Cape Peninsula University of Technology

MEASUREMENT AND MODELLING OF GEOMAGNETICALLY INDUCED CURRENTS (GIC) IN POWER LINES.

by

ELECTDOM MATANDIROTYA

Thesis submitted in fulfillment of the requirements for the degree

Doctor of Engineering: ELECTRICAL ENGINEERING

in the Faculty of: Engineering

at the Cape Peninsula University of Technology

Supervisor: Prof. P. J. Cilliers
Co-Supervisor: Prof. R. R. Van Zyl

Bellville

July 2016

DECLARATION

I, Electdom Matandirotya, declare that the contents of this thesis represent my own unaided work, and that the thesis has not previously been submitted for academic examination towards any qualification. Furthermore, it represents my own opinions and not necessarily those of the Cape Peninsula University of Technology.

Electdom Matandirotya
signed

25 February 2017
date

ABSTRACT

Geomagnetically induced currents (GIC) are currents induced in ground-based conductor networks in the Earth's surface. The GIC are driven by an electric field induced by geomagnetic variations which are a result of time-varying magnetospheric-ionospheric currents during adverse space weather events. Several studies have shown that there is a likelihood of technological damage (the power grid) in the mid- and low-latitude regions that could be linked to GIC during some geomagnetic storms over the past solar cycles. The effects of GIC in the power system can range from temporary damage (e.g. protective relay tripping) to permanent damage (thermal transformer damage). Measurements of GIC in most substations are done on the neutral-to-ground connections of transformers using Hall-effect transducers. However, there is a need to understand the characteristics of GIC in the power lines connected to these transformers. Direct measurements of GIC in the power lines are not feasible due to the low frequencies of these currents which make current measurements using current transformers (CT) impractical.

This thesis discusses two techniques that can be employed to enhance understanding GIC characteristics in mid-latitude regions. The techniques involve the measurement of GIC in a power line using differential magnetometer measurements and modelling GIC using the finite element method. Low frequency magnetometers are used to measure magnetic fields in the vicinity of the power lines and the GIC is inferred using the Biot-Savart law. A finite element model, using COMSOL-Multiphysics, is used to calculate GIC with the measured magnetic field and a realistic Earth conductivity profile as inputs. The finite element model is used for the computation of electric field associated with GIC modelling.

The two techniques explored have proved to be useful tools that can be used in GIC measurements and modelling. The differential magnetometer measurement results indicate that the characteristics of GIC in the power line are similar to those of the GIC measured at the neutral-to-ground connection of the power transformers. On the other hand, the finite element modelled GIC also reveal that the characteristics of the GIC in the power network can be estimated with high confidence by calculating the surface electric field and using network coefficients derived using other methods. Thus, there is no need to add the system circuitry to the layered Earth model to optimise the model. These techniques can be used to complement each other when it comes to GIC measurements and model validation. The differential magnetometer method (DMM) observations could provide the much needed data to improve GIC model validation in the Southern African region. The finite element method (FEM) model also expands the study by providing a means of investigating current distribution in the Earth's different geological environments.

LIST OF PUBLICATIONS

Some of the work done in this thesis is published in international journals as well conference proceedings. The published articles are listed below:

1. Matandirotya, E., Cilliers, P. J. and Van Zyl, R. R. Methods of measuring and modelling geomagnetically induced currents (GICs) in a power line, *in Proceedings of SAIP 2013, the 58th Annual Conference of the South African Institute of Physics*, edited by Roelf Botha and Thulani Jili (SAIP and University of Zululand, 2014), pp.410 - 415. ISBN: 978- 0-620-62819-8

2. Matandirotya, E., Cilliers, P. J. and Van Zyl, R. R. 2015. Modelling geomagnetically induced currents in the South African power transmission network using the finite element method. *Space Weather*, 13, 185-195. doi: 10.1002/2014SW001135

3. Matandirotya, E., Cilliers, P. J. and Van Zyl, R. R. 2015. Differential magnetometer method (DMM) for the measurement of geomagnetically induced currents (GIC) in a power line: Technical aspects, *Journal of ELECTRICAL ENGINEERING, 66, 7/s, 50-53.*

4. Matandirotya, E., Cilliers, P. J. and Van Zyl, R. R, Oyedokun, D. T., de Villiers, J. 2016. Differential magnetometer method applied to measurement of geomagnetically induced currents in Southern African power networks, *Space Weather* 14, 221-232. doi: 10.1002/2015SW001289

5. Matandirotya, E., Cilliers, P. J. and Van Zyl, R. R. 2016. Modelling ground conductivity for computing the electric field associated with geomagnetically induced currents (A mid-latitude case study), *in Proceedings of SAIP 2015*

ACKNOWLEDGEMENT

The success of this DTech journey was made possible by a number of people. I may not mention you all but I am grateful for all the contributions. First and foremost, I thank my Heavenly Father for His grace to see me through.

I am indebted to my supervisors, Prof. P. J. Cilliers and Prof. R. R. Van Zyl for their guidance, advice, encouragement, patience and support throughout the whole study. Thank you for helping me realise this dream. I wish to also convey my many thanks to the SANSA Space Science management team for awarding me the bursary and all the "behind the scenes" support to make sure that my stay in South Africa during my studies is enjoyable and worth it.

I would like to thank the SANSA Space Science Technology team (Danie Gouws and Elda Saunderson), the GIC research group (Stefan Lotz, Jean de Villiers and David Oyodekun) and the Engineering and Data Acquisition team (Errol Julies, Ziyaad Isaacs and Jimmy Makoloane) for all the technical support. Thank you all for creating a conducive working environment, the productive discussions, and your willingness to help me sort out all the instruments whenever it was necessary. I couldn't have met the deadlines without your expertise and assistance.

Newton Runyararo Matandirotya, my husband, you deserve a special mention for being patient, encouraging and above all the most supportive throughout my studies. You never stopped believing in me till the end. Mazviita and Makaita (my children), your smiles and tears kept me going. You always reminded me why I should finish in time so that I can give you the deserved attention.

Many thanks to my family (both the Matandirotya and Siziba) for the moral support, the fatherly, motherly, brotherly and sisterly love you directed towards me through this journey and the unconditional support was amazing. Though I was miles away from home, some people dedicated their time whenever necessary. This actually contributed significantly to the success of my studies. Thanks to Mrs Tshimangadzo Matamba who knew when to switch between roles of being a friend, a sister and a colleague when it mattered most. To Elda Saunderson, Jeanne Cilliers, Anita Engelbrecht, Mpho Tshisaphungo, Mr and Mrs Nyandwi, John Bosco Habarulema and Adrian Chimphalika, you were an awesome "family". I wouldn't have reached this far without most of your sacrifices. May the Almighty keep blessing you for all your efforts.

To all the SANSA Space Science based students from 2011-2015 (including those who left to join other institutions), thank you guys for the academic discussions, the soccer games, the hiking and all the support you gave me. Ifriky Tadadjeu and Morne Roman, thanks for being part of this journey.

DEDICATION

To my lovely family

My awesome fathers
Rev Debson Siziba and Agripa Matandirotya

My amazing mothers
Mrs Josephine Siziba and the late Ms. Magret Makamure

My marvellous husband
Runyararo Newton Matandirotya

My blessed kids
Mazviita Kgotso and Makaita Ndivhuwo

GLOSSARY

Terms/Acronyms/Abbreviations	Definition/Explanation
AC	Alternating Current
CPUT	Cape Peninsula University of Technology
CIM	Complex Image Method
CME	Coronal Mass Ejection
CT	Current Transformer
DC	Direct Current
DMM	Differential Magnetometer Method
DOFs	Degrees of Freedom
EM	Electro-Magnetic
Eskom	The South African power utility
EPRI	Electrical Power Research Institute
FEM	Finite Element Method
GIC	Geomagnetically Induced Currents
HBK	Hartebeesthoek INTERMAGNET station
HER	Hermanus INTERMAGNET station
INTERMAGNET	International Real-time Magnetic Observatory Network
KMH	Keetmanshoop INTERMAGNET station
NASA	National Aeronautics and Space Administration
NamPower	The Namibian power utility
NUST	Namibian University of Science and Technology
nT	nanoTesla
MAS	Method of Auxiliary Sources
SANSA	South African National Space Agency
SECS	Spherical Elementary Current System
SSC	Sudden Storm Commencement
TSU	Tsumeb INTERMAGNET station
UCT	University of Cape Town

LIST OF SYMBOLS

List of symbols used in the work. Vector quantities are denoted by bold letters. SI units are adopted and used throughout the document.

A magnetic vector potential
H magnetic field intensity in spatial domain
E electric field in spatial domain
B magnetic flux in spatial domain
J current density
I line current
t time
σ electrical conductivity
μ_0 permeability of free space
ϵ_0 permittivity of free space
ω angular frequency
p complex skin depth
R reflection coefficient of the Earth

CONTENTS

LIST OF FIGURES

LIST OF TABLES

CHAPTER 1: INTRODUCTION

1.1 Research background

The objective of the study reported here is the measurement and modelling of geomagnetically induced currents (GIC) in the Southern African power system using the differential magnetometer method (DMM) and finite element method (FEM).

The currents induced on the Earth's technological systems due to geomagnetic perturbations are referred to as GIC. The GIC are quasi-DC currents of which the maximum frequency in their spectrum are a few mHz. GIC are intensively studied within the physics and engineering communities in academic and non-academic environments. Scientists and engineers are making efforts to predict and adequately model GIC occurrences so as to build up an alert system that can be implemented in the mitigation and management of impacts of space weather on ground based conductor networks. Industries that are challenged by the existence of GIC in their systems collaborate with academic institutions so as to understand the characteristics, dynamics and associated mechanisms of GIC. The studies address the need to understand, model and predict GIC in any technological system. Research on estimating the drivers of GIC and relevant measurements for estimating GIC is on-going at various institutions. Furthermore, measurements of GIC in specific technological systems, such as power lines, are also done in order to complement the studies.

The United Kingdom (UK) (Hapgood and Rees, 2014) and the United States of America (USA) (`http://www.nerc.com/Pages/default.aspx`) have formulated strategies that enhance the understanding of space weather dynamics and the potential threats to power systems on the Earth. These strategies create awareness and also encourage effective modelling, prediction and mitigation of GIC on grounded technologies. GIC research in Southern Africa started at the University of Cape Town (UCT) in collaboration with the South African power utility (Eskom) and the Electrical Power Research Institute (EPRI) in 1999 (Koen, 2002).

1.2 Research statement

Measurement of GIC in the power lines using transducers at transformers neutrals to monitor GIC is expensive as the grid network is usually extensive and complex. An alternative way is to assess GIC is to model GIC so that one can predict what values of GIC to expect during geomagnetic storms. Modelling would enable continuous now casting so that alerts to power companies may be issued in a timely manner. In this research we modelled GIC using the finite element method (FEM) and validated the results using both the differential magnetometer method (DMM) and direct GIC measurement.

1.2.1 Research objectives

The primary objectives of the research are to:

- Identify suitable magnetic sensors that can be used for measuring GIC in the power lines and develop a low cost magnetic field measurement system for measuring GIC via the magnetic field under a power line;
- Formulate and evaluate an algorithm for inferring GIC in the power line from differential magnetometer measurements;
- Develop a 2D finite element methods (FEM) model and evaluate the application of 2D FEM in the modelling of GIC using measured magnetic field data as input.

1.2.2 Research questions

The research addresses the following questions:

1. What is the best configuration of instruments for estimating the GIC via magnetic field measurements under the power line?
2. What is the best algorithm for estimating the GIC in a power line from magnetic measurements on the ground under the power line?
3. What is a suitable representation of the Earth for the estimation of GIC using FEM?
4. What are the best conductivity profiles to use for efficient modelling of GIC using the FEM?
5. What are the characteristics of the induced current distribution in the Earth?
6. How does the GIC estimated by means of the FEM compare with GIC derived from other models and GIC measurements in the power line?

1.3 Research motivation

Geomagnetic storms may occur any time, however the probability is higher several years after the solar cycle peak. Since GIC effects on power grid lead to losses in terms of power blackouts and transformer replacements, continuous and reliable and cost effective measurements or modelling and now casting is needed. This will ensure that during geomagnetic storms, GIC alerts may be provided as part of space weather alerts to improve monitoring power disruptions. This will in turn help power companies cut down on overheads related to GIC and improve on their revenue.

The research presented here is conducted using the data collected during the years 2013-2015 near the peak of solar cycle 24; hence, geomagnetic disturbances resulting from geomagnetic storms are likely. Measuring GIC in a power line using the DMM is more sensible during geomagnetic storms, since these storms are more likely to have events where the response of the magnetometers to GIC in the network is above the noise level. The research contributes to the understanding of the extent to which GIC occur in mid-latitude power networks.

1.4 Research significance

The research findings reported may be a tool in the field of space weather hazard monitoring and modelling. The study and understanding of GIC aim at efficiently modelling the characteristics of GIC to an extent where the power utilities are able to manage the effects and challenges posed by GIC on the power grids. Using the techniques developed in this research, the power utilities will be able to estimate the expected magnitude and dynamics of the GIC in the power transformers more efficiently.

1.5 Delineation

- The project does not include the development of the Southern African ground conductivity profile. Realistic conductivity values from the literature are used for various Earth layers and these layers are limited to homogeneous planar layers with 1D conductivity variations with depth.

- The effects of GIC in the transformers are not investigated in the current work. Models developed by others are used for calculating GIC in transformers when comparisons are made with GIC estimated from measurements under power lines. Only GIC in the power lines were be calculated.

- FEM simulation are limited to a 2D (lateral distance, depth) representation of the relevant Earth geometry due to high computational memory demand and long simulation times required for 3D modelling and the lack of 3D conductivity data for the region of interest.

1.6 Research methodology

1.6.1 Differential magnetometer method (DMM)

The differential magnetometer method implements an indirect, practical way of obtaining the GIC in power lines during geomagnetic disturbances. The method was originally developed in 1970 by (Campbell, 1978, 1980) for the measurement of GIC in the oil pipe lines in Alaska. In the 1990s, it was modified to measure GIC in the power network in Finland (Mäkinen, 1993; Viljanen and Pirjola, 1994) and has also been applied in Brazil (Trivedi *et al.*, 2007).

It is a dangerous practice to measure the GIC in a power line directly due to high voltages involved in the transmission of electricity. The Biot-Savart law is implemented in the calculation of the GIC from the difference between the measured geomagnetic field at two locations near the power line. A pair of fluxgate magnetometers is used to measure magnetic field due to the GIC in a power line at a selected site. It is a requirement that the location of the pair of magnetometers will be chosen such that there is negligible spatial variation of the background geomagnetic field at the magnetometer locations.

It is known that, in the absence of GIC on the power line, the only current expected is 50 Hz current and some harmonics of 50 Hz. Magnetometers with a low cut-off frequency (below 0.1 Hz) are used

to measure the magnetic field under the power line. This allows the estimation of the GIC in the power line from the measured magnetic field.

1.6.2 Finite element modelling

One challenge that has been posed in the GIC research field is the difficulty of separating the magnetic effects of the GIC in the power line from the geomagnetic field that would have existed in the absence of the power line. Finite element modelling would help in the understanding of the nature of the currents flowing in the power lines and beneath the Earth's surface during a geomagnetic storm. To address these complications and the complexity of the geometry, FEM modelling is implemented. A study by Dong *et al.* (2013) using simulated currents in the ionosphere has demonstrated that FEM can be applied in the computation of the magnetic field and electric field associated with GIC.

FEM modelling aims at obtaining an approximate solution of a complex problem, using an idealised model which is a closer representative of the real problem than is feasible with an analytic model. The solution obtained from a FEM may not be "exact" but is accurate enough to improve the understanding of the problem at hand, in cases where analytical techniques are difficult or impossible to implement (Humphries, 2010). The FEM divides the complex geometry into non-overlapping but joined finite subdivisions (elements). The subdivisions simplify the elemental solutions and allow the integration of the solution of each element to give an overall solution of the whole system. It is possible to solve Maxwell's equations and boundary conditions for the magnetic and electric field using integral equation methods to address the geophysical step of GIC calculation (Boteler and Pirjola, 1998*a*). However, the principles are hard to implement practically, due to extensive computation of the required integral over space and time.

1.7 Thesis layout

The thesis consists of 7 chapters. Chapter 1 gives an overview of the research project, describing the problem and the objectives of the research. Chapter 2 deals with relevant literature that defines the research context. The topics discussed in Chapter 2 aim at giving an insight into space weather, the processes that lead to the establishment of GIC and their effects on the electrical power grid. Chapter 3 discusses the technical aspect of the differential magnetometer method. Chapter 4 presents results of the application of the differential magnetometer method in Southern Africa. Chapter 5 discusses the basics of the FEM and its application in the current research, including the application of COMSOL Multiphysics as the FEM software chosen for this particular research. Chapter 6 presents the results from the FEM model. Chapter 7 evaluates the outcomes against the research goals and expected outcomes, and makes recommendations for future research.

CHAPTER 2: LITERATURE REVIEW

2.1 Introduction

This chapter explores the literature associated with geomagnetically induced currents (GIC), the differential magnetometer method (DMM) and the finite element method (FEM). The literature reviewed includes papers on the solar events that produce GIC on the Earth's surface. GIC related studies that have been carried out in the Southern African region and their findings are briefly discussed. Emphasis is put on the computation of the geoelectric field from the geomagnetic field, which can be either modelled or measured. The chapter is concluded by pointing out some methods that are adopted in the mitigation of GIC in power networks.

2.2 Background

The effects of GIC were first noted in the 1840s in telegraph lines. The telegraphic systems of that era experienced high abnormal currents, which were later deduced to be associated with space weather events such as solar storms (Boteler *et al.*, 1998; Béland and Small, 2005; Gummow and Eng, 2002).Calculating the electric field that drives the GIC has been a scientific challenge. The electric field is affected by, amongst others, the ground conductivity, which is inhomogeneous and anisotropic. A study carried out in the United Kingdom (Beamish *et al.*, 2002) indicated that the appropriate modelling of the surface resistivity is crucial for the accurate calculation of the magnitude of GIC.

2.2.1 GIC in mid-latitudes

The GIC research in other mid-latitude countries such as Brazil (Trivedi *et al.*, 2007), Spain (Torta *et al.*, 2012), China (Liu *et al.*, 2009) and Australia (Marshall *et al.*, 2011) have confirmed the presence of GIC in mid-latitude power grids during geomagnetic storms.

2.2.2 Previous studies of GIC in the Southern Africa

The modelling of GIC in Southern African power networks make use of the magnetic field measured at four INTERMAGNET (`http://www.intermagnet.org/`) Magnetic Observatories which are Tsumeb (TSU), Keetmanshoop (KMH), Hermanus (HER) and Hartebeesthoek (HBK). GIC measurements are available for selected periods for some, but not all, substations in the region. Figure 2.1 shows the location of the INTERMAGNET observatories and some GIC measurement sites in Southern Africa.

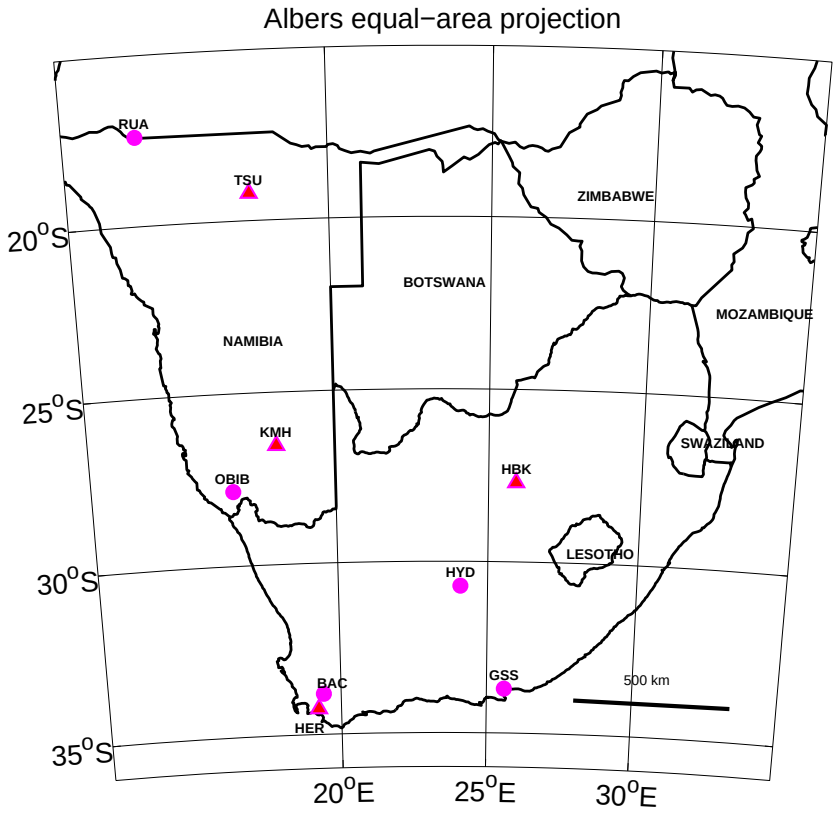

Figure 2.1: Map showing the location of the INTERMAGNET Observatories in Southern Africa (TSU, KMH, HER, HBK) and the GIC measurement sites in Southern Africa (GSS, HYD, BAC, RUA and OBIB) which are addressed in this work. The names and coordinates of these sites are given in Table 2.1.

Table 2.1: Names and geographical coordinates of the INTERMAGNET observatories and GIC measurement sites discussed in this thesis.

INTERMAGNET OBSERVATORIES			
Code	**Name**	**Latitude[deg]**	**Longitude[deg]**
TSU	Tsumeb	-19.20	17.58
KMH	Keethmanshoop	-26.54	18.11
HBK	Hartebeesthoek	-27.7	25.9
HER	Hermanus	-34.4	19.2
GIC MEASUREMENTS SITES			
RUA	Ruacana	-17.40	14.22
OBIB	Obib	-27.84	16.64
HYD	Hydra	-30.71	24.09
BAC	Bacchus	-33.81	19.40
GSS	Grassridge	-33.72	25.63

During the period 1999-2002 the existence of GIC over the Southern African region was established through the research done by Koen (2000), (Gaunt and Coetzee, 2007). Among other significant findings of that research, was the validation of models for GIC in Southern Africa. The theoretical GIC values were obtained through the use of a plane wave model and a homogeneous, half-space Earth model with a conductivity value of 0.001 S/m. Two South African substations were investigated, i.e. Grassridge (GSS) and Hydra (HYD) (shown in Figure 2.1). The results of the modelled and measured GIC are illustrated in Figure 2.2 for GSS and Figure 2.3 for HYD. Furthermore, it was concluded that the vulnerability of the network to GIC depends on the network configuration. The work by Koen initiated the research on the characterisation and modelling of GIC in the electricity power system of the Southern African region.

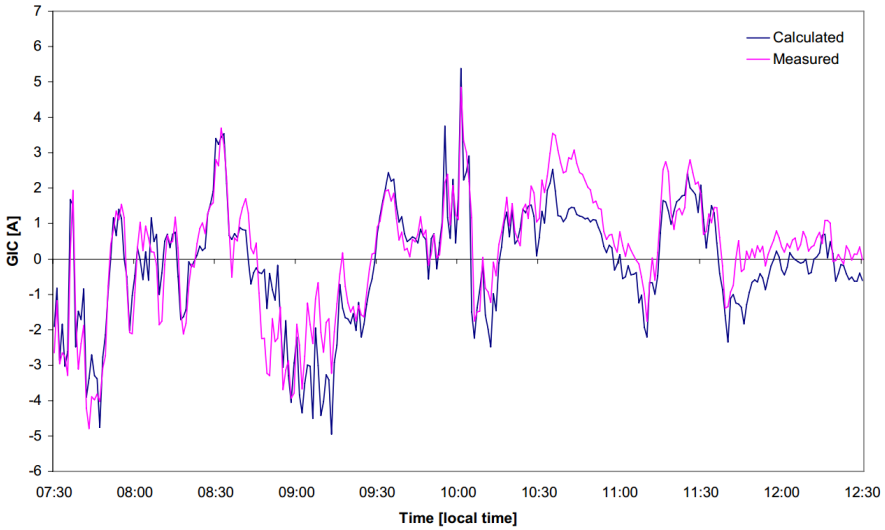

Figure 2.2: The measured and calculated GIC at GSS substation during the 31 March 2001 geomagnetic storm. Adopted from (Koen, 2002).

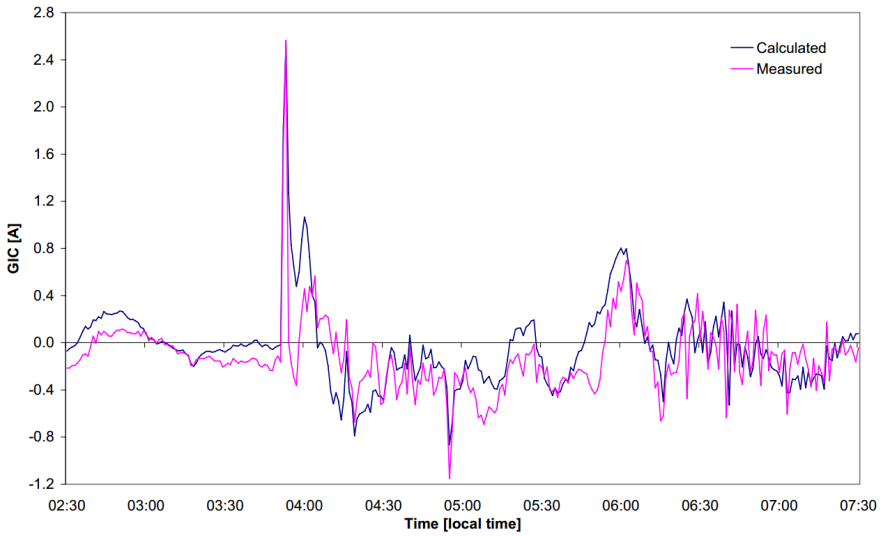

Figure 2.3: The measured and computed GIC at HYD substation during the 31 March 2001 geomagnetic storm. Adopted from (Koen, 2002).

In a subsequent GIC modelling study, the methods that were applied by Koen (2002) were implemented by Zatjirua (2005) over the Namibian transmission network. Despite the fact that there were no GIC monitoring stations in Namibia at that time, the applied model indicated that GIC were likely to occur in the Namibian transmission network. High currents above 10 A were estimated for some of the Namibian substations for the Halloween storm of 2003, as illustrated in Figure 2.4 (Zatjirua, 2005).

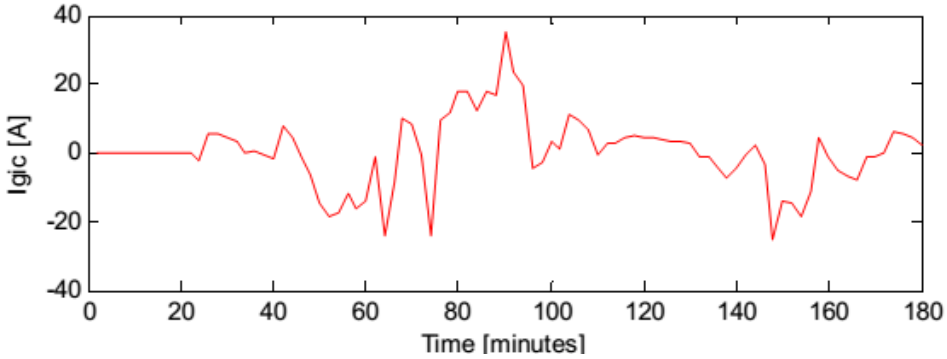

Figure 2.4: Calculated GIC at the Ruacana substation in Namibia for the October 2003 geomagnetic storm. Adopted from (Zatjirua, 2005).

Bernhardi (2006) contributed significantly with the improvement on calculation and modelling of GIC in the South African and Namibian power networks through the use of the Spherical Elementary Current System (SECS) method. His work indicated that there is a spatial non-uniformity of the geoelectric field over large areas during a geomagnetic event as illustrated in Figure 2.5. It was further illustrated that using the SECS method and the available magnetic field measured at different stations in the region, GIC can be better estimated by interpolating the magnetic field data to the measurement station (Bernhardi *et al.*, 2008). A conclusion was reached that if geomagnetic data from a single station is considered for GIC computation, the station must be close to the GIC measurement point (within 300 km).

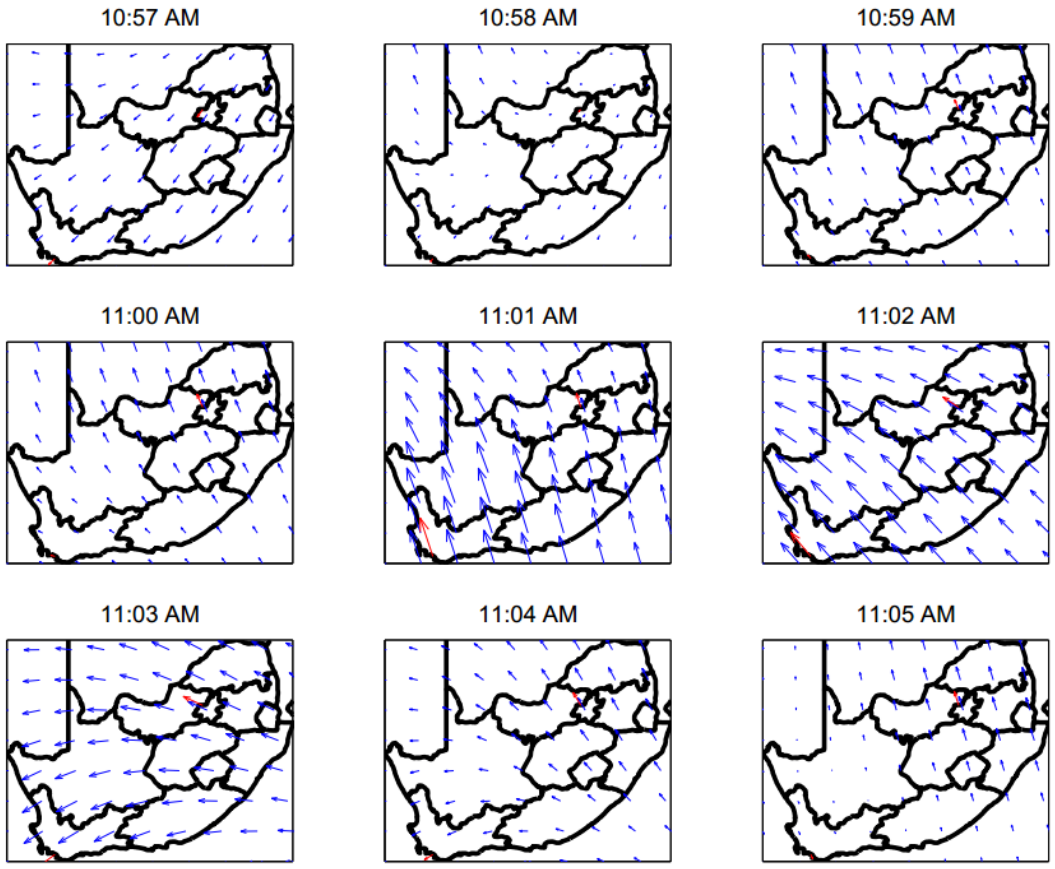

Figure 2.5: Typical variations of the electric field over South Africa during a geomagnetic storm at 1 minute intervals on 29 October 2003. Adopted from (Bernhardi, 2006).

Ngwira *et al.* (2008) contributed to the progress in the GIC modelling through the establishment of a surface impedance profile for Grassridge using geomagnetic field data and GIC data measured at the GSS substation in South Africa (Port Elizabeth). A 1D resistivity profile for GSS, shown in Figure 2.6, was developed and used for improving the GIC model.

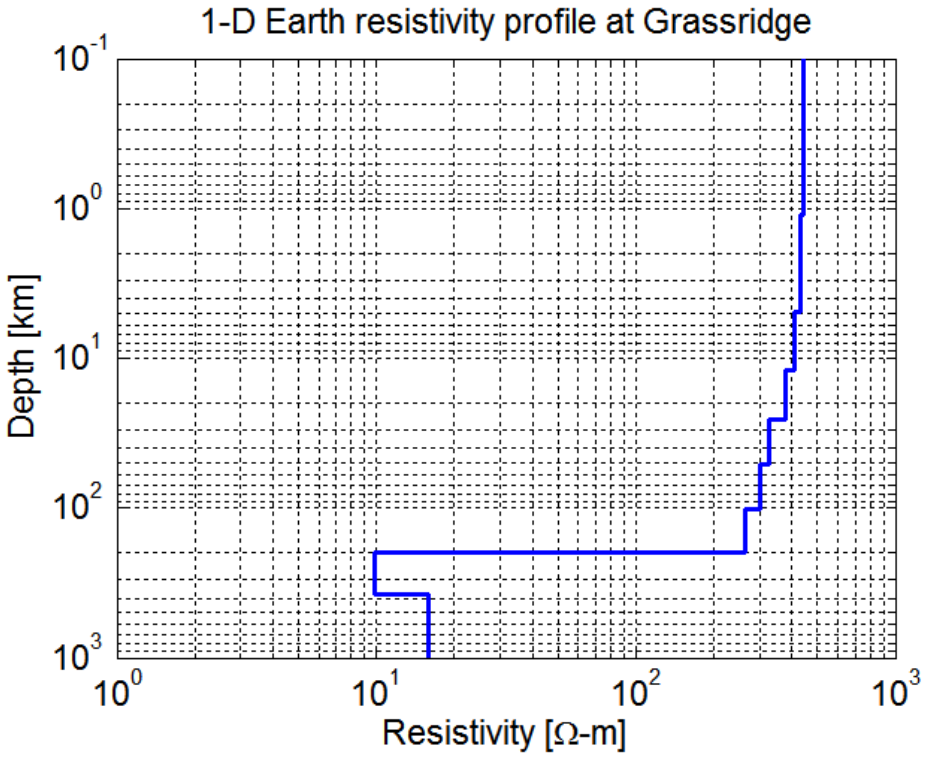

Figure 2.6: Resistivity for various Earth layers at the Grassridge substation. Adopted from (Ngwira *et al.*, 2008).

The challenge faced in all the modelling to date is a lack of measured GIC data that could be used for comparison with modelled GIC to improve the existing models (Ngwira *et al.*, 2009). Not much has been documented on GIC in other Southern African countries. This does not rule out the existence of GIC in their power networks, as most of the networks are interlinked. Namibia and South Africa have invested in the GIC research through collaborations between the national power utilities (Eskom and NamPower), the South African National Space Agency (SANSA), University of Cape Town (UCT), Namibian University of Science and Technology (NUST) and Cape Peninsula University of Technology (CPUT).

2.3 Space weather events

The Sun is the driver of space weather events. A significant fraction of the energy of the Sun propagates through the space environment in the form of electromagnetic radiation (Priest, 1995). A number of events influenced by the conditions of the Sun occur in the regions of space between the Sun and the Earth. The rest of this section describes the stages illustrated in Figure 2.7 (Lang, 2009).

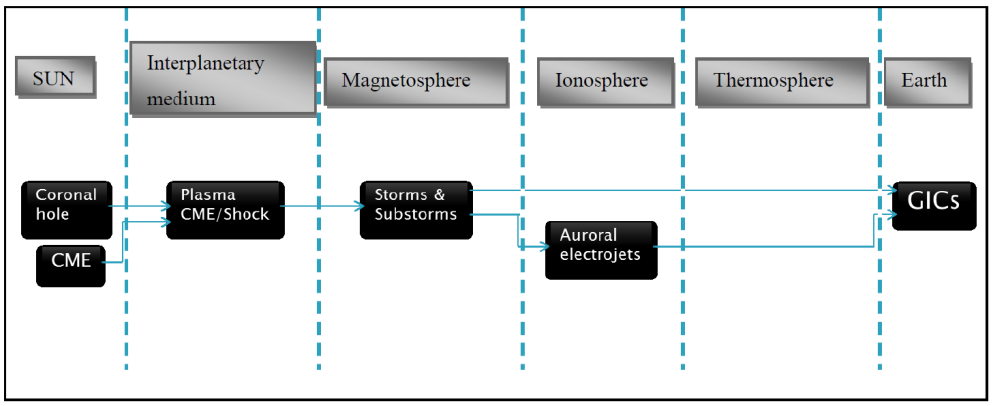

Figure 2.7: An illustration of several space weather related events that occur between the Sun and the Earth in the process of causing GIC.

Stage 1: The Sun's plasma processes initiate the emission of electromagnetic (EM) radiation, corpuscular radiation, charged atoms, and sub-atomic particles such as protons and electrons. These emissions are achieved through what is known as coronal mass ejections (CME), as illustrated in Figure 2.8, which are characterised by an explosive release of plasma and magnetic flux from the Sun's upper atmosphere into space (Priest, 1995; Moldwin, 2008).

Figure 2.8: Coronal mass ejection. Adopted from (NASA/MSFC, 2010).

Stage 2: Particles such as electrons and protons constantly released from the Sun, propagate though the interplanetary medium as magnetised plasma in what is known as the "solar wind". The solar wind has a speed of up to $\approx$ 2000 km/s during a major storm, and hence, can reach the

Earth within one day. The red arrows in Figure 2.9 illustrate the flow of the solar wind as it interacts with the magnetosphere.

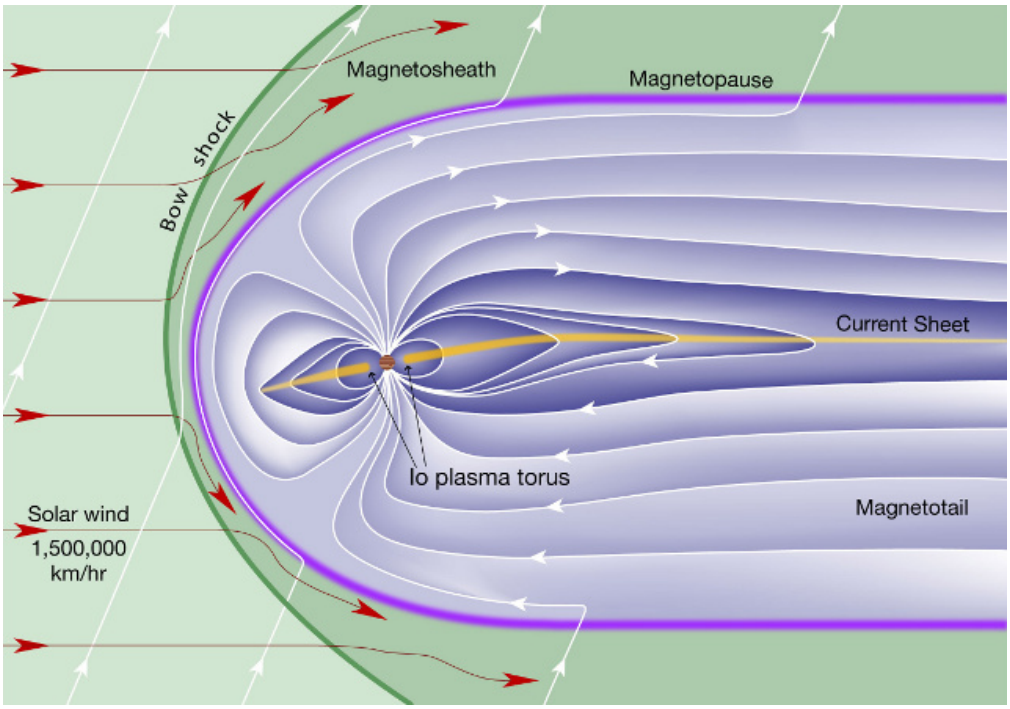

Figure 2.9: Artist's impression of the flow and interaction of the solar wind with the interplanetary medium for a quiet-time solar wind speed of 1 500 000 km/hr. Adopted from (MrReid.Org., 2011).

Stage 3: The propagated solar wind interacts with the geomagnetic field. The magnetosphere is the region where the magnetic field of an astronomical object controls the behaviour of the particles in its vicinity (Ratcliffe, 1972). At this stage, the orientation of the solar wind magnetic field determines the intensity of the energy transferred during the reconnection of the solar wind and the magnetosphere. High energy releases result in changes in the magnetospheric electric currents. These interactions enhance the onset of the so-called geomagnetic storms and sub-storms (Pulkkinen, 2003). The southward directed interplanetary magnetic fields result in intense geomagnetic storms during the reconnection with the magnetosphere magnetic field (Tsurutani, 2001).

Stage 4: The perturbations in the magnetosphere have an impact on the stability of the ionosphere. The dynamic changes in the magnetosphere link with the ionosphere through the ionospheric polar regions. During the magnetosphere-ionosphere interactions, the magnetospheric current system transfers energy to the ionospheric particles. These variations and couplings result in auroral and other electrojets in the ionosphere, which are horizontal electric currents flowing in the D and E layers of the ionosphere (Kamide, 2001; Pulkkinen, 2003). These time-varying currents in the ionosphere induce a time- and spatially-varying magnetic field, which in turn induces an electric field.

Stage 5: A geomagnetic field variation is induced due to the rapid changes in the magnetosphere-ionosphere electric currents. The geomagnetic field induces a geoelectric field on and beneath the Earth's surface. The conductivity profile of the Earth's surface determines the surface impedance, which in turn determines the characteristics of the resultant geoelectric field. The geoelectric field creates a voltage gradient over any long conductor aligned with it. The induced currents do not have a well-defined pattern that could resemble that of the ionospheric source (Campbell and Zimmerman, 1980), due to in-homogeneity of the Earth's conductivity.

Stage 6: Grounded technological systems such as power lines, are the transmission paths of the induced voltages resulting in a current flow within the systems. The characteristics and electrical properties of the conductors in the power network determine the distribution of the induced currents within the particular network (Pirjola, 2000).

2.3.1 Geomagnetic storms

At the onset of a geomagnetic storm, the Earth's magnetic field undergoes a very short and small increase called the sudden storm commencement (SSC). The subsequent phase is a large decrease in the magnetic field, which is called the main phase of the the storm. The extent at which the magnetic field of the Earth is disturbed can be indicated by a localised magnetic index called the K-index, which has a scale of 0-9, where 0-4 does not produce significant GIC while 5-9 indicates larger disturbances, which are more likely to produce significant GIC disturbance. The Kp-index is a planetary average of the K-indices of a number of observatories, which can also be used as an alternative to a local K-index where there is no local data available. The disturbance storm time (Dst) index is another index that is used to measure the severity of a geomagnetic storm. The unit of measurement of the Dst-index is nanoTesla (nT) and it is averaged hourly from four geomagnetic observatories. Figure 2.10 illustrates a typical variation of the total magnetic field, the Dst and Kp indices during the October 2003 Halloween storm. Another index used is called the Ap-index, which is a daily index rather than a 3-hour index, such as the Kp-index.

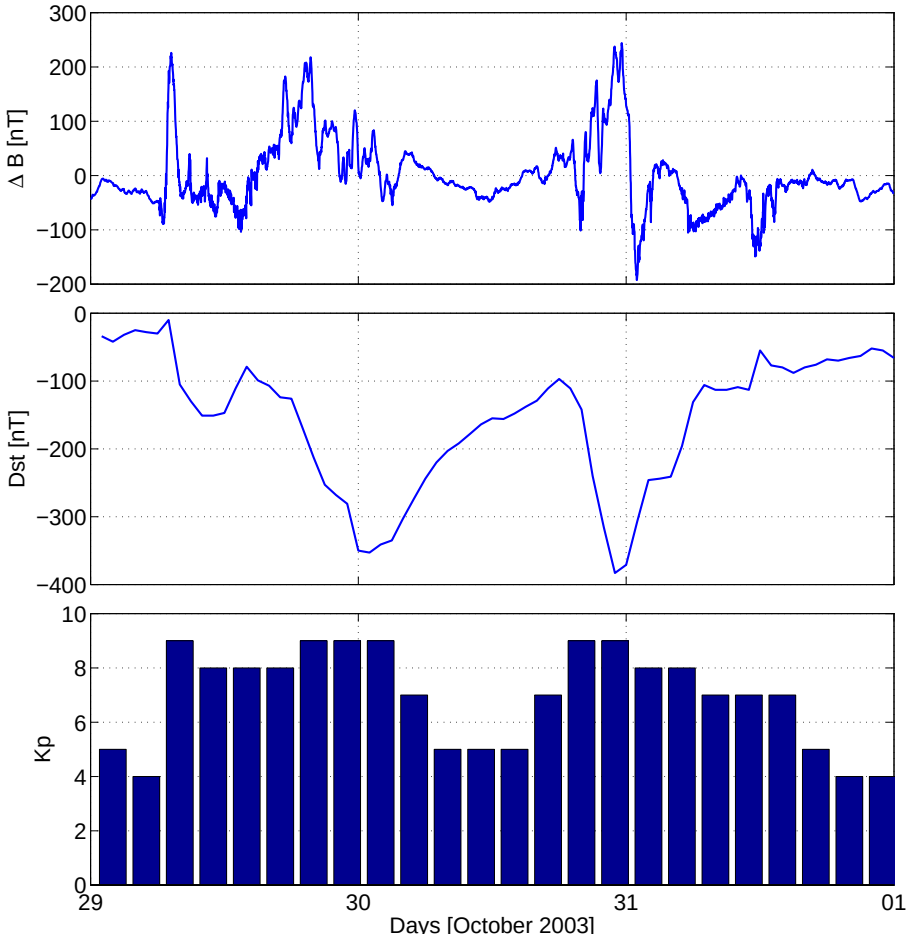

Figure 2.10: A typical variation total magnetic field, Dst and Kp indices during a geomagnetic storm. The main phase of the geomagnetic storm is associated with higher Kp index values. (Top) The total magnetic field variations measured in Hermanus during a geomagnetic storm of 29 to 31 October 2003. (Middle) The Dst index during the storm period. (Bottom) The corresponding Kp-index.

2.4 Geomagnetically induced currents in power systems

Grounded systems such as power grids, telecommunication cables, railway lines and oil and gas pipelines are affected by the ground currents that are enhanced during adverse space weather. The effects come as a result of currents induced in the Earth during geomagnetic storms. The GIC in a particular grounded system is determined by the conductivity profile of the Earth and to a certain extent, the length of the conductor (Pirjola and Boteler, 2002; Boteler *et al.*, 1998). Coastal boundaries and high resistivity regions tend to have high geoelectric fields induced during geomagnetic storms (Koskinen *et al.*, 2001). The effects of the GIC will differ from one technological network to the other depending on the transformer types, network configuration and the load (Pirjola, 2000; Molinski, 2002).

GIC are introduced into the power system through the grounded neutral nodes of Y-connected transformers. Figure 2.11 illustrates the possible path followed by the GIC within the transmission

network. The GIC splits equally among the three phases of the transformer.

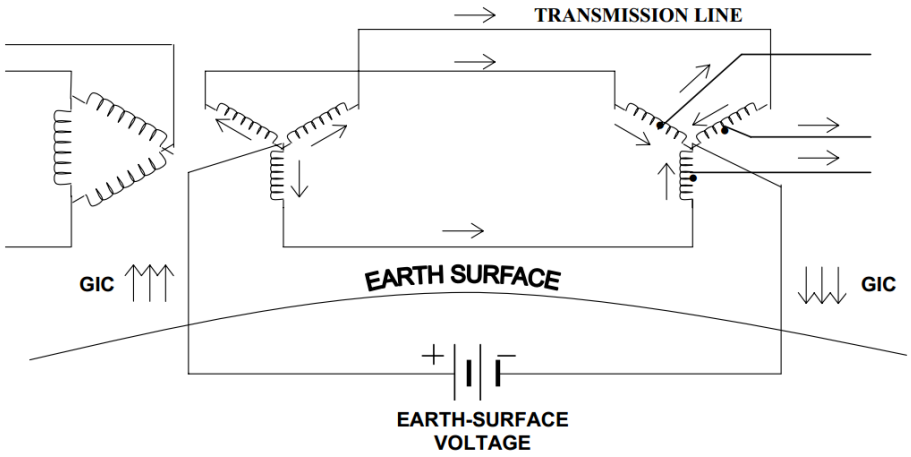

Figure 2.11: GIC introduced into the power system via grounded transformers. Adopted from (Koen, 2002).

2.4.1 Transformer saturation

The GIC are low frequency currents, in the range of 0.1-10 mHz. Power systems normally operate at 50 Hz or 60 Hz. The GIC in the power system are, therefore, seen as quasi-DC currents due to their low frequencies compared to the power distribution current. Due to the biasing of the core magnetisation, as illustrated in Figure 2.12 (Price, 2002; Girgis *et al.*, 2012), half-cycle transformer saturation occurs. Once the transformer core is saturated, it operates on the non-linear side of the steel magnetisation curve. The core is then forced to transfer the excess flux through other routes, such as the tank wall. The transformer, thus, draws high currents that are unsymmetrical (Koen, 2002). The transformer saturation manifests as harmonic distortion, reactive power demand, increase in noise level and transformer heating 2.13.

Furthermore, the saturation of the transformers distorts the AC transmission in the transformer and lowers the voltage. In cases of a heavily loaded network, the voltage drops may result in blackouts, e.g. in Quebec in 1989 (Bolduc, 2002).

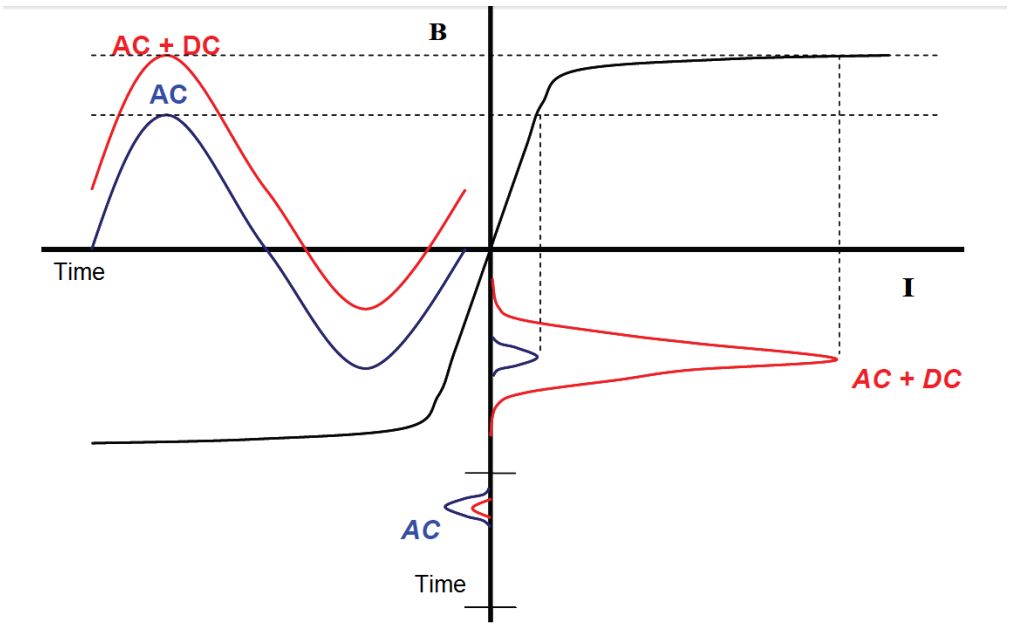

Figure 2.12: Representation of the excitation current before and after coupling with GIC. B is the magnetic flux density and I is the current. Adopted from (Girgis *et al.*, 2012).

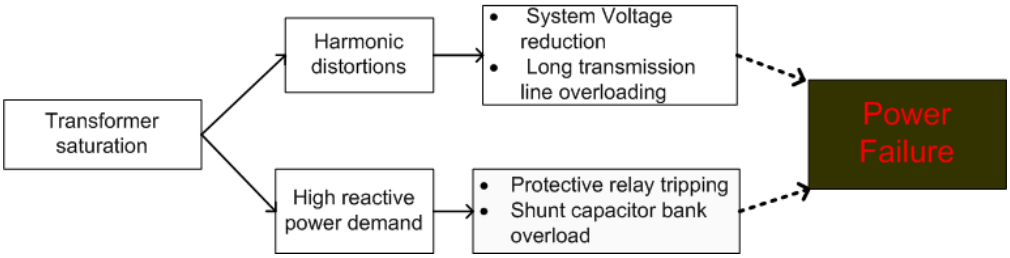

Figure 2.13: Summarised effects of GIC on the power systems that could lead to power failures due to a saturated transformer.

2.4.2 Transformer heating

When there is excessive flux in the transformer, the flux finds alternative paths, such as through clips or via the tank wall. Eddy currents are enhanced within some parts of the transformer during saturation. These eddy currents initiate localised heating, resulting in hot spots. Figure 2.14 shows damage caused by GIC in transformers due to a localised hot spot. In cases of overheating, the magnetic circuit is highly affected and may lead to melting of the windings. Factors such as the type of material exposed to the excess flux and the size of the transformer affect the extent to which the transformer is damaged.

Figure 2.14: Effects of transformer heating associated with GIC. Adopted from http://www.spaceweather.gc.ca/tech/se-pow-eng.php.

2.4.3 Power system susceptibility to GIC

The interlinking of power networks could be a preventative measure for localised power disruption causes, such as lightning strikes, but the whole GIC phenomenon poses a threat to the configuration. GIC effects tend to spread throughout the grid and, therefore, the damage may occur at several locations in the grid. The high electricity demand by heavy industries also increases the vulnerability of the grid to GIC. Heavily loaded grids are more susceptible to GIC.

2.5 Computation of geomagnetically induced currents

An adequate analysis of the GIC takes into account two significant steps:

1. **The geophysical step:** The computation of the horizontal components of the surface geoelectric field on the surface of the Earth. This stage requires a knowledge of the surface impedance, which can be derived from the conductivity profile of the Earth.

2. **The engineering step:** The calculation of GIC from the configuration and electrical parameters of the grounded system together with the knowledge of the geoelectric field.

Due to the fact that the frequencies dealt with in GIC calculation are less than 10 mHz, the quasi-static approximation is applied. This approximation neglects the inductive and capacitive effects in the system under investigation. Another significant assumption usually made, justified by the "locality" of the computations, is that of the flat-Earth. These assumptions reduce the complexities of the mathematics (Pulkkinen, 2003).

2.5.1 The geophysical step

The computation of the geoelectric field can be achieved from the knowledge of either the measured geomagnetic field or the ionospheric current source. The background of these computations is based on fundamental principles of electromagnetism. The relationship between the electric field ($\mathbf{E}$), magnetic field ($\mathbf{B}$) and the current density ($\mathbf{J}$) are best described by Maxwell's equations and Ohm's law:

$$\nabla \cdot \mathbf{E} = \frac{\rho}{\epsilon} \tag{2.1}$$

$$\nabla \cdot \mathbf{B} = 0 \tag{2.2}$$

$$\nabla \times \mathbf{E} = -\frac{\partial \mathbf{B}}{\partial t} \tag{2.3}$$

$$\nabla \times \mathbf{B} = \mu_0 \mathbf{J} + \mu_0 \epsilon \frac{\partial \mathbf{E}}{\partial t} \tag{2.4}$$

$$\mathbf{J} = \sigma \mathbf{E} \tag{2.5}$$

where ρ is the charge density, ϵ is the permittivity, μ_0 is permeability and σ is the conductivity.

The magnetic permeability of vacuum, $\mu_0 = 4\pi \cdot 10^{-7}$ in Hm^{-1} is applied in all computations as is done in most of the relevant literature. To justify the quasi-stationary approximation of the electric field we take the curl of equation 2.3 and a combination of equations 2.4 and 2.5. If a characteristic time T of a particular event is taken into consideration and $t' = \frac{t}{T}$, equation 2.6 becomes equation 2.7

$$\nabla^2 \mathbf{E} = \nabla(\nabla \cdot \mathbf{E}) + \mu_0 \sigma \frac{\partial \mathbf{E}}{\partial t} + \mu_0 \epsilon \frac{\partial^2 \mathbf{E}}{\partial^2 t} \tag{2.6}$$

$$\nabla^2 \mathbf{E} = \nabla(\nabla \cdot \mathbf{E}) + K_1 \frac{\partial \mathbf{E}}{\partial t'} + K_2 \frac{\partial^2 \mathbf{E}}{\partial^2 t'} \tag{2.7}$$

where $K_1 = \frac{\mu_0 \sigma}{T}$ and $K_2 = \frac{\mu_0 \epsilon}{T^2}$. For typical values of free space and ground permittivity over the range of frequencies of GIC, $\frac{K_1}{K_2}$ is of the order 10^8 thus $K_1 \gg K_2$. This condition justifies neglecting the last term of equation 2.7. If the current density $\mathbf{J}$ is assumed to be divergence free, equation 2.5 gives:

$$(\nabla \sigma) \cdot \mathbf{E} + \sigma \nabla \cdot \mathbf{E} = 0 \tag{2.8}$$

Furthermore, if $\nabla \sigma = 0$ in the direction of the electric field, $\nabla \cdot \mathbf{E} = 0$. Substituting $\nabla \cdot \mathbf{E} = 0$ into equation 2.7 we obtain equation 2.9, known as the vector diffusion equation of the electric field. Also in a uniform conductor, the magnetic field can be shown to satisfy the diffusion equation expressed as equation 2.10 (Pulkkinen, 2003).

$$\nabla^2 \mathbf{E} = \mu_0 \sigma \frac{\partial \mathbf{E}}{\partial t} \tag{2.9}$$

$$\nabla^2 \mathbf{B} = \mu_0 \sigma \frac{\partial \mathbf{B}}{\partial t} \tag{2.10}$$

The equations outlined above show that the electric field in the Earth is diffusive rather than propagating as a wave. The vertical component of the electric field is always zero and the Earth's electric field is always horizontal if there are no horizontal variations in the conductivity of the Earth.

2.5.2 Computing the geoelectric field from ionospheric current models

The computation of the geoelectric field using the ionospheric current models requires knowledge of the Earth's conductivity profile. Several techniques have been established to achieve adequately realistic results in either 1D or 2D. Among these methods, two have gained preference, namely, the Complex Image Method (CIM) (Pirjola and Viljanen, 1998) and the Method of Auxiliary Sources (MAS) (Shepherd and Shubitidze, 2003). Results from these techniques are compared to the exact solution obtained from solving Maxwell's equation. Equations 2.11 to 2.13 are derived by (Hermance and Peltier, 1970) to give the exact solution of the geoelectric and magnetic field on the Earth's surface.

$$B_x = -\frac{\mu_0 I}{2\pi} \int_0^\infty (1 + R) \exp(-h\nu) \cos \nu x d\nu \tag{2.11}$$

$$B_z = -\frac{\mu_0 I}{2\pi} \int_0^\infty (1 - R) \exp(-h\nu) \sin \nu x d\nu \tag{2.12}$$

$$E_y = \frac{j\omega\mu_0 I}{2\pi} \int_0^\infty \frac{1}{\nu} (1 - R) \exp(-h\nu) \cos \nu x d\nu \tag{2.13}$$

where R is the reflection coefficient of the Earth's conductivity structure, I is the magnitude of the current, ω is the frequency, x is the horizontal distance from the current source along the Earth's surface and ν is a spatial integration variable associated with the Fourier decomposition of the line current (Shepherd and Shubitidze, 2003).

The application of CIM in the calculation of the geoelectric and magnetic fields produced by an auroral electrojet of finite length is presented by Pirjola and Viljanen (1998) and Boteler and Pirjola (1998*b*). The primary electromagnetic field is reflected from the interface between two different media and, hence, forms a secondary field. The currents induced in the Earth are represented by an image current at a complex distance below the primary line current (see Figure 2.15). This method is limited to 1D layered Earth models. The CIM solution has so far given realistic estimates of GIC in the power system. The equations derived for the magnetic and electric fields due to a given line current source are as follows:

$$B_x = \frac{\mu_0 I}{2\pi}\left(\frac{h}{h^2+x^2} + \frac{h+2p}{(h+2p)^2+x^2}\right) \tag{2.14}$$

$$B_z = -\frac{\mu_0 I}{2\pi}\left(\frac{x}{h^2+x^2} - \frac{x}{(h+2p)^2+x^2}\right) \tag{2.15}$$

$$E_y = -\frac{j\omega\mu_0 I}{2\pi}\ln\left[\frac{\sqrt{(h+2p)^2+x^2}}{\sqrt{h^2+x^2}}\right] \tag{2.16}$$

$$p = \frac{Z}{j\omega\mu_0} \tag{2.17}$$

where h is the height of the line current, p is the complex skin depth given by 2.17 and $Z = \frac{-E_y}{H_x}$ which is the surface impedance.

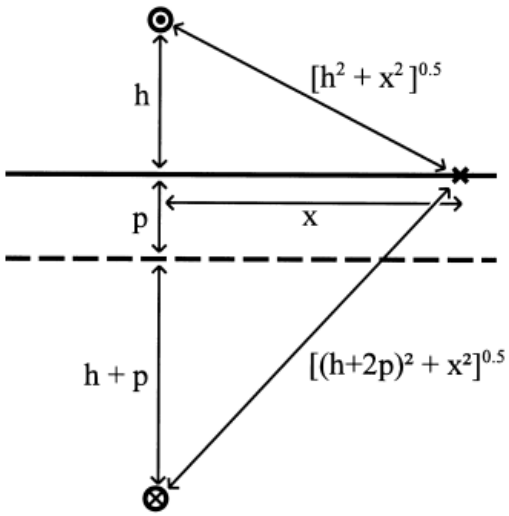

Figure 2.15: Line current representation of the auroral electrojet and the position of an image current at a complex depth used to represent the effect of induced currents in the Earth. Adopted from (Boteler and Pirjola, 1998*b*).

While the CIM is limited to 1D geomagnetic induction problems, another numerical technique, i.e. the MAS method can be used. 2D and 3D geomagnetic induction problems can be handled with MAS. The horizontal variation of the Earth's conductivity can be accommodated in the computations. Figure 2.16 illustrates the application of the MAS for the simplest case of a single-layer Earth model.

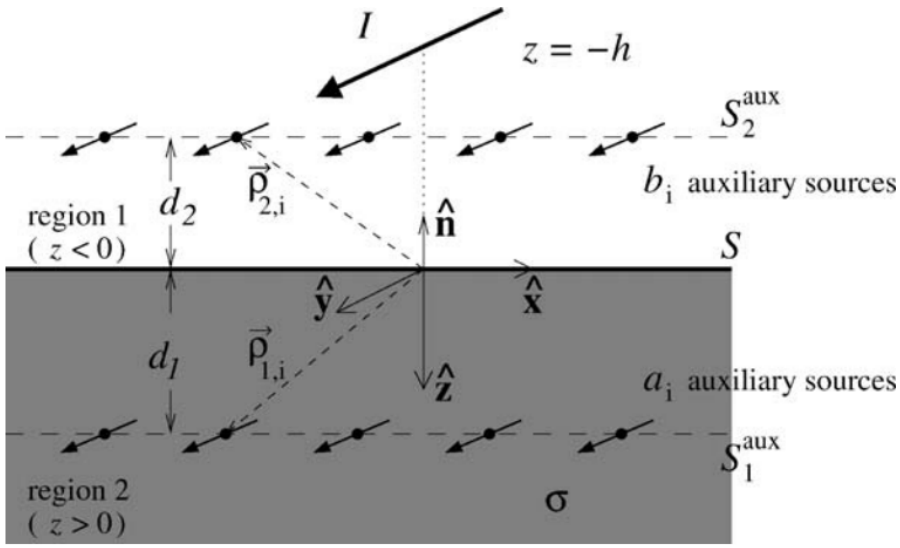

Figure 2.16: Quasi-3D geometry for application of the MAS to a 1D single-layer Earth conductivity model. Adopted from (Shepherd and Shubitidze, 2003).

In Figure 2.16, a current I is located at a height h above the Earth's surface. The current is directed in the $+\hat{y}$ direction and extends to infinity in both $\pm\hat{y}$. In 2D, the electric field has no y variation. The auxiliary surfaces ${S^{aux}}_1$ and ${S^{aux}}_2$ are required to describe the electric field in region 1 and 2, respectively. If a vector potential ($\mathbf{A}$) is considered according to Maxwell's equations, for the regions 1 and 2 indicated on the figure, equations 2.18 and 2.19 hold.

$$\nabla^2 \mathbf{A}_1 = 0 \tag{2.18}$$

$$\nabla^2 \mathbf{A}_2 - j\omega\mu\sigma\mathbf{A}_2 = 0 \tag{2.19}$$

where $\mu = \mu_0\mu_r$ is the permeability of the Earth, μ_r is the relative permeability, σ is the Earth's conductivity. The magnetic and electric fields in regions 1 and 2 are expressed by equations 2.20 and 2.21.

$$\mathbf{H}_\alpha = \nabla \times \mathbf{A}_\alpha \tag{2.20}$$

$$\mathbf{E}_\alpha = j\omega\mathbf{A}_\alpha \tag{2.21}$$

where $\alpha = 1$ or 2 and $B = \mu_0\mathbf{H}$. The boundary conditions applied in the computations are:

$$\hat{\mathbf{n}} \times ({\mathbf{H}_1}^{sc} + \mathbf{H}^{pr}) = \hat{\mathbf{n}} \times \mathbf{H}_2 \tag{2.22}$$

$$\hat{\mathbf{n}} \cdot ({\mathbf{H}_1}^{sc} + \mathbf{H}^{pr}) = \hat{\mathbf{n}} \cdot \mathbf{H}_2 \tag{2.23}$$

where $\mathbf{H}^{pr}$ is the primary magnetic field due to the line current I, $\mathbf{H}^{sc}{}_1$ is the reflected magnetic field due to Earth currents and $\mathbf{H}_2$ is the total field in the Earth. In this case, the permeability of the vacuum was assumed hence the continuity of the tangential component of $\mathbf{H}$ implies the continuty of the normal component the tangential component of $\mathbf{B}$.

$$\mathbf{H}^{sc}{}_1(\rho) = \sum_{j=1}^{N} \mathbf{H}^{sc}_{1,i}(\rho, \rho_{1,i}) = \sum_{j=1}^{N} \nabla \times \mathbf{A}^{sc}_{1,i}(\rho, \rho_{1,i}) \tag{2.24}$$

where $\mathbf{H}^{sc}_{1,j}(\rho, \rho_{1,i})$ is the magnetic field due to the auxiliary current a_i and $\mathbf{H}_{2,i}(\rho, \rho_{2,i})$ is the magnetic field due to the auxiliary current b_i. The terms $\mathbf{A}^{sc}_{1,i}(\rho, \rho_{1,i})$ and $\mathbf{A}_{2,i}(\rho, \rho_{2,i})$ are solutions to equations 2.18 and 2.19, respectively. The total field in region 1 is a sum of H^{pr} and H^{sc}_1 where the field potentials are expressed as:

$$\mathbf{A}^{sc}_{1,i}(\rho, \rho_{1,i}) = \frac{a_i}{4\pi} \ln |\rho - \rho_{1,i}| \hat{y} \tag{2.25}$$

$$\mathbf{A}^{pr}_{1}(\rho) = \frac{I}{4\pi} \sqrt{x^2 + (z+h)^2} \hat{y} \tag{2.26}$$

The total field in region 2 is expressed as:

$$\mathbf{H}_2(\rho) = \sum_{j=1}^{N} \mathbf{H}_{2,i}(\rho, \rho_{2,i}) = \sum_{i=1}^{N} \nabla \times \mathbf{A}_{2,i}(\rho, \rho_{2,i}) \tag{2.27}$$

where

$$\mathbf{A}_{2,i}(\rho, \rho_{2,i}) = \frac{b_i}{4\pi} K_0(\sqrt{-i\omega\sigma\mu}|\rho - \rho_{2,i}|\hat{y}) \tag{2.28}$$

and K_0 the modified zero order Bessel function.

2.5.3 Computing the geoelectric field from the geomagnetic field

When the horizontal electric field components are derived from the local geomagnetic field, the magnetotelluric theory Tis usually adopted. The theory has its roots in Faraday's law, equation 2.3. The vertical component of the induced electric field $E_z = 0$, hence, only computations for E_x and E_y are required. B_x and B_y are therefore considered to be sufficient for the computation of E_x and E_y in the Earth's surface. A plane wave model was found to be sufficient in these computations, especially with 1D Earth models. The assumption is that the plane wave propagates vertically downwards to the Earth. The Earth is represented by a single or multiple planar layers (Viljanen *et al.*, 2004; Thomson *et al.*, 2009; Pirjola, 2010). The process of GIC modelling from the geomagnetic field can be summarised by the flow diagram in Figure 2.17.

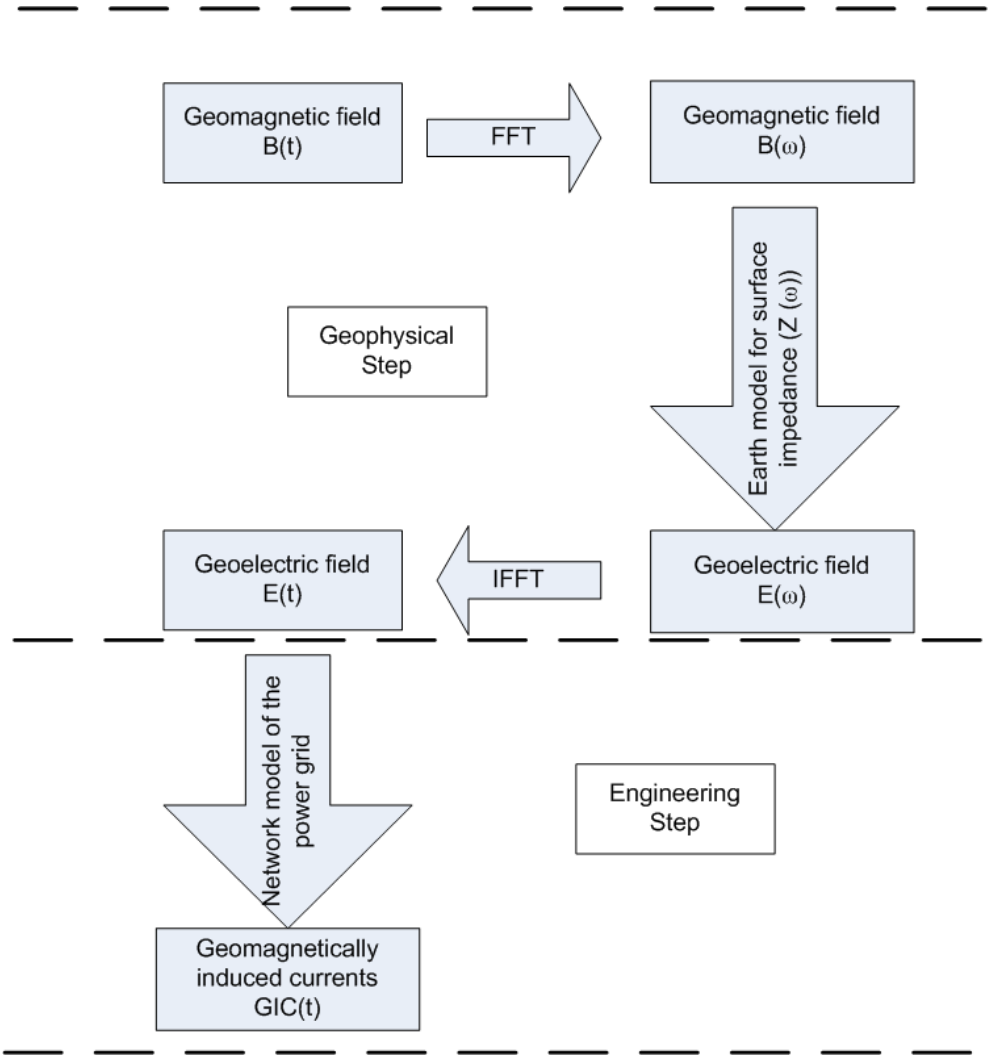

Figure 2.17: Flow diagram for modelling GIC from geomagnetic data. Adapted from (Zheng *et al.*, 2013).

If a Cartesian coordinate system with the Earth's surface is the xy plane, x axis points northwards, y axis eastwards and z axis downwards is used and a single angular frequency ω is considered, the horizontal components of the geoelectric and geomagnetic fields are expressed as equations 2.29 and 2.30 (Pulkkinen, 2003):

$$\overrightarrow{E}_i(t) = \overrightarrow{E_0} \exp i(\omega t - k_0 z) \tag{2.29}$$

$$\overrightarrow{B}_i(t) = \overrightarrow{B_0} \exp i(\omega t - k_0 z) \tag{2.30}$$

where

$$\overrightarrow{E_0} = E_x \hat{x} + E_y \hat{y} \tag{2.31}$$

$$\overrightarrow{B_0} = B_x \hat{x} + B_y \hat{y} \tag{2.32}$$

where $\hat{x}$, $\hat{y}$ and $\hat{z}$ are unit vectors pointing in the x, y and z directions, respectively, and k_0 is the free-space propagation constant given by $\frac{2\pi}{\lambda}$ ($\lambda is the wavelength$). $In conducting media k_0$ is replaced by $k = \frac{(1-i)}{\delta}$ where δ is the skin depth given by:

$$\delta = \sqrt{\frac{2}{\omega\mu\sigma}}. \tag{2.33}$$

Equation 2.33 applies to a homogeneous, half space Earth model. Two boundary conditions apply at the boundary between the air and the Earth; the horizontal component of the electric field and the magnetic field are both continuous at $z = 0$. This consideration therefore implies that:

$$\frac{E_x}{B_y} = \sqrt{\frac{\omega}{\mu_0\sigma}}\exp(i\frac{\pi}{4}) \tag{2.34}$$

$$\frac{E_y}{B_x} = -\sqrt{\frac{\omega}{\mu_0\sigma}}\exp(i\frac{\pi}{4}) \tag{2.35}$$

which is the basic magnetotelluric equation as defined by Cargniard, (1953), with $Z(\omega)$ the surface impedance.

Equations 2.34 and 2.35 are also represented in terms of the surface impedance $Z(\omega)$ by

$$E_y(\omega) = -\frac{Z(\omega)}{\mu_0}B_x(\omega) \tag{2.36}$$

$$E_x(\omega) = \frac{Z(\omega)}{\mu_0}B_y(\omega) \tag{2.37}$$

The inverse Fourier transform of equations 2.34 and 2.35 can be expressed by

$$E_y(t) = -\frac{1}{\sqrt{\pi\mu_0\sigma}}\int_{-\infty}^{t}\frac{g_x(u)}{\sqrt{t-u}}du \tag{2.38}$$

and

$$E_x(t) = \frac{1}{\sqrt{\pi\mu_0\sigma}}\int_{-\infty}^{t}\frac{g_y(u)}{\sqrt{t-u}}du \tag{2.39}$$

where $g_{(x,y)}$ are the time derivatives of $B_{x,y}$ i.e. $\partial B_{x,y}/\partial t$ (Viljanen and Pirjola, 1989).

Equations 2.38 and 2.39 are not practical as there is no $-\infty$ in practical measurements of the magnetic field. The solution is approximated by assuming that $-\infty$ can be replaced by a finite time equal to $M\Delta$ where Δ is the sampling interval and M is the number of the previous samples of the magnetic field considered in the computation of the electric field. M should be sufficiently large. The integral in equation 2.39 can be approximated by a sum of a finite number of terms by assuming an instantaneous value in the middle of the measurement interval, such that the magnetic field is expressed as:

$$B(t) = B_{n-1} + (B_n - B_{n-1})(t - T_{n-1})/\Delta, T_{n-1} \leq t \leq T_n \tag{2.40}$$

where $B_n = B(T_n)$ is the average value of either B_x or B_y over the interval $T_n - \Delta/2$ to $T_n + \Delta/2$ and $\Delta = T_n - T_{n-1}$. The time derivatives of the magnetic field are given by the expression

$$g(t) = \frac{(B_n - B_{n-1})}{\Delta}, T_{n-1} < t < T_n \tag{2.41}$$

If M values are considered, the geoelectric field at the sample time T_n is given by the expression

$$E(T_n) = \frac{1}{\sqrt{\pi\mu_0\sigma}} \int_{T_n - M\Delta}^{T_n} \frac{g(u)}{\sqrt{T_n - u}} du \tag{2.42}$$

If the integral is expanded, the result is equation 2.43

$$E(T_N) = \frac{1}{\sqrt{\pi\mu_0\sigma}} \left\{ \sum_{n=N-M+1}^{N} \frac{B_n - B_{n-1}}{\Delta} \int_{T_{n-1}}^{T_n} \frac{1}{\sqrt{T_N - u}} du \right\} \tag{2.43}$$

The integral identity below is applied to equation 2.43 and the geoelectric field can be expressed by equation 2.44.

$$\begin{aligned} \int_{T_{n-1}}^{T_n} \frac{1}{\sqrt{T_N - u}} du &= -2 \left[\sqrt{T_N - u} \right]_{T_{n-1}}^{T_n} \\ &= -2 \left\{ \sqrt{T_N - T_n} - \sqrt{T_N - T_{n-1}} \right\} \\ &= -2\sqrt{\Delta} \left\{ \sqrt{N - n} - \sqrt{N - (n-1)} \right\} \end{aligned}$$

$$E(T_N) = \frac{-2}{\sqrt{\pi\mu_0\sigma\Delta}} \left\{ \sum_{n=N-M+1}^{N} (B_n - B_{n-1}) \left(\sqrt{N - n} - \sqrt{N - (n-1)} \right) \right\} \tag{2.44}$$

2.6 GIC calculation

The calculation of GIC in the power system is known as the engineering step. The modelling of GIC in power systems once depended on tools such as the Electromagnetic Transient Program (EMTP) (Albertson *et al.*, 1981; Dommel, 1986). Lehtinen and Pirjola (1985) developed a stand-alone method (LP method) to calculate GIC for a discretely earthed network, such as a power system. This method has been vastly used in various power systems. Other methods, namely the Mesh Impedance Matrix method (MIM) and the Nodal Admittance Matrix method (NAM) are also used to calculate GIC in the power network (Boteler, 2014; Boteler and Pirjola, 2014; Pirjola, 2007). For a power system represented as an impedance network with the voltage sources, the MIM method is used, while, the LP and NAM method are applied if the power system can be represented as an admittance network and current sources. The Lehtinen-Pirjola (LP) method and the NAM method are mathematically equivalent (Boteler and Pirjola, 2014) and computationally more efficient than MIM.

From these methods, if the electric field is assumed to be spatially uniform, the calculation of the GIC is simplified and equation 2.45 is used.

$$I_{GIC}(t) = aE_x(t) + bE_y(t) \tag{2.45}$$

where the a and b are network coefficients, E_x is the northward electric field and E_y is the eastward electric field.

From the LP method, these network coefficients can be derived from the knowledge of the network configuration, i.e. topology, transformer and transmission line resistances and the substation earthing resistances. The column vector [**I**] in equation 2.46 gives the earthing currents (Viljanen *et al.*, 2012; Viljanen and Pirjola, 1994; Lehtinen and Pirjola, 1985).

$$[\mathbf{I}] = ([\mathbf{1}] + [\mathbf{Y}][\mathbf{Z}])^{-1}[\mathbf{J}] \tag{2.46}$$

where [**1**] is the unit matrix, [**Y**] is the network admittance matrix , [**Z**] is the earthing impedance matrix and [**J**] is the column matrix of equivalent current sources at the earthing points. The a and b network coefficients are given by equation 2.47 and 2.48, respectively.

$$[\mathbf{a}] = ([\mathbf{1}] + [\mathbf{Y}][\mathbf{Z}])^{-1}[J_x] \tag{2.47}$$

$$[\mathbf{b}] = ([\mathbf{1}] + [\mathbf{Y}][\mathbf{Z}])^{-1}[\mathbf{J}_y] \tag{2.48}$$

where $[\mathbf{J}_x]$ is the column matrix of the equivalent current sources for a northward electric field on 1 V/km, and $[\mathbf{J}_y]$ is the column matrix of the equivalent current sources for eastward electric field of 1 V/km.

It is possible to derive the network coefficients, empirically without the knowledge of the network configuration, from the calculated electric field as well as the measured GIC (Zhang *et al.*, 2012; Ngwira *et al.*, 2008; Pulkkinen *et al.*, 2007).

2.7 GIC mitigation

With the ongoing research on the effects of GIC on power system, some methods of mitigating these effects have been established. These methods can either completely eliminate or reduce the chances of GIC flowing into the power system. The introduction of series capacitors in the transmission network (as illustrated in Figure 2.18) is expected to block any flow of GIC within the network completely. While this method would present an ideal solution, it is costly, especially at high voltage transmission lines and hence, not adopted in many systems. In most systems where these capacitors are incorporated, their primary role is to enhance the stability of the AC transmission system and the blocking of GIC is a secondary benefit. An alternative way is to introduce low voltage capacitors on the neutral to ground terminal connection as shown in Figure 2.19.

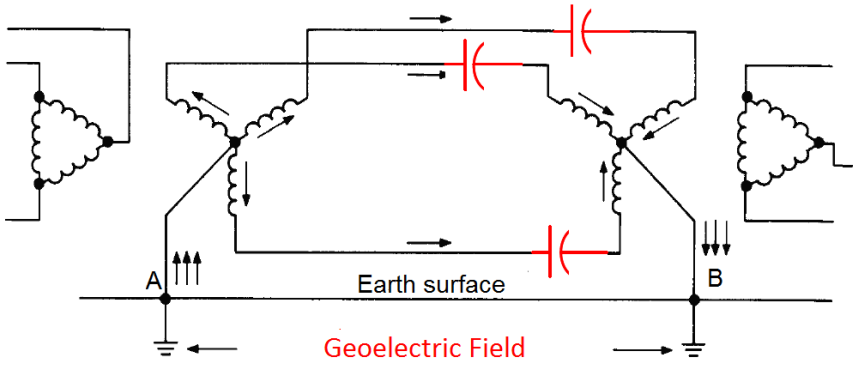

Figure 2.18: Introduction of series capacitors on the transmission lines to block GIC flow in a network.

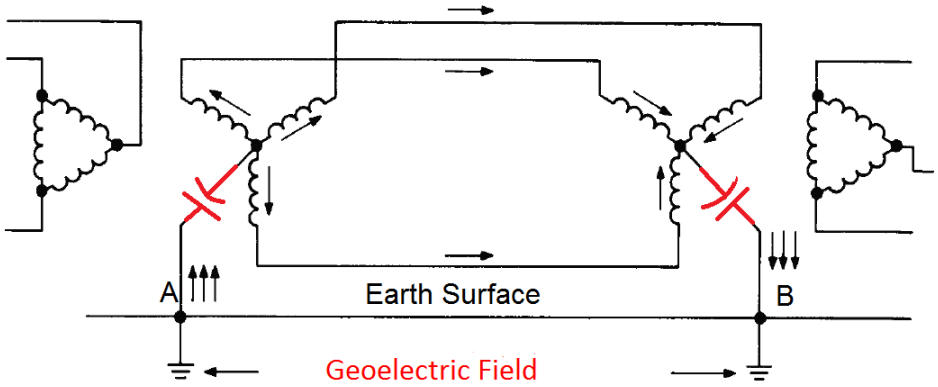

Figure 2.19: Introduction of capacitors on the neutral to ground terminal to block GIC flow in a network.

The reduction of the GIC in the system can also be achieved by introducing a low-ohmic resistor in the neutral-to-ground terminal as illustrated in Figure 2.20. This will reduce the flow of GIC into the system.

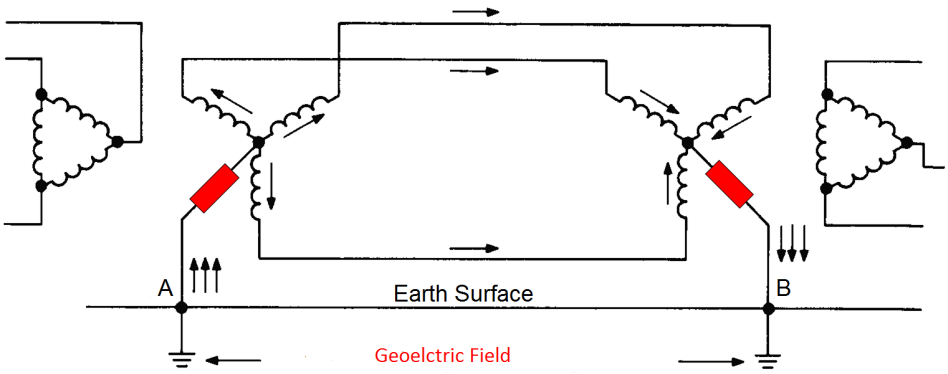

Figure 2.20: Introduction of low-ohmic resistors in the neutral-to-ground terminals to reduce GIC flow in a network.

2.8 Conclusion

This chapter discussed the space physical and geophysical background of the occurrence of GIC and also the impacts of GIC on power systems. Some methods that can be used to calculate the electric field associated with GIC from modelled or measured magnetic field have been outlined. The chapter also highlighted methods that can be employed by power utilities to reduce the flow of GIC into the power system. A summary of the GIC calculation techniques is also given in this chapter.

CHAPTER 3: MEASUREMENT OF GIC IN THE POWER LINE USING THE DIFFERENTIAL MAGNETOMETER METHOD

3.1 Introduction

Geomagnetically induced currents (GIC) are traditionally measured in the neutral-to-ground connections of high voltage power transformers. There is a need to determine the characteristics of GIC in high voltage power lines in order to verify GIC models. The GIC are low frequency currents and can, therefore, not be measured using current transformers (CT). A method that uses a set of two magnetometers to infer the GIC in the power line is discussed in this chapter. This chapter presents the algorithm and the instruments used for the differential magnetometer method (DMM) in Southern Africa.

3.2 Principles of the differential magnetometer method (DMM)

The DMM is an indirect way of estimating GIC in power lines using magnetic field measurements. Two magnetometers are used to record the magnetic field variations in the vicinity of the power line. One magnetometer is placed directly under the power line and the other is placed some distance away, as shown in Figure 3.1. The principle of operation of the DMM is that the magnetometer under the power lines (at P1) will measure both the magnetic field induced by telluric currents and the magnetic field induced by GIC in the power line. The telluric currents are induced in the Earth by the magnetic field variations which can be enhanced during geomagnetic storms. The magnetic field due to the telluric currents is obtained by subtracting the quiet-time magnetic field at the location of interest from the total geomagnetic field. The second magnetometer, placed at a certain distance away (at P2) should measure the surrounding magnetic field which is not influenced by the current in the power line (Viljanen *et al.*, 2009; Campbell and Zimmerman, 1980). The second magnetometer should be far enough that the magnetic field due to the GIC in the power line will be less than 1 % of the magnetic field due to telluric currents but not too far in order that the other transient variations of the geomagnetic field can be considered equal. The difference between the measured fields will be treated as the contribution of the quasi-DC current flowing in the power line.

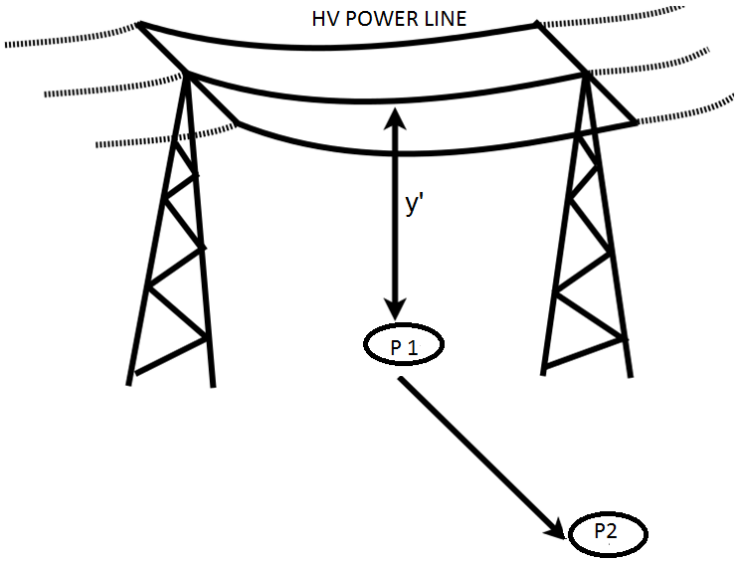

Figure 3.1: Differential magnetometer measurement set up for estimating GIC in a power line: P1 is the magnetometer under the power line of which the lowest point is at a height y', P2 is an identical magnetometer some distance away from the power line.

The power lines usually run in a three-phase configuration. A typical geometry is shown in Figure 3.2.

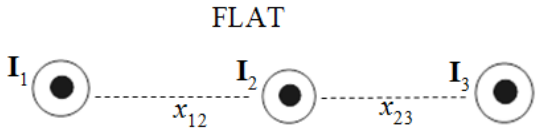

Figure 3.2: Typical 3-phase overhead line configuration.

The Biot-Savart law is used to calculate the magnetic field contribution $d\mathbf{B}$ from its source of current $Id\mathbf{s}$, where $d\mathbf{s}$ represents a short section of the line. The magnetic field contribution is expressed as

$$\mathbf{B} = \frac{\mu_0}{4\pi} \frac{Id\mathbf{s} \times \hat{\mathbf{r}}}{r^2} \tag{3.1}$$

For a conductor of finite length, as illustrated in Figure 3.3, the magnetic field at the point **P** on the ground (in free space) is calculated by considering the symmetry of the situation where $\theta_2 = \theta_1$. If the conductor is of length 2L, the magnetic field (**B**) due to the current (**I**) at the point **P** is given by equation 3.2,

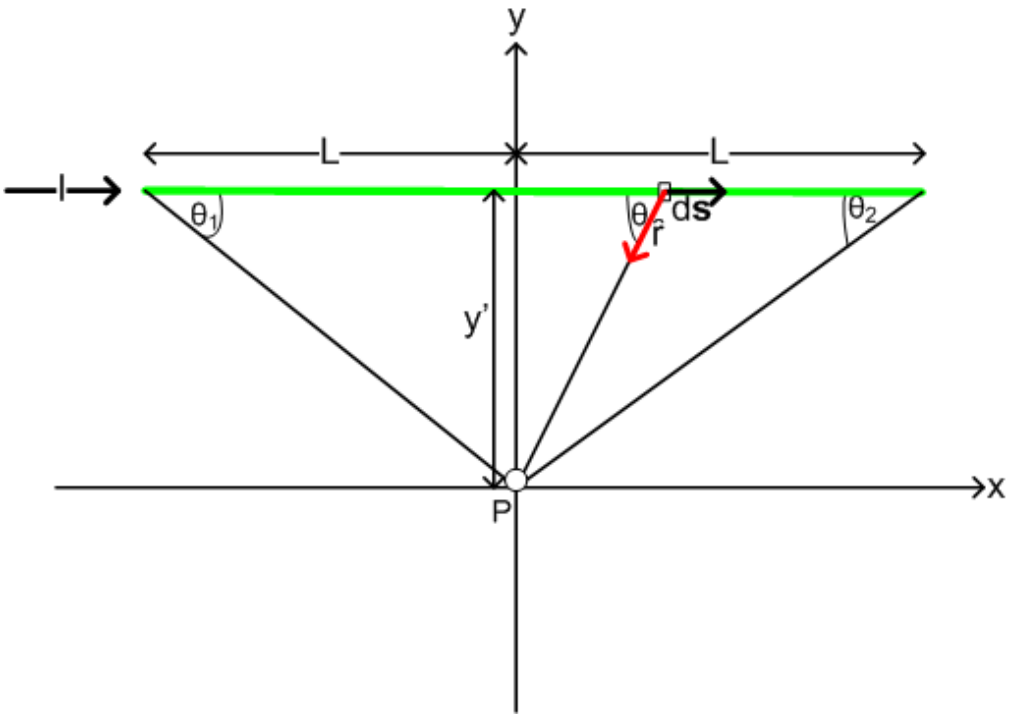

Figure 3.3: Geometry used for the application of the Biot-Savart law: A thin conductor of length 2L, at a height y' above the ground.

$$\mathbf{B} = \int_{-L}^{L} d\mathbf{B} dx = \frac{\mu_0 \mathbf{I}}{2\pi y'} \frac{L}{\sqrt{L^2 + y'^2}} \tag{3.2}$$

where y' is the distance below the conductor and μ_0 is the permeability of free space.

When applying the Biot-Savart law in this technique, the power line is treated as a very long straight current conductor $L >> y'$, for which equation 3.2 can be approximated by equation 3.3. However, the result from equation 3.4 is an approximation. The power line in reality is not a straight line and the geometry of the three phase with respect to the magnetometer are different. It will be sufficient to estimate GIC (I_{GIC}) as the total current in all three parallel conductors of the power line as this would be the expected current measured at the transformer neutrals. The component of the magnetic field perpendicular to the line is given by

$$B_{\perp} = \frac{\mu_0 I}{2\pi h} \tag{3.3}$$

where, h is the distance from the center of the center power line to the magnetometer as shown in Figure 3.2. The GIC in the power is then estimated by equation 3.4

$$I_{GIC} = \frac{2\pi h B_{\perp}}{\mu_0} \tag{3.4}$$

It is expected that the GIC in the power line produce a secondary magnetic field in the Earth, as given by the second term in equation 3.5 which, applies to the computation of the magnetic field due

to an infinite line current source using the CIM method (Boteler and Pirjola, 1998*b*). The second term of the equation is neglected in the computation of the GIC due to the fact that the power line height (h) is much less than the absolute value of the skin depth (p) in the Earth (Viljanen *et al.*, 2009). The magnetic field along the horizontal distance from the power line is given as

$$B_{\perp} = \frac{\mu_0 I}{2\pi}\left(\frac{h}{h^2+x^2} + \frac{h+2p}{(h+2p)^2+x^2}\right) \tag{3.5}$$

For $\sigma = 0.001$ S/m at a frequency of 0.001 Hz, $p = 300$ km, hence the second term of equation 3.5 is negligible; thus, the remaining term is the expression as defined by the Biot-Savart law (equation 3.2 and 3.3).

3.3 Instrumentation

The instrumentation for the execution of the DMM requires the following components:

1. two vector magnetic sensor
2. data logging unit
3. power supply

3.3.1 Magnetic sensors

Two identical tri-axial magnetic sensors were used in this project. Low cost magnetometers were preferred to facilitate the deployment of the measurement system at several points in the region to form a network that enhances GIC research in Southern Africa. The selection of the sensors were based on cost, specifications from manufacturers and the availability of the sensor during the time of research.

The two magnetometers selected were both fluxgate magnetometers manufactured by Lviv Centre of Institute for Space Research,[1] namely the LEMI-417 and LEMI-011. Fluxgate magnetometers generate an electrical signal that is proportional in magnitude to the intensity of the external magnetic field along the axis. Fluxgate magnetometers are used in the measurement of direct current (DC) or low frequency alternating current (AC) magnetic fields (Ripka and Ripka, 2007). Fluxgate sensors combine good sensitivity, high stability and linearity, and as such they are preferred above any magneto-resistive or semiconductor magnetic sensors in applications of low frequency magnetic field measurements (Forslund *et al.*, 2008).

3.3.2 Recommended magnetic sensor characteristics

This section lists characteristics of a magnetic sensor which are to be considered when selecting a magnetometer for a DMM application.

- *Vector vs. absolute measurement*: A three-axis vector magnetometer is preferred when measuring GIC using DMM. This allows for extraction of the horizontal component perpendicular to the power line.

[1] www.isr.lviv.ua

- *Bandwidth*: The bandwidth of the magnetometer must be well below 50 Hz since GIC have a frequency band of 0.1-10 mHz. It is best to use a magnetometer with a low pass filter, which has a cutoff frequency well below 50 Hz, so that the magnetic field due to the 50 Hz current is sufficiently suppressed.

- *Temperature sensitivity*: A magnetometer with a low sensitivity for temperature variation over a wide operational temperature range is recommended. Since the magnetometers are buried underground, temperature fluctuations are expected to be reduced.

- *Dynamic range*: A wide measurement range is necessary to allow the magnetometer to record high levels of dynamic magnetic field without reaching saturation.

3.3.2.1 The LEMI-417 magnetotelluric device

The LEMI-417 is a magnetotelluric (MT) instrument that consists of an electrometer with four electrodes and a tri-axial fluxgate magnetometer, as shown in Figure 3.4. The electrodes are used to measure the geoelectric field. The ability of the MT to measure both the magnetic field and the electric field (induced by the time varying magnetic field), makes it possible to determine the surface impedance of the Earth at that point (Chave and Jones, 2012). The LEMI-417 comes with an advantage of waterproof housing, which facilitates outdoor measurements.

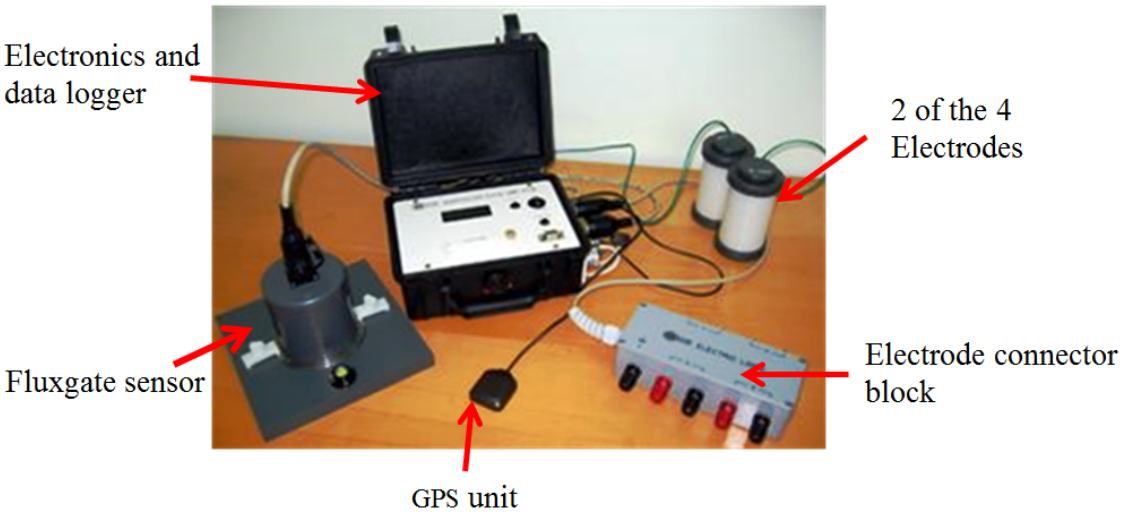

Figure 3.4: LEMI-417 components.

A typical MT measurement set-up is illustrated in Figure 3.5. The measured magnetic field is processed and stored in the built-in memory of the electronic unit and can be transferred to an external device via RS-232 or RS-422 (LEMI, 2011). This makes it easy for data download after a certain period.

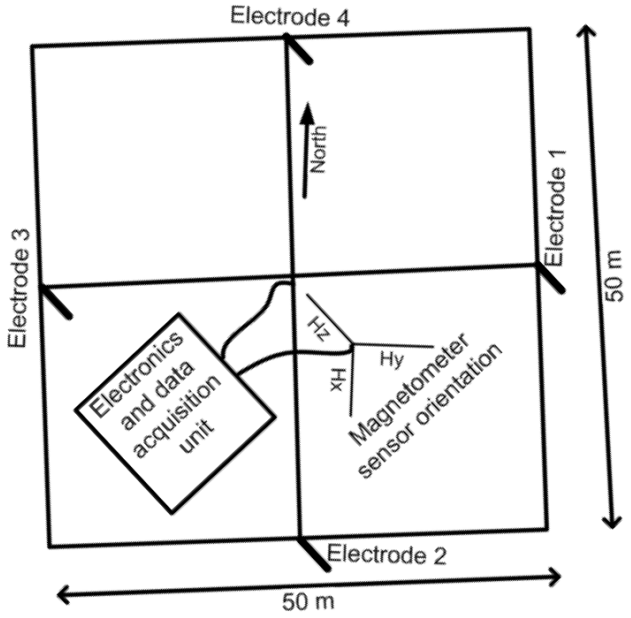

Figure 3.5: Magnetotelluric set-up

3.3.2.2 The LEMI-011 magnetometer

The LEMI-011 is the primary magnetometer chosen for this pilot project. It is a very low cost, light and energy efficient magnetometer, which has demonstrated its robustness and reliability in magnetic measurements. The LEMI-011 was tested inhouse as a candidate for space magnetometry (Matandirotya *et al.*, 2013) and is recommended for the particular project. The technical specification is available at `http://www.lemisensors.com/?q=LEMI-011`. Figure 3.6 shows the inside of a LEMI-011 magnetometer.

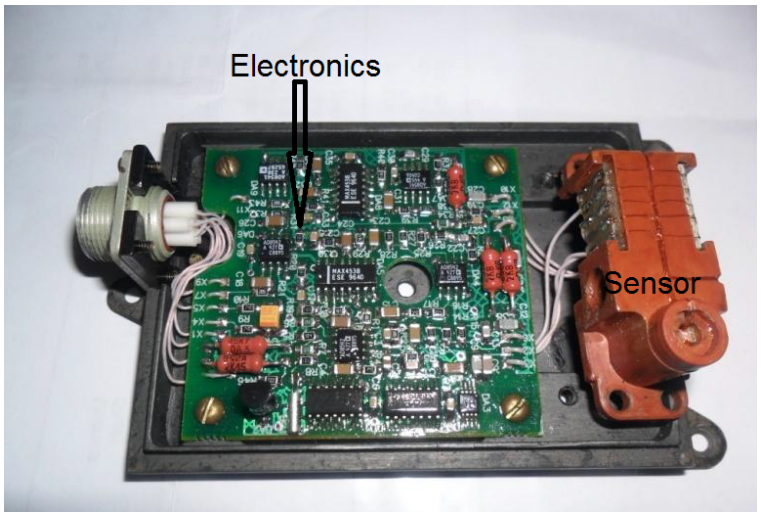

Figure 3.6: The LEMI-011 magnetometer with lid removed.

3.3.2.3 Magnetic sensor calibration

The LEMI-011 was calibrated in the Helmholtz coils of SANSA, Space Science. As discussed by Matandirotya *et al.* (2013), two tests are performed to determine the offsets, sensitivity and

misalignment. These are the *Linearity* and *Thin Shell* tests. The magnetometers were chosen randomly from an available batch. To determine the influence of the battery, data logger and voltage regulating circuit on the magnetometer, calibration was done with all equipment in functional mode. The calibration matrix to convert the measured voltages to calibrated magnetic field values is given in equation 3.6

$$\begin{bmatrix} FieldX \\ FieldY \\ FieldZ \end{bmatrix} = \begin{bmatrix} C_{xx} & C_{xy} & C_{xz} \\ C_{yx} & C_{yy} & C_{yz} \\ C_{zx} & C_{zy} & C_{zz} \end{bmatrix} \times \begin{bmatrix} OutputX \\ OutputY \\ OutputZ \end{bmatrix} - \begin{bmatrix} O_x \\ O_y \\ O_x \end{bmatrix} \tag{3.6}$$

where C_{xx}, C_{yy} and C_{zz} are the sensitivities of the sensor in the x, y and z axes, respectively, and $C_{xy}, C_{xz}, C_{yx}, C_{yz}, C_{zx}, C_{zy}$ are the calibration matrix elements which correct for sensor misalignment. $O_{x,y,z}$ are the offsets of the x, y, z axes. The calibration involved applying a range of known magnetic fields along each of the three orthogonal axes and comparing the output of the magnetometer with the known field values. The magnetometers were first calibrated as stand-alone units (i.e. without the battery and the logging unit connected). This is done to evaluate the magnetic interference due to the extra units surrounding the magnetometers. The measurement results for two magnetometers are presented in Tables 3.1 and 3.2.

Table 3.1: Recording of the sensitivity and offsets of the magnetometer with serial number N70

	Magnetometer only	Full Setup
X		
C_{xx} [nT/mV]	27.48	27.53
O_x [nT]	1276.50	1524.20
Y		
C_{yy} [nT/mV]	27.48	27.44
O_y [nT]	1029.67	3427.4
Z		
C_{zz} [nT/mV]	27.50	27.42
O_z [nT]	1188.18	1300.90

Table 3.2: Recording of the sensitivity and offsets of the magnetometer with serial number N0309

	Magnetometer only	Full Setup
X		
C_{xx} [nT/mV]	27.41	27.48
O_x [nT]	-89.78	-166.02
Y		
C_{yy} [nT/mV]	27.52	27.42
O_y [nT]	-48.56	622.36
Z		
C_{zz} [nT/mV]	27.46	27.48
O_z [nT]	71.43	0.78

3.3.3 Data Logging

A survey was done on affordable data loggers that could be used for this project. Selection was based on affordability, availability during the research period and specifications. A HOBO (HOBO UX120 4-Channel Analog Data Logger - UX120-006M) data logger was selected for this pilot project. Figure 3.7 shows an image of the data logger. This is a portable logger, which has memory that can store data for periods ranging from a week to a year depending on the sampling rate. The specifications are available at `http://www.onsetcomp.com/products/data-loggers/ux120-006m`.

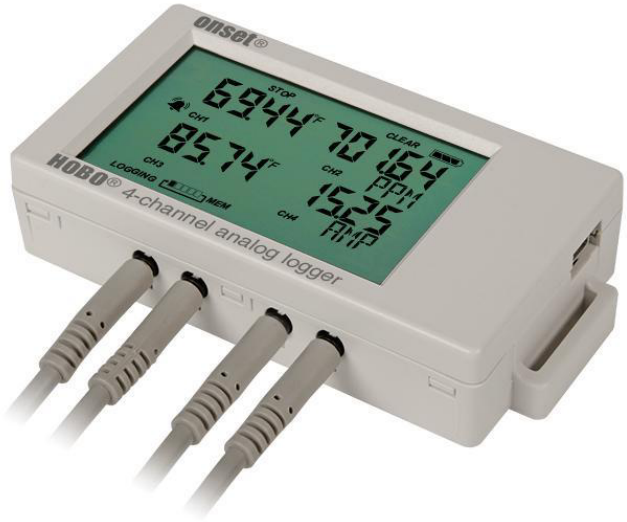

Figure 3.7: HOBO UX120 4-Channel Analog Data Logger - UX120-006M data logger.

3.3.4 Power supply

The data logging unit uses its own built-in 3 V batteries and, hence, only the LEMI-011 magnetometer requires an external power supply. A 12 V/8 Ah battery is used. Due to the LEMI-011 requiring a 5 V input voltage, a voltage regulator circuit was designed. If the identified sites are made permanent and they are secure enough, then solar panels may be considered to

charge the batteries. All the necessary adaptations required for the system to work are discussed in the subsequent section.

3.3.5 System integration

The logger is designed in such a way that specialised cables limit an external voltage exceeding 2.5 V to the internal peak voltage of 2.5 V. To avoid additional cost, the cables were designed in-house. The requirement was to represent -60 000 nT to 60 000 nT with an output of 0 to 2.5 V, as the logger cannot accept negative voltages. The outputs of the 3 axes (x, y, z) of the magnetometer are measured relative to the reference voltage of 2.5 V. Figure 3.8 shows the schematic diagram of the system for the analogue measurements. The system shown includes the design of the voltage reduction cables, as well as a voltage regulator to step down the 12 V to 5 V required by the magnetometer.

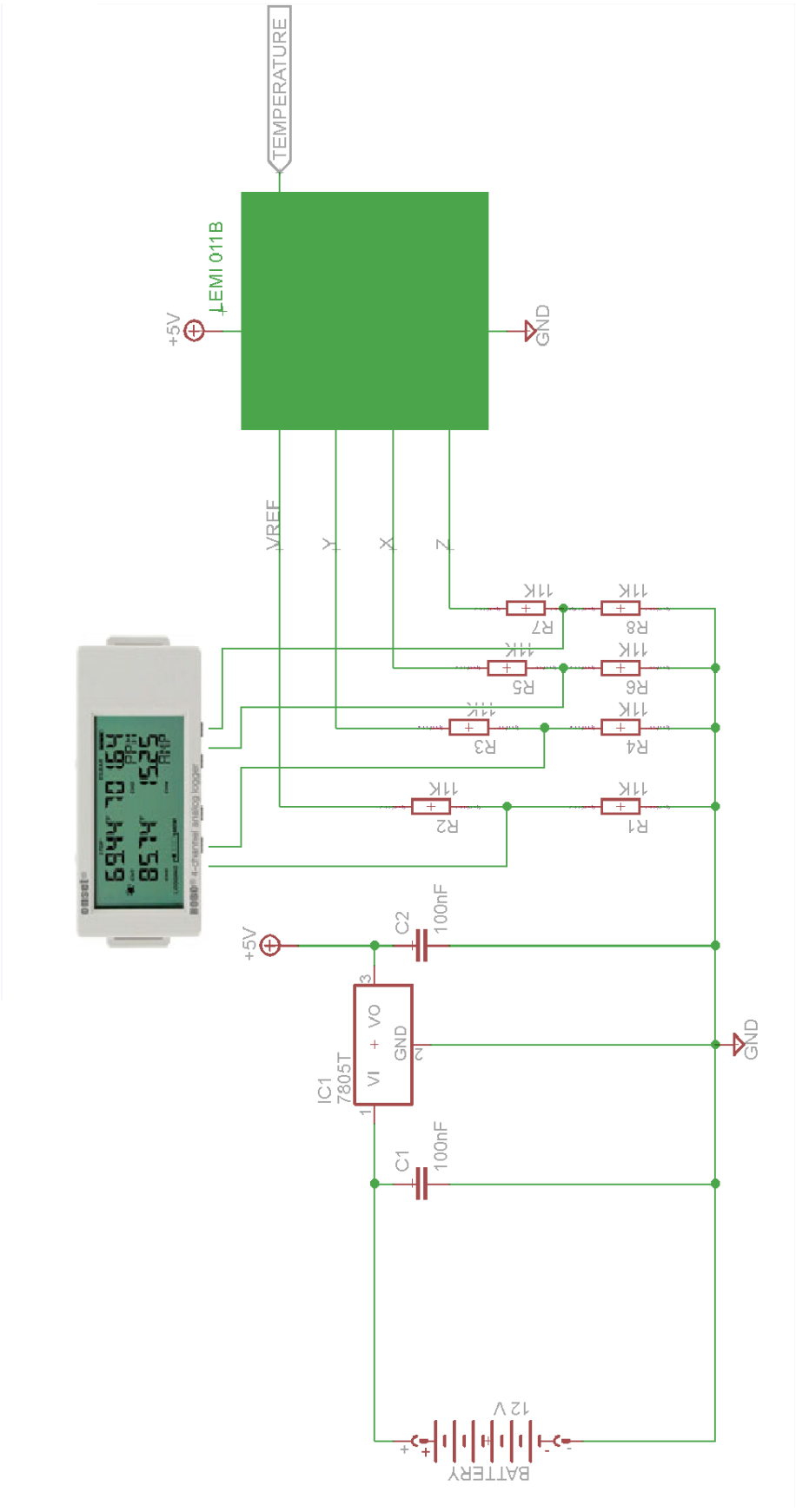

Figure 3.8: Schematic of the fully integrated DMM instrument as modified and tested in-house at SANSA Space Science.

3.3.6 Data processing

The four channels of the logger record the reference voltage and the three voltages (V_x, V_y, V_z) corresponding to the x, y and z components of the magnetic field, respectively. The following steps are taken when manipulating the measured data.

- Launch the HOBO software on the device being used, which can be a laptop or cellphone used in the field.
- Read out the data via the USB connection and save the data file.
- Export the recorded data to a format that one can easily read, for example export to a .cvs file and read with Ms Excel.
- Subtract the reference voltage from the x, y and z recordings.
- Use the calibration matrix to obtain the magnetic field output for each of the x, y, z components.

An example of processed data is presented in Table 3.3

Table 3.3: Processed data from magnetometer measurements captured by logger.

V_{ref} [V]	V_x [V]	V_y [V]	V_z [V]	V_x-V_{ref} [V]	V_y-V_{ref} [V]	V_z-V_{ref} [V]	B_x[nT]	B_y [nT]	B_z [nT]
2.4780	2.1553	2.4781	1.6268	0.3227	-0.0002	0.8512	8842	-4	23321
2.4780	2.1551	2.4783	1.6270	0.3229	-0.0003	0.8511	8846	-8	23317
2.4780	2.1552	2.4782	1.6269	0.3228	-0.0002	0.8511	8844	-6	23317
2.4780	2.1555	2.4780	1.6268	0.3225	0.0000	0.8512	8836	0	23319
2.4780	2.1551	2.4783	1.6268	0.3229	-0.0003	0.8512	8846	-8	23319

NB: The B_z values match that of the INTERMAGNET magnetometer in Hermanus.

3.4 Selected sites

To roll out the pilot project, a survey was done to identify the possible sites where the method could be carried out. The Namibian network was preferred due to the simplicity of the power network structure. The cost of traveling from South Africa to Namibia limited exploring a wide area and, hence, the measurements done in the Namibia were performed during MT installations at Obib. For the South African measurements, the site near Botriver was chosen for its accessibility, security and proximity to Hermanus.

3.4.1 Considerations for selection of a test site

When selecting a site for GIC measurements using the DMM, certain aspects need to be considered in order to enhance accuracy and validity of the measured results.

- An area with minimal man-made magnetic disturbances should be considered. This is to avoid magnetic interference from the man-made influence.

- It should also be possible to have a comparison of the GIC measured on the power lines with those from the transformer neutrals fed by the same power lines. The GIC cannot be measured on certain transformer neutrals as DC compensating series capacitors are installed on the network (Molinski, 2002). The capacitors block the flow of GIC into the transformers to protect the network. The site selected for the DMM measurements should be a power line that terminates in a non-DC compensated substation.

- There should be minimum or negligible natural spatial variation of the geomagnetic field at the magnetometer placement positions. A measurement of the magnetic field gradient should be carried out to determine the geomagnetic gradient.

- Security of the instruments is of great importance as well. Certain measures need to be put in place so that the instruments are secure and the measurements are not disrupted, as these are outdoor measurements.

- The measurement site should also be accessible. This will help in case of trouble shooting and maintenance of the deployed instruments.

Figure 3.9 shows part of the Namibian and South African 400 kV network. The Namibian measurements were done along the power line running from Kokerboom to Obib. For the South African measurements, the line running from Muldersvlei to Bacchus was considered. There are ongoing neutral-to-ground current measurements on the transformers at the Obib and Bacchus substations. Observatories TSU, KMH and HER shown in Figure 3.9 can be used as reference for the magnetic measurements at the chosen sites.

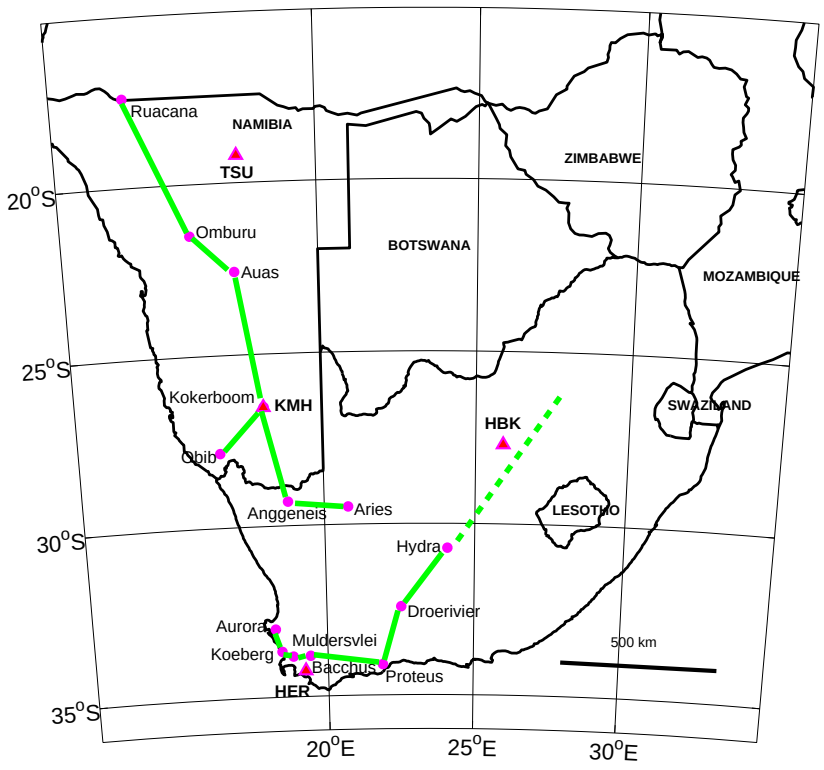

Figure 3.9: Map showing part of the Namibian and South African 400 kV transmission line network. The South African magnetic observatories are shown on the map.

3.4.2 Field work

The images in Figures 3.10 to 3.14 demonstrate the steps taken during the deployment of the magnetometers at the measurement site in South Africa. The images outline several aspects to consider when deploying magnetometers in the field to protect the instruments and also ensure accuracy of the recorded data. Two sites were excavated at the same time. Images that best represent the described step were selected from either of the two sites. The list below highlights some materials that are needed for the deployment process.

1. Digging tools.
2. A wooden box (painted with water proof paint inside and outside) that can accommodate the assembled instruments and water containers for temperature regulation.
3. Durable plastic sheet, large enough to wrap the designed box.
4. Leveling instrument to make sure the magnetometer is not tilted during deployment, as that would add to misalignment.
5. Extra protection such as spikes or insect guard, to guard against animals digging out the instruments.

6. Multimeter to measure the battery voltage before closing up.

7. A GPS unit to record the location of the box so that it can be easily accessed later.

(a) View of the closest 400 kV line pylon.

(b) Identified site before excavation.

Figure 3.10: Stage 1: A view of the identified suitable sites.

(a) The start of site excavation.

(b) The end of site excavation.

Figure 3.11: Stage 2: Excavation of the selected sites for system deployment.

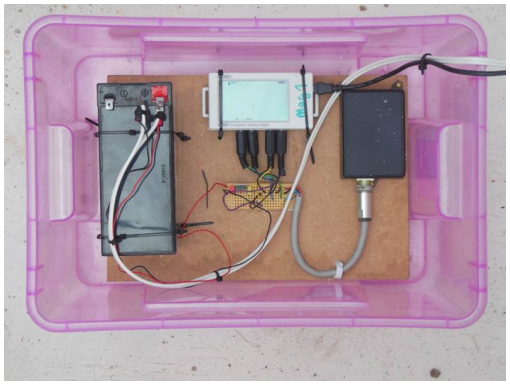

(a) View of the assembled equipment in a plastic container.

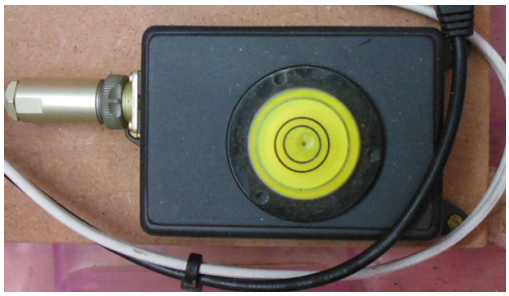

(b) Bubble level used to check if the magnetometer is horizontally aligned.

(c) Launch the HOBO data logger using a USB cable from a laptop pc.

(d) Record readings before closing.

Figure 3.12: Stage 3: Instrument assembly and launch of data logger.

(a) Water container for temperature regulation.

(b) Extra container close to the surface to protect the USB cable against moisture and sand particles and allow easy access for data download.

Figure 3.13: Stage 4: Temperature and moisture control.

(a) Closed box with protection including spikes and insect guard.

(b) Plastic protection to cover the top.

(c) Cover with the soil.

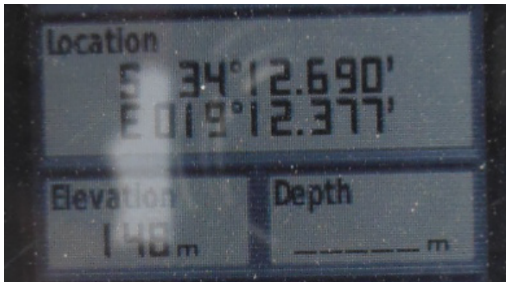

(d) GPS coordinates of the site.

Figure 3.14: Stage 5: Closing up and safe-guarding the instruments.

3.4.3 System improvement

The output of the system is the recorded x, y and z components of the magnetic field. Some additional items in the system may improve its efficiency. The temperature variation of the magnetometer is important in the magnetic field recordings, as it may affect the response of the magnetometer. The limiting factor in this system was the number of ports on the logger. Hence, a temperature logging system is needed. Regular wireless data transfer is also preferred so that any problems in the logging system can be identified timeously. A voltage monitoring system is also essential for maintaining a reliable power supply. When new electronic devices are added in the measurement system, the level of interference they may have on the magnetometer must be considered and catered for in the calibration matrix.

3.5 Conclusion

This chapter presented the technical aspects of the DMM and the algorithm recommended for inferring GIC in a power line. From the Finland (Mäkinen, 1993) and Brazil (Trivedi *et al.*, 2007) measurements, the GIC could be inferred from the three measured magnetic field magnetic field components and scaling factors were derived to calculate the GIC. In the current study, the GIC is inferred from the magnetic field component perpendicular to the power line and this is achieved through the alignment of the magnetometer axes with the power line. The requirements of the deployed system were outlined. Furthermore, the procedure followed in the deployment of the magnetometers was illustrated with the aid of pictures taken during the process to enhance clarity of the discussed deployment method. Some suggestions were given for the future improvement of the DMM system and data access.

CHAPTER 4: RESULTS OF GIC MEASUREMENTS USING THE DIFFERENTIAL MAGNETOMETER METHOD

4.1 Introduction

This chapter presents the results obtained from the measurement of GIC using the differential magnetometer method (DMM). The magnetic field measured under the power line and that measured at the reference points are compared. In the discussion of the results, the applicability of this technique in the Southern African region is evaluated by comparing GIC estimated using the DMM with the GIC measured at the neutral-to-ground terminal of the power transformers using Hall-effect transducers and GIC estimated using other algorithms.

4.2 Measurements in the Namibian network

The measurements done in Namibia were opportunistic and took advantage of magneto-telluric (MT) station installations that were taking place during that period. Due to the high costs that would have been incurred if the identified site were to be visited frequently, data were recorded for a period of one week for further processing and analysis. The Namibian power network was considered ideal for the DMM evaluation because of its simplicity. The selected site had only a small number of network interconnections compared to the South African power network. The measurements were done along the 400 kV power line running from the Kokerboom substation (26.54°S, 18.12°E) to the Obib (27.83°S, 16.63°E) substation from 6 July 2013 to 12 July 2013. The 400 kV power line terminates at the Obib substation where there was a GIC monitoring system on the neutral-to-ground terminal of the power transformer at the time of the measurements.

The Hermanus K-index (K(HER)) was used to evaluate the intensity of the geomagnetic disturbance. In terms of geomagnetic activity, the measurement period under discussion could be regarded as mostly quiet days except for 6 July when K(HER) = 5 occurred and 11 July 2013 when some geomagnetic activity of peak intensity K(HER) = 4 occurred (minor storm which may result in small fluctuation in a power system (Campbell, 2001)). Figure 4.1 shows the K(HER) during the measurement days.

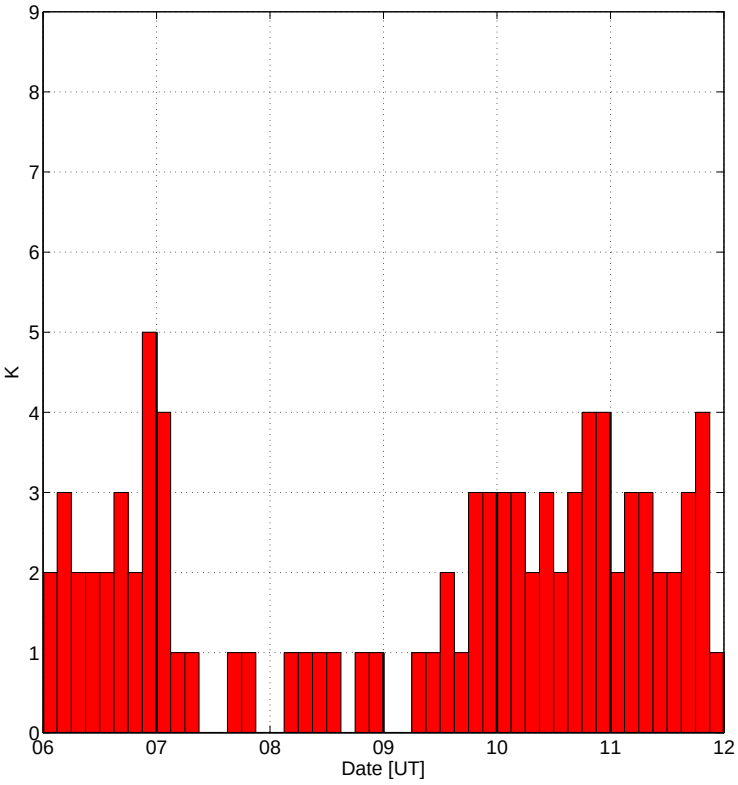

Figure 4.1: The K-index (K(HER)) for 6-12 July 2013 during DMM measurement in Namibia.

4.2.1 Measurement setup

For the magnetic field measurements under the power line, the magnetometer of one of the LEMI-417 MT unit was used. The full MT setup (magnetic sensor and the electric field electrodes) was mounted 200 m West of the power line. The x-axes of both magnetic sensors were aligned such that they are parallel to the direction of the power line, which was approximately aligned with Geographic North. The y-axes of the magnetic sensors were, therefore, aligned perpendicular to the power line, i.e. approximately Geographic East. Such an alignment allows the magnetic sensor to measure the contribution of the power line current effectively with one axis of the magnetometer (the one perpendicular to the power lines; in this case the y-axis). Figure 4.2 shows the instrument setup as described. The location where the MT was mounted, is referred to as the Obib-remote and the other magnetometer location under the power line is referred to as Obib-line.

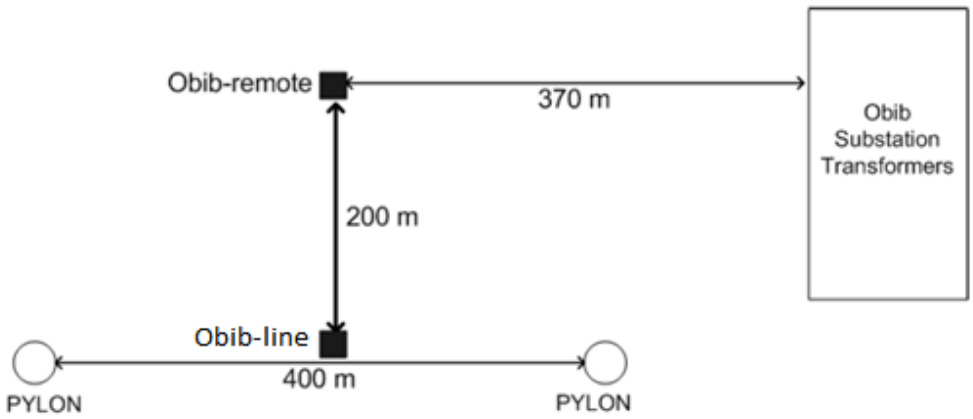

Figure 4.2: An overview of the setup of the magnetometers at the Obib measurement site. Obib-remote is the location of the MT station were both magnetic and electric fields were measured. Obib-ine is the location of the magnetometer under the power line.

4.2.2 Measurement results

For further comparison of the measured magnetic field variations, magnetometer data from a nearby INTERMAGNET Magnetic Observatory can be used as reference. Unfortunately, during this measurement period, the magnetometer at Keetmanshoop (KMH), which is nearest to the Obib measurement site, was down for the period 8 July 2013 to 20 July 2013. Due to the failure of the KMH magnetometer, Tsumeb (TSU) data were considered for further data analysis. The distance from measurement site (Obib-MT) to KMH is $\approx$ 205 km while TSU is $\approx$ 970 km away.

A comparison of the daily magnetic field variations at KMH and TSU was done for two consecutive quiet days, K(HER) $\leq$ 1. This was done to demonstrate that the daily variation of these two stations under geomagnetically quiet conditions are similar, hence justifying the use of TSU as the reference station for GIC estimation in cases where KMH is down or the other way round. The selected quiet days were 3 July 2013 and 4 July 2013. Figure 4.3 shows the magnetic field variations for TSU and KMH on the selected quiet days.

Figures 4.4 and 4.5 show the magnetic field measured under the power line and 200 m away from the power line, respectively. The magnetic variations were compared to TSU data in Figure 4.6. INTERMAGNET data were available in 1 minute intervals. The Obib data were available at 1 second intervals and averaged over 1 minute intervals for analysis purposes.

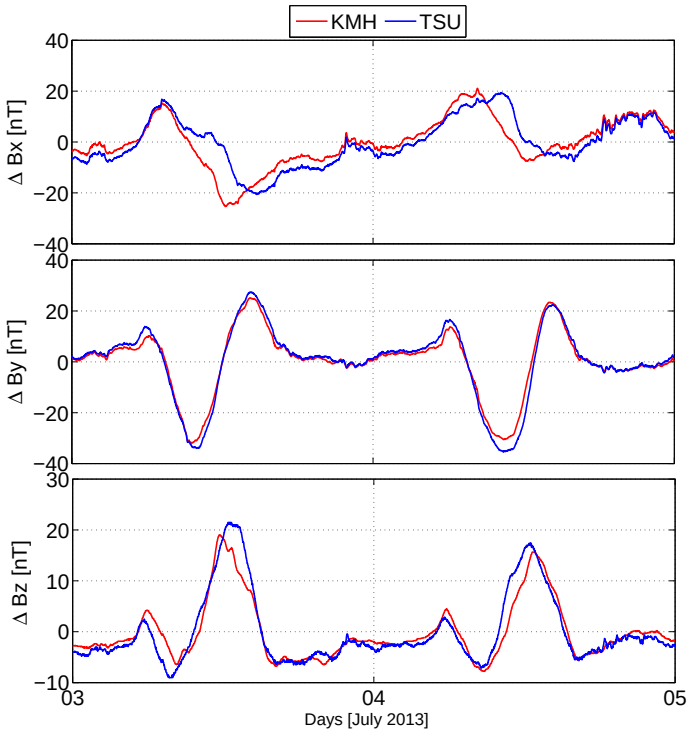

Figure 4.3: The magnetic field variations for Tsumeb (TSU) and Keetmanshoop (KMH) on typical quiet days.

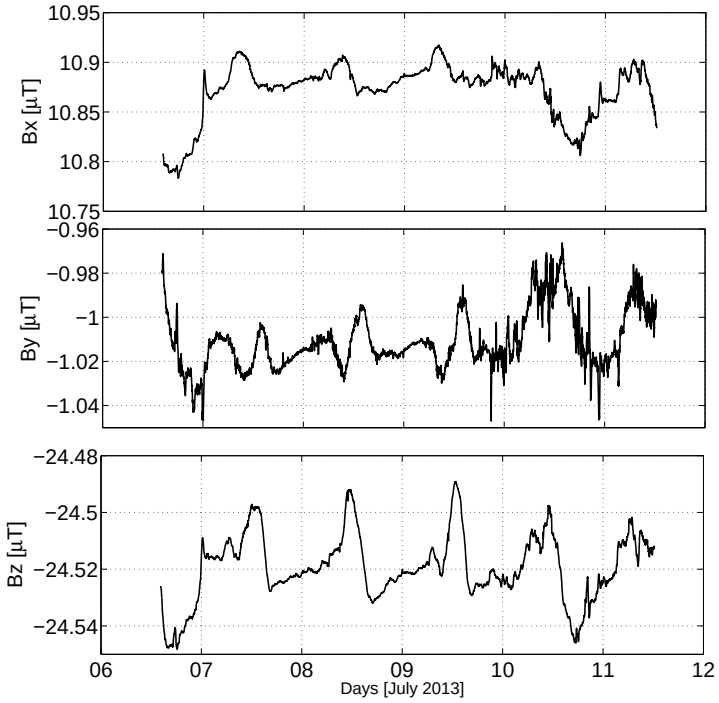

Figure 4.4: The magnetic field measured under the power line at Obib-line.

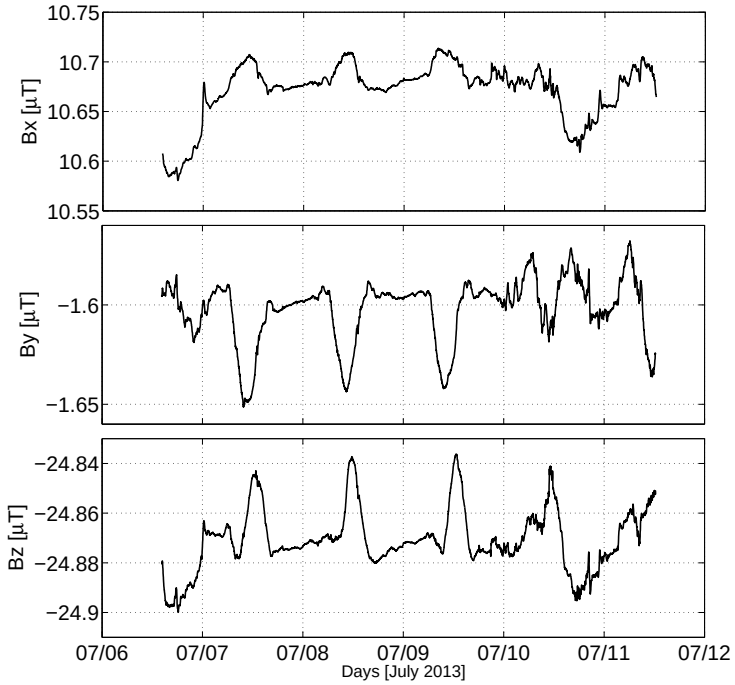

Figure 4.5: The magnetic field measured 200 m from the power line at Obib-remote.

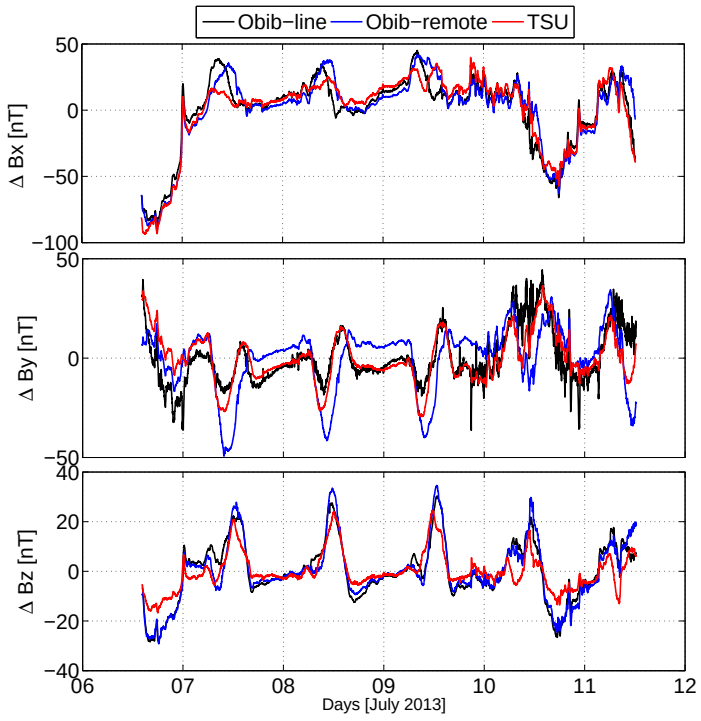

Figure 4.6: The magnetic field variation for the three measurement sites, under the power line (Obib-line), 200 m away from the power line (Obib-remote) and at Tsumeb (TSU).

4.2.3 GIC estimation

To estimate the magnitude of GIC in the power line using the DMM, equation 4.1 is used.

$$I_{GIC} = \frac{2\pi r}{\mu_0} B_{\perp} \tag{4.1}$$

where $B_{\perp}$ is the component of the magnetic field perpendicular to the line, which is assumed to be due to the GIC flowing in the power line. Due to the magnetic sensor alignment, $B_{\perp}$ corresponds to the difference between the B_y components of the measured magnetic field under the power line and the field used as reference. Figures 4.7 and 4.8 show the difference between the magnetic field measured under the power line and the reference magnetic field. The magnetic field data used for reference were the magnetic field measured 200 m away from the power line (at Obib-remote) and at TSU.

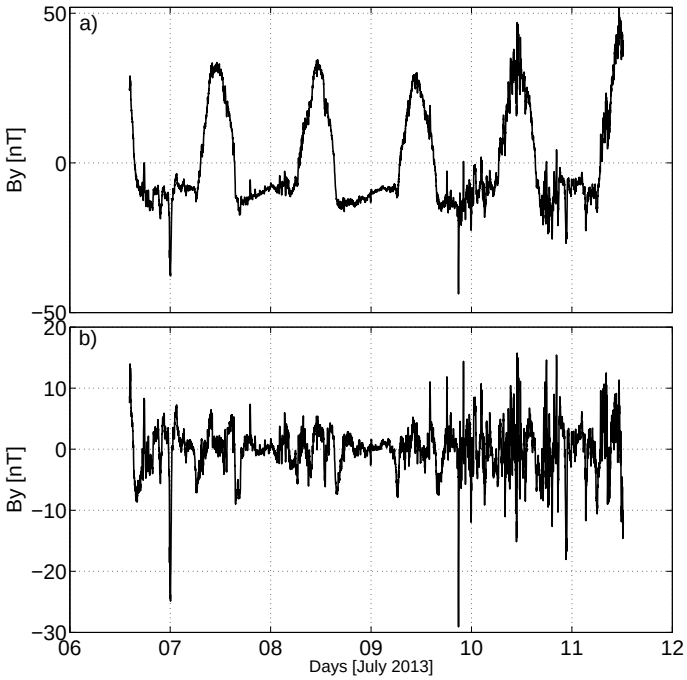

Figure 4.7: The perpendicular magnetic field component calculated using the magnetic field measurements 200 m away from the power line as reference. a) The magnetic field before removing the diurnal variation. b) The magnetic field after removing the diurnal variation by subtracting the average taken over the two quietest days i.e. 8 and 9 July 2013.

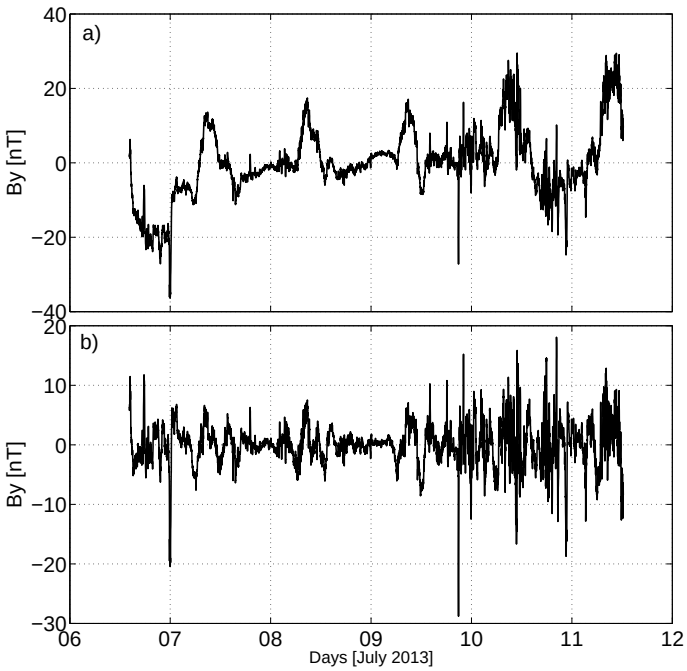

Figure 4.8: The perpendicular magnetic field component calculated using the magnetic field measured at Tsumeb as reference. a) The magnetic field before removing the diurnal variation. b) The magnetic field after removing the diurnal variation by subtracting the average taken over the two quietest days i.e. 8 and 9 July 2013.

Unfortunately, no reliable GIC data were available from the Obib GIC monitoring system for this particular period due to technical problems. GIC estimated using the DMM was, however, compared with GIC calculated using two different approaches. The first approach used equation 2.45 to calculate GIC using the electric field measured at the reference point (Obib-remote) by the MT station electrodes.

The a and b network parameters for the Obib substation used in the GIC calculation are a= 25.90 Akm/V, b= 34.90 Akm/V, which were obtained using the LP method discussed in section 2.6. Figure 4.9 shows the measured electric field.

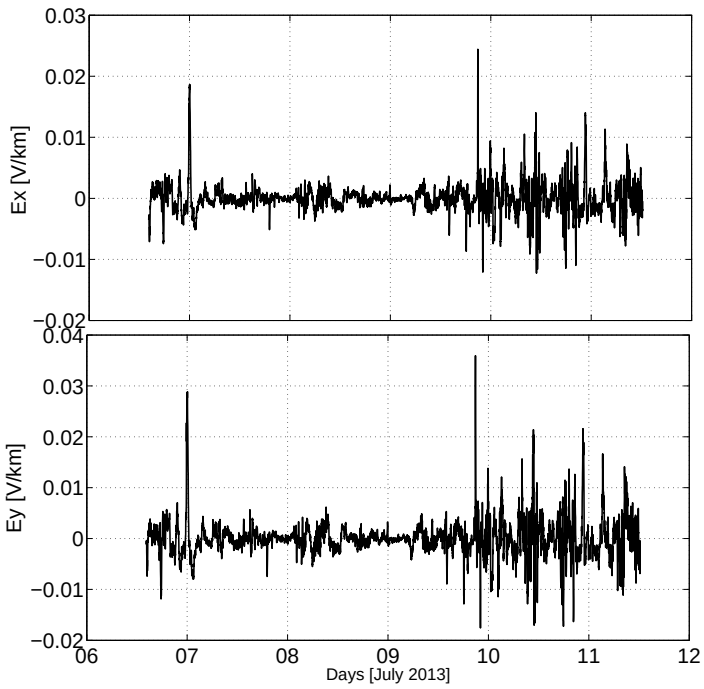

Figure 4.9: The electric field measured by the MT station at the Obib-remote site, 200 m away from the power line.

The second approach was to use the Nodal Admittance Matrix method (NAM) to calculate GIC for this particular period. Equation 4.2 was applied to calculate the GIC through the Obib substation.

$$I_{GIC} = [\mathbf{y}_0\mathbf{y}_0\mathbf{y}_{0\mathbf{y}_0][\mathbf{Y}]^{-1}[\mathbf{H}](4.2)$$

where $[I_{GIC}]$ is the nodal GIC, $[y_0]$ is the nodal admittance row matrix, $[\mathbf{Y}]$ is the network admittance matrix, $[\mathbf{H}]$ is the matrix of Norton's currents. Boteler (2014) and Trichtchenko *et al.* (2007) discuss the computation of the Norton's currents.

The TSU magnetic field was used for computing the horizontal components of the electric field used for the GIC computation with the NAM method. The calculation of the electric field was done using the inverse Fourier transform method following the procedure illustrated in Figure 2.17. A homogenous Earth model with conductivity 45 mS/m was used. This conductivity value was derived from a best fit of the estimated electric field for a homogeneous Earth approximation, and the measured electric field from the MT measurements of that period. Figure 4.10 shows the calculated electric field used as input in the NAM procedure. Figure 4.11 shows how the GIC estimated with the three different methods compared.

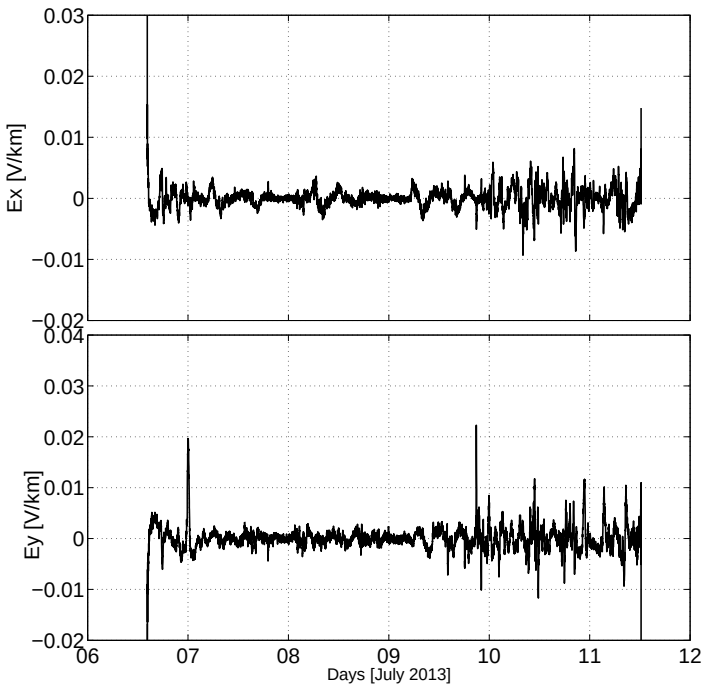

Figure 4.10: The electric field calculated applying to the inverse Fourier transform method using the magnetic field measured at Tsumeb. The peaks at the start and end of the inversion are artifacts of the inversion method.

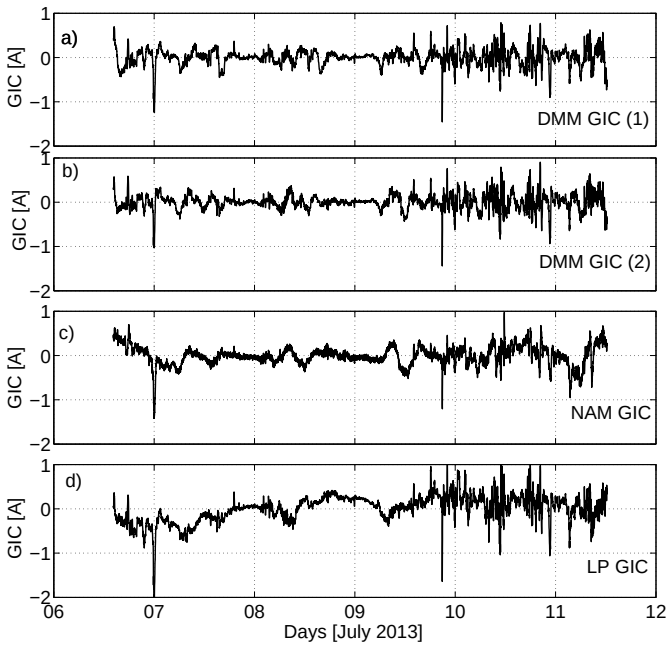

Figure 4.11: Comparison of the four estimates of GIC. a) DMM GIC(1) is the GIC calculated with difference between the magnetic field measured at Obib-line and Obib-remote. b) DMM GIC(2) is the GIC calculated with difference between the magnetic field measured at Obib-line and TSU. c) NAM is the GIC calculated using the Nodal Admittance Matrix method. d) LP GIC was calculated from the measured electric field using equation 2.45.

4.2.4 Discussion of measurements

4.2.4.1 Magnetic field

The y component of the magnetic variations measured under the power line had the largest variation with respect to the remote site, was more noisy and exhibited larger spikes than the other components. The magnetic field measurement results support the expected outcome of the magnetometer alignment. The magnetometer axes were positioned such that only the y-axes will measure the magnetic field due to the GIC in the power line. The cause of these spikes may be related to network operation i.e. the switching on and off of some systems linked with the network which feeds the Roshpinah mine. During daily operations, power utilities are subjected to voltage transients. These are short-duration increases or decreases in voltages. The voltages have a direct influence on the current flowing in the power lines. The observation on the recorded magnetic field might be an influence of the voltage transients (Russell, 2000). The main sources are utility power switching, and the switching on and off of high power demanding equipment such as industrial motors, which are typical of mining operations.

The x component and the z component of the field measured under the power line are less noisy. This was anticipated as any GIC in the power line is not expected to have any influence on these axes due to the alignment of the magnetometer.

4.2.4.2 Statistical analysis

To evaluate the correlation between the GIC estimated using the three different techniques, the correlation coefficient (R) was computed using equation 4.3

$$R = \frac{n\sum xy - (\sum x)(\sum y)}{\sqrt{n(\sum x^2) - (\sum x)^2}\sqrt{n(\sum y^2) - (\sum y)^2}}, \tag{4.3}$$

where n is the number of data points.

The value of R for the DMM and the NAM method estimations of the GIC is 61 %. The value of R for the DMM GIC and the GIC estimated from the use of measured electric field is 71 %. The correlations confirm the visual observation that the results of the three methods have some common features. The maximum GIC estimated for the three techniques are: 1.6 A for the DMM, 1.2 A for the NAM method and 1.9 A when using the MT measured electric field. The measured electric field may be affected by local geological conditions.

4.2.4.3 General remark

Both reference magnetic field values used in the GIC computation may have been compromised. The TSU station is very far (970 km) from the DMM measurement location. This may have compromised the spatial uniformity of the background magnetic field (Ngwira *et al.*, 2009). The MT was located close (370 m) to the Obib substation as well. Magnetic interference from the substation equipment may have influenced the measured magnetic field recordings (Uchida *et al.*, 2005). For the Obib substation, we therefore recommend the use of KMH (205 km away) as reference. However, the measurements indicate that the sensitivity of the magnetometers used were sufficient to record the smaller magnetic variations and are therefore suitable to for DMM observations.

Due to the limited amount of data, the noisiness of the data and the fact that there was no GIC measured at the substation, the Namibia measurements provide only limited confirmation of the DMM method.

4.3 Measurements in the South African network

A suitable measurement site was identified on a farm near Botriver in the Overbeg, Western Cape. The measurements were done under the 400 kV line running from the Muldersvlei substation (33.82°S, 18.81°E) to the Bacchus substation (33.81°S, 19.40°E). Two sets of the LEMI-011 magnetometers discussed in section 3.3.2.2 were used. The site was selected due to its accessibility and the security of the measurement system. The period of measurement discussed is from 17 to 21 March 2015. This period included one of the few periods of K(HER) = 7 geomagnetic disturbances recorded during solar cycle 24. The K(HER) for the measurement period is shown in Figure 4.12. The period included storms categorised as minor (K=5), moderate (K=6) and strong (K=7) according to the NOAA space weather scale (Campbell, 2001). The measurements at Botriver were sampled at 10 seconds and averaged over 1 minute intervals for further analysis.

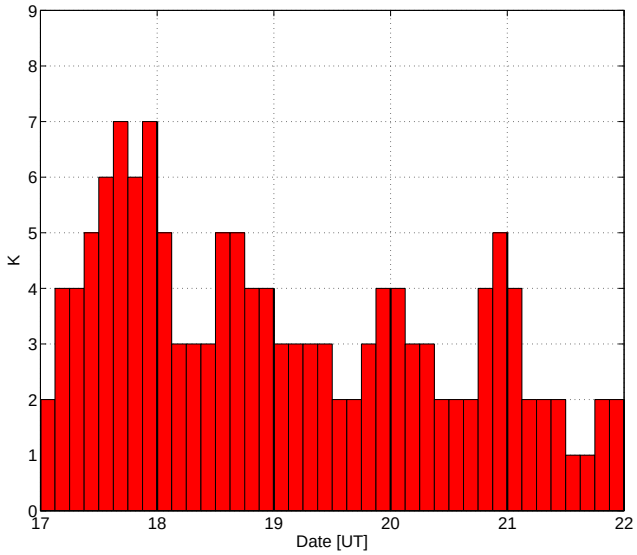

Figure 4.12: The Hermanus K-index for 17 to 21 March 2015.

4.3.1 Measurement setup

The annotated map in Figure 4.13 shows a view of the measurement area. Site A is the measurement point under the power lines while site B is 70 m from site A in a direction perpendicular to the power line. Site B was about halfway between the 400 kV power line and an adjacent 50 kV power line, a location chosen to give the least contribution from GIC in either of the power lines. To standardise the magnetometer alignment the x-axes of both magnetometers were aligned with reference to Magnetic North by rotating them until the magnetic field recorded on the y-axes was approximately zero.

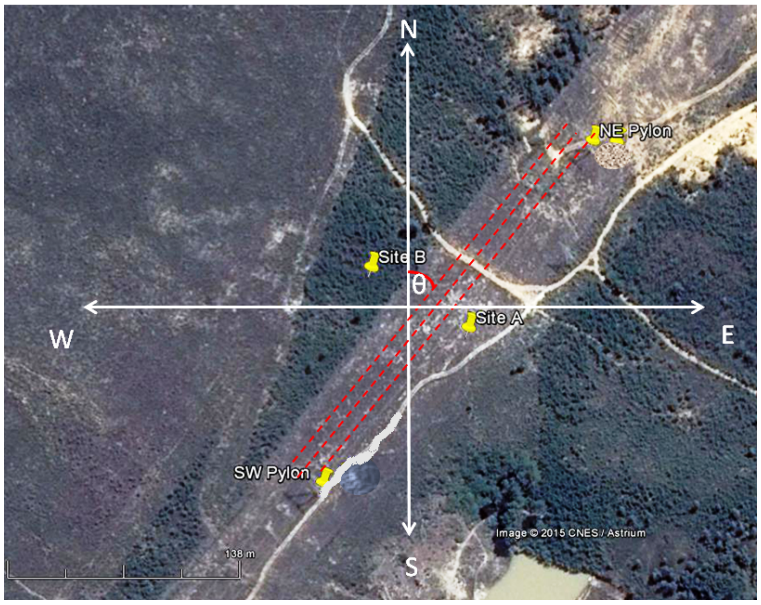

Figure 4.13: An annotated Google map image of the measurement site near Botriver which is situated ≈ 30 km away from the magnetic observatory in Hermanus. The red lines are drawn along the 400 kV power lines.

The component of the magnetic field required to estimate the GIC in the line should be the magnetic field component perpendicular to the line direction. This implies that the field measured at sites A and B need to be rotated through the power line bearing and the local declination angle. The power line bearing is the angle between the power line and Geographic North measured in a clockwise direction. The bearing θ was estimated from the map and taken as 38°. The declination angle is the angle between Magnetic North and Geographic North. The declination angle used for the measurement was assumed to be the same as that in Hermanus, namely -25.54° (NRF/HMO, 2009).

Figure 4.14 illustrates the concept of finding the magnetic field components in a rotated coordinate system. If the Cartesian coordinate system is used where the x-axis points to the Geographic North and the y-axis points towards the Geographic East, and the measured magnetic field represented by vector **F**, transformation of the components of the field to the $x'y'$ coordinate system implies that

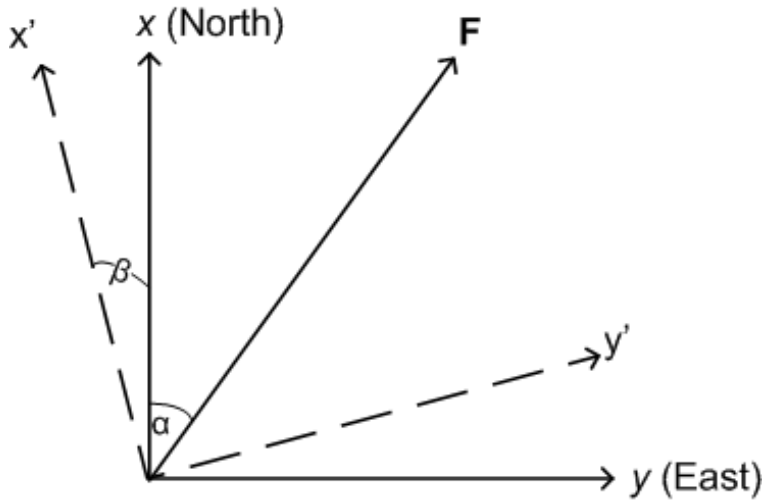

Figure 4.14: Coordinate transformation to determine the magnetic field component perpendicular to the power line. Both α and β are here assumed to be positive angles.

$$B_{x'} = \mathbf{F}\cos(\alpha+\beta) = \mathbf{F}\cos\alpha\cos\beta - \mathbf{F}\sin\alpha\sin\beta \tag{4.4}$$

$$B_{x'} = B_x\cos\beta - B_y\sin\beta \tag{4.5}$$

$$B_{y'} = \mathbf{F}\sin(\alpha+\beta) = \mathbf{F}\sin\alpha\cos\beta + \mathbf{F}\cos\alpha\sin\beta \tag{4.6}$$

$$B_{y'} = B_y\cos\beta - B_x\sin\beta \tag{4.7}$$

Hence, the transformation is achieved through a transformation matrix in the following manner:

$$\begin{bmatrix} B_{x'} \\ B_{y'} \end{bmatrix} = \begin{bmatrix} \cos\beta & -\sin\beta \\ \sin\beta & \cos\beta \end{bmatrix} \begin{bmatrix} B_x \\ B_y \end{bmatrix} \tag{4.8}$$

where $\begin{bmatrix} \cos\beta & -\sin\beta \\ \sin\beta & \cos\beta \end{bmatrix}$ is the coordinate rotation matrix.

In the present situation we expressed the magnetic field at the power line with reference to Magnetic North by B_x, B_y, with reference to the Geographic North by $B_{x'}, B_{y'}$ and with reference with the power line by $B_{x''}, B_{y''}$. For declination angle $-\theta_1$ and the power line bearing $-\theta_2$, the coordinate rotation is achieved through the following matrices

$$\begin{bmatrix} B_x \\ B_y \end{bmatrix} = \begin{bmatrix} \cos\theta_1 & \sin\theta_1 \\ -\sin\theta_1 & \cos\theta_1 \end{bmatrix} \begin{bmatrix} B_{x'} \\ B_{y'} \end{bmatrix} \tag{4.9}$$

$$\begin{bmatrix} B_{x''} \\ B_{y''} \end{bmatrix} = \begin{bmatrix} \cos\theta_2 & \sin\theta_2 \\ -\sin\theta_2 & \cos\theta_2 \end{bmatrix} \begin{bmatrix} B_x \\ B_y \end{bmatrix} \tag{4.10}$$

4.3.2 Measurement results

The magnetic fields measured at Site A (Bot-line) and Site B (Bot-remote) are therefore compared to the magnetic field measured at HER. Figures 4.15 and 4.16 show the measured components of the field under the power line in the geomagnetic and power line coordinate system, respectively. Figures 4.17 and 4.18 show the magnetic field 70 m away from the power line in the same coordinate systems. Figure 4.20 compares the magnetic field variation in the geographic coordinate system at the three sites and Figure 4.21 shows the difference between the magnetic field measured under the power line, the field measured 70 m away and at HER (shown in Figure 4.19) in the power line coordinate system.

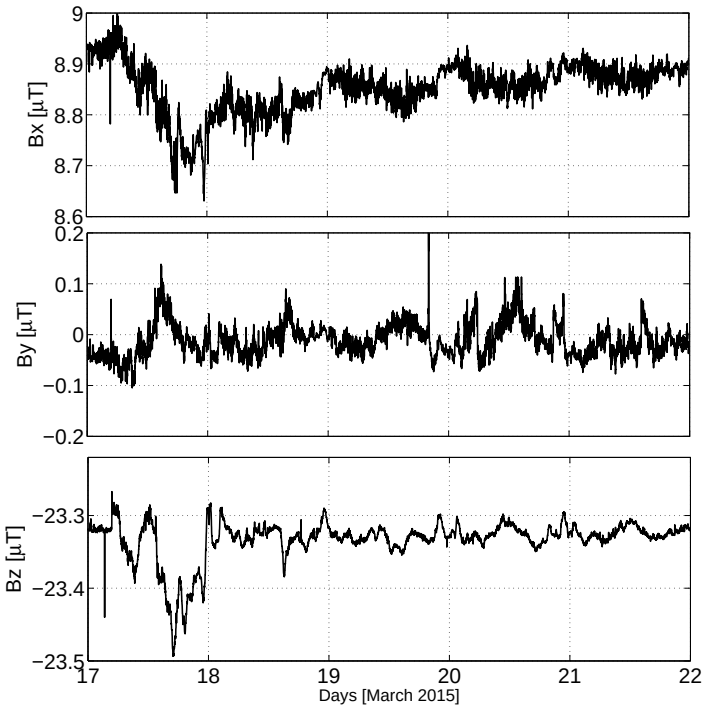

Figure 4.15: Magnetic field measured under the power line at site A (Bot-line).

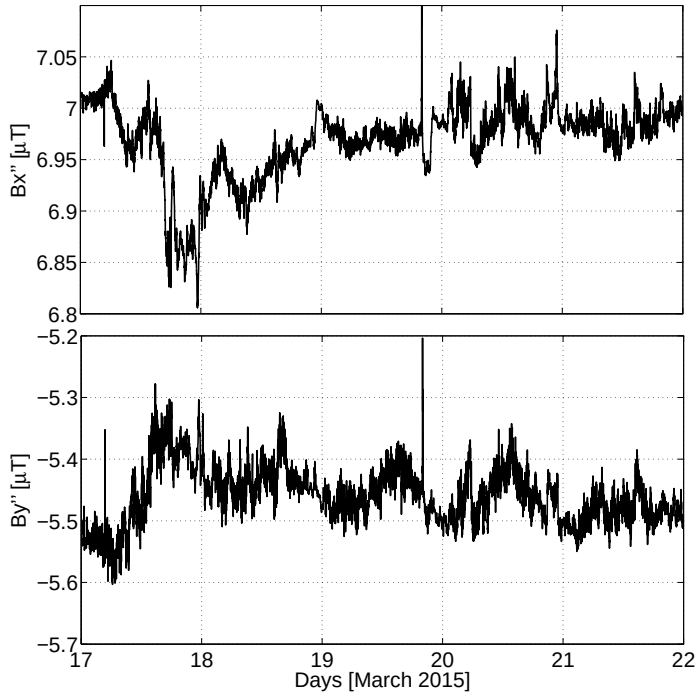

Figure 4.16: Horizontal components of the magnetic field measured under the power line at site A rotated through the declination angle and the power line bearing.

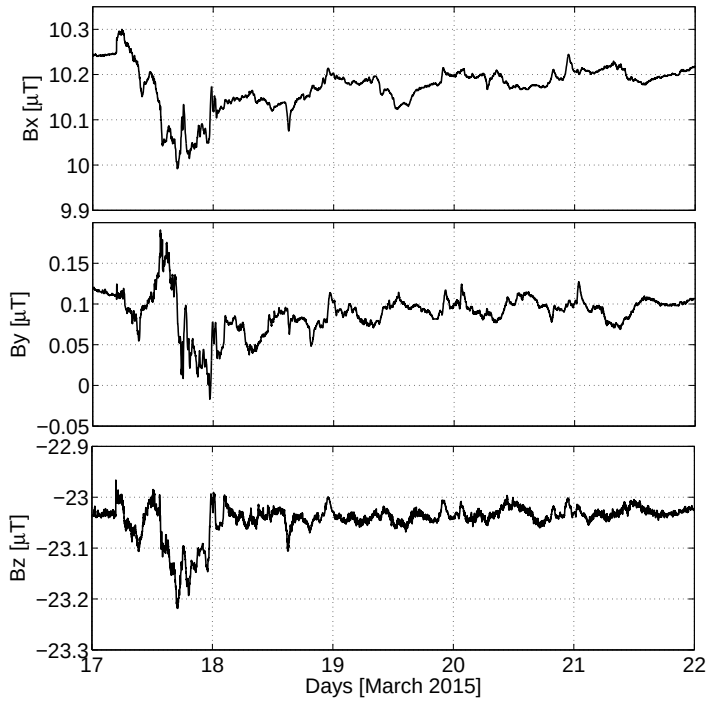

Figure 4.17: Magnetic field measured at site B (Bot-remote), 70 m away from the power line.

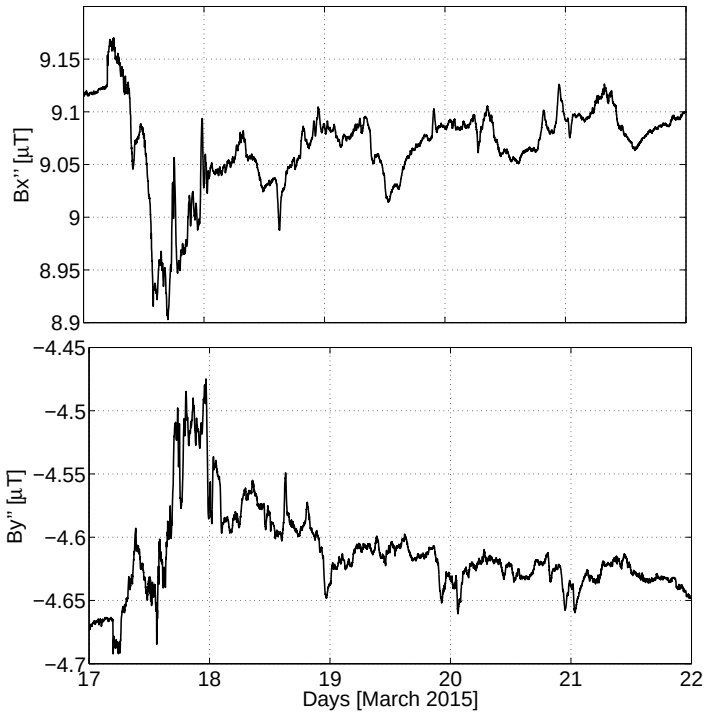

Figure 4.18: Horizontal components of the magnetic field measured under the power line at site A in a coordinate system rotated through the declination angle and the power line bearing.

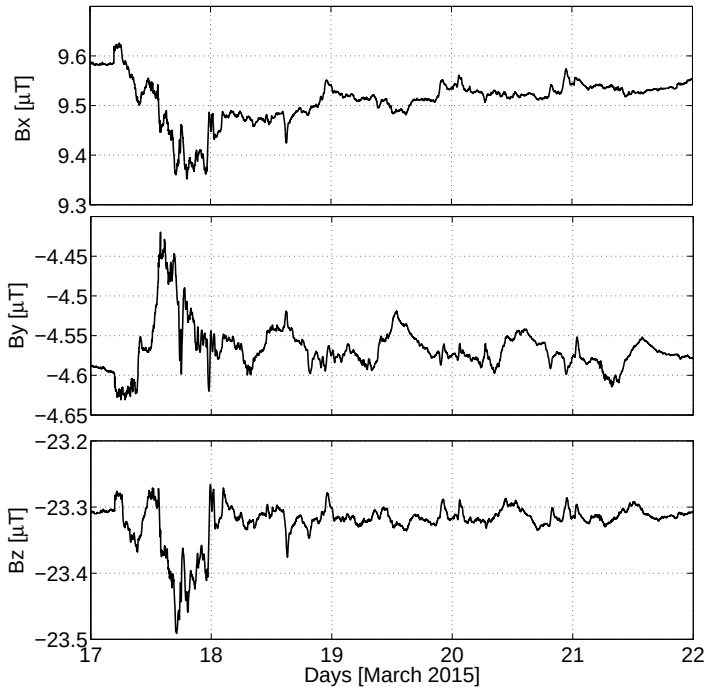

Figure 4.19: Magnetic field measured at Hermanus Magnetic Observatory.

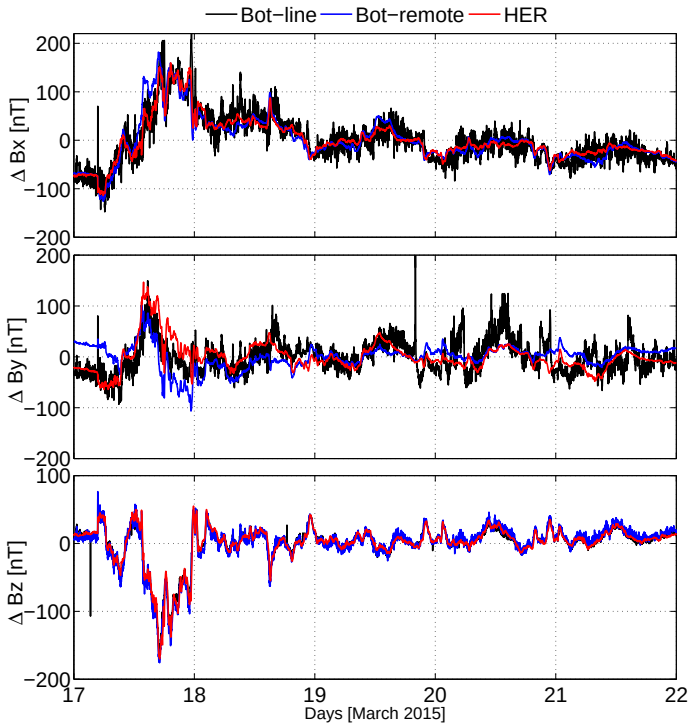

Figure 4.20: Magnetic field variation for the three measurement sites, Bot-line, Bot-remote and HER in a coordinate system aligned with geographic North. ΔB_z, Bot-line and Bot-remote coincide since the GIC does not create any B_z component.

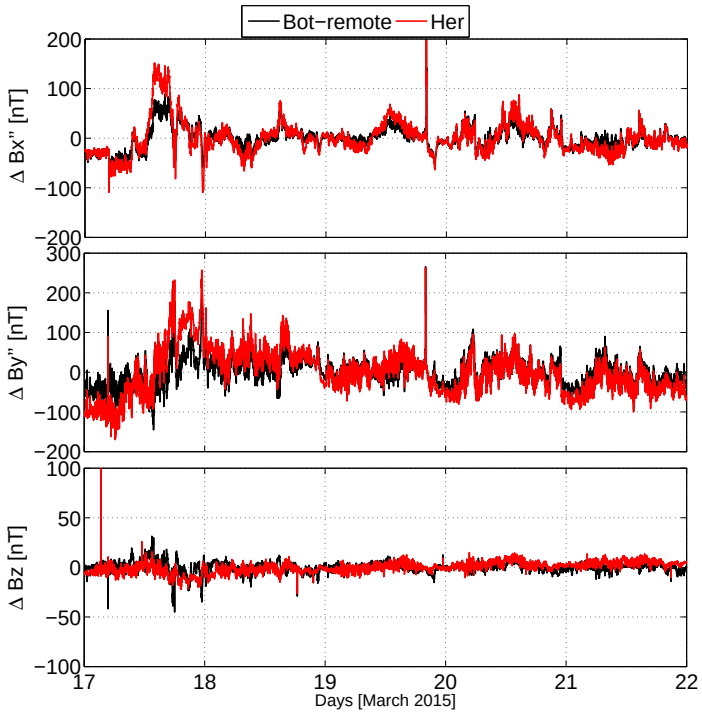

Figure 4.21: Magnetic field variation measured under the power line and at the reference sites. "Bot-remote" is the difference between rotated magnetic field measured under the power line and the rotated magnetic field measured 70 m away. "Her" is the difference between rotated magnetic field measured under the power line and magnetic field measured at Hermanus Magnetic Observatory.

4.4 GIC estimation

The GIC estimated using the DMM method are compared with GIC measured using the Hall-effect sensor on the neutral-to-ground connection of one transformer at the Bacchus substation. The GIC monitoring at Bacchus substation system records the minimum GIC value per 5 minute interval, the maximum GIC value per 5 minute interval, as well as the 5 minute average. From the DMM method, the GIC was calculated using two references, the measurements at 70 m away (Bot-remote) as well as HER. Figures 4.22 and 4.23 show the comparison of the GIC as follows:

a) The estimated and measured minimum GIC within 5 minute intervals.
b) The estimated and measured average GIC within 5 minute intervals.
c) The estimated and measured maximum GIC within 5 minute intervals.

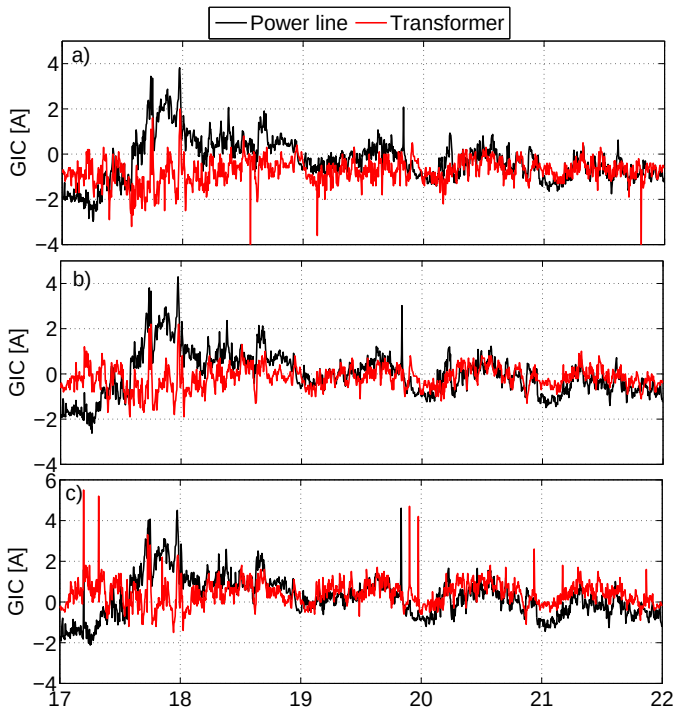

Figure 4.22: The estimated and measured GIC. "Power line" is the estimated GIC using the DMM and "Transformer" is the GIC measured at the transformer neutrals. Reference magnetic field data used for DMM were measured at Bot-remote.

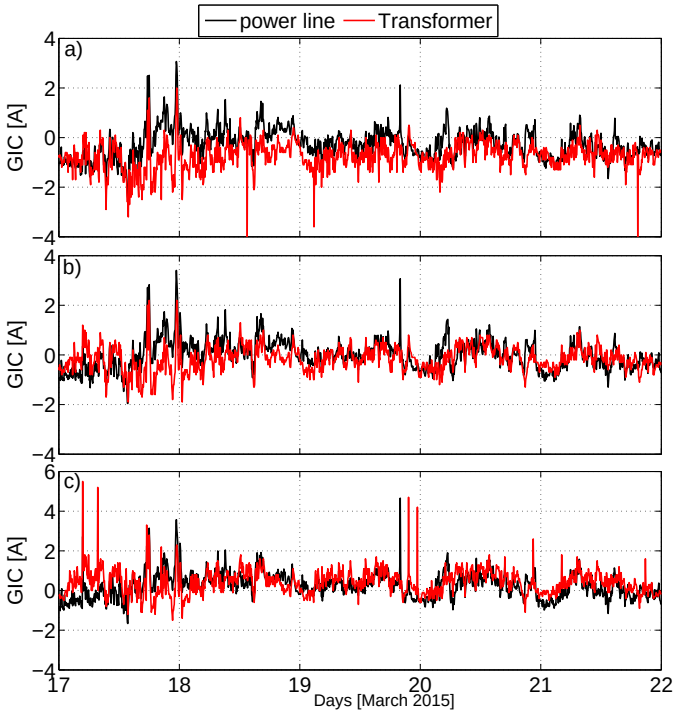

Figure 4.23: The estimated and measured GIC. "Power line" is the estimated GIC using the DMM and "Transformer" is the GIC measured at the transformer neutral. Reference magnetic field data used for DMM were measured at Hermanus Magnetic Observatory

4.5 Discussion of the Botriver results

4.5.1 The measured magnetic field

The difference between the components of the magnetic field measured under the power line (Bot-line in Figure 4.20) and the corresponding components at the reference location (Bot-remote) are larger in the case of the x and y components than in the case of the z component, irrespective of whether the reference field is measured 70 m away from the power line, or at Hermanus (about 30 km away from the power line) as shown in Figure 4.21 and Table 4.1

Table 4.1 gives RMS values of the differences between the magnetic field components under the power line and the corresponding components of the reference field.

Table 4.1: RMS values of the differences between the magnetic field components under the power line, and the corresponding components of the reference field.

Reference	Component		
	x (nT)	y (nT)	z (nT)
Hermanus	22.6	36.2	5.5
70 m from line	33.6	57.1	5.5

The z component of the magnetic field under the power line is expected to be the closest to the reference field, since the magnetic field due to the GIC in the centre phase of the power line is parallel to the ground and would thus not cause any difference from the background z component. The small variation in the z component is attributed to the z component of the magnetic field due to the GIC in the outer two phases of the three-phase line, since the magnetometer under the power line was located directly below the centre conductor of the three-phase line. The observation that the differences in the x and y components of the magnetic field were significantly larger than the difference in the z component is taken as evidence that the variation in the horizontal components of the magnetic field are due to the GIC in the line.

The observation that the noise levels on all three components of the magnetic field measured 70 m away from the power line are about the same (See Figure 4.17), and that all components of the magnetic field at 70 m away from the power line are about the same as measured in Hermanus, is taken as evidence that the influence of GIC flowing in the power line is minimal at 70 m away from the power line and also that there is spatial uniformity of the magnetic field over the distance between 70 m away from the power line and Hermanus. Thus, it can be assumed that the low frequency magnetic field under the power line would be the same as at 70 m away from the power line if there were no GIC in the power line.

The slightly larger noise level in the z component of the magnetic field at 70 m away from the power line, than the noise level in the x and y components at this location, and the fact that the noise level in the z component of the magnetic field at 70 m away from the power line is slightly larger than in the z component of the magnetic field in Hermanus, may be attributed to some effect of the

GIC in the power line at 70 m away from the power line, which is expected to be more dominant in the z-component than in the y-component at this distance.

4.5.2 Statistical analysis

The statistical analysis of the relationship between the measured GIC and the GIC estimated from the DMM is presented in terms of the root-mean-square-error (RMSE) as well as the correlation coefficient (R). The RMSE is calculated using

$$RMSE = \sqrt{\frac{\sum_{i=1}^{n}(X_{obs,i} - X_{model,i})^2}{n}} \tag{4.11}$$

where $X_{obs,i}$ is the i^{th} observation, $X_{model,i}$ is the corresponding value of the GIC estimated from the DMM measurements and n is the number of observations.

Tables 4.2, 4.3 and 4.4 show the statistical analysis of the data shown in Figures 4.22 and 4.23, namely the correlation coefficients and the RMSE between the minimum, average and maximum GIC measured in each 5 minute interval in the ground-to-neutral connection at the Bacchus power transformer and the corresponding minimum, average and maximum GIC in each 5 minute interval derived from the DMM measurements.

Table 4.2: Statistical analysis of the minimum GIC measured at the transformer neutrals with GIC_1 and GIC_2.

	R %	RMSE [A]
GIC_1	20	1.1
GIC_2	50	0.7

Table 4.3: Statistical analysis of the average GIC measured at the transformer neutrals with GIC_1 and GIC_2.

	R %	RMSE [A]
GIC_1	23	1.0
GIC_2	52	0.6

Table 4.4: Statistical analysis of the maximum GIC measured at the transformer neutrals with GIC_1 and GIC_2.

	R %	RMSE [A]
GIC_1	26	1.1
GIC_2	49	0.7

The DMM data were measured at 10 second intervals while the measured GIC was recorded at 5 minute intervals. The difference in the sampling rate of the measured magnetic field and GIC led to significant averaging, which could have contributed to the lower calculated correlation coefficients. The difference between the GIC in the power line as estimated from the measurements and the GIC recorded at Bacchus transformer, can be due to the fact that there are power lines leaving

the transformer at Bacchus at different angles. Hence, some, but not all GIC measured at Botriver will flow to the ground via the neutral connection at Bacchus. Better correlation coefficients and lower RMSE values are obtained when the HER magnetic field is used for reference, rather than Bot-remote. The reason for observation may be that the Botriver reference, which is 70 m away from the 400 kV power line, is too close to the power line, and hence, contain some influence of the GIC in the power line as pointed out above.

4.6 Conclusion

The results indicate that the GIC in a power line can be detected and estimated from the magnetic field variations in the proximity of high voltage power lines. This conclusion derives from the larger storm-related variation in the magnetic field perpendicular to the power line than in the vertical component which would not be affected by GIC in the power line. This attribute of the magnetic field under the power line is an indication that the application of the DMM on non-DC compensated power lines can provide an enhancement in the understanding of GIC in the power network.

CHAPTER 5: APPLICATION OF FINITE ELEMENT METHOD IN GIC MODELLING

5.1 Introduction

This chapter discusses the application of the finite element method (FEM), a rarely explored technique when it comes to GIC modelling. A FEM simulation package COMSOL Multiphysics [1], is chosen for the current study. In this study, FEM is used for the first time here to compute the induced geoelectric field using measured magnetic field data and a realistic ground conductivity profile.

5.2 Finite element method basics

FEM is a numerical technique applicable to solving partial differential equations (PDE) for boundary value problems associated with complex geometry. A boundary value problem is defined as "a mathematical problem in which one or more dependent variables must satisfy a differential equation everywhere within a known domain of independent variables, and satisfy specific conditions on the boundary of the domain" (Hutton, 2004). In engineering and mathematics, the complex geometry is often represented by a model. A model is a symbolic structure defined in the FEM simulation software to simulate and predict aspects of behaviour of a real system.

This method dates back to the 1950s where it was used in the aerospace industry and later in structural and solid mechanics. As years progressed, more discoveries about the method led to its application in problems involving heat transfer and fluid dynamics (Bathe, 1982). The capabilities of FEM to use variational methods, such as the Galerkin's method or the least square approach, made it possible to solve a wider range of problems.

5.2.1 The general finite element method process

Certain procedures are followed during the FEM process. The order of execution in different commercial software packages may vary. The paragraphs below explain these procedures.

1. *Model Definition*
   The problem is defined on the simulation platform in the correct dimensions (1D, 2D or 3D). The appropriate coordinate system is assigned, e.g. planar, cylindrical or spherical depending on the shape of the problem domain.

2. *Discretisation*
   Discretisation is the process whereby the complex geometry is subdivided into smaller components known as "elements". These elements are connected by nodes, such that there is no overlapping and no gaps between the adjacent elements. Figure 5.1 shows a general domain or field that can be defined and subdivided into elements. The symmetry and

[1] www.comsol.com

boundary conditions of the domain are taken into account at this stage. The number of nodes formulated during the discretisation process will affect the time taken by the processor to converge to a desirable solution.

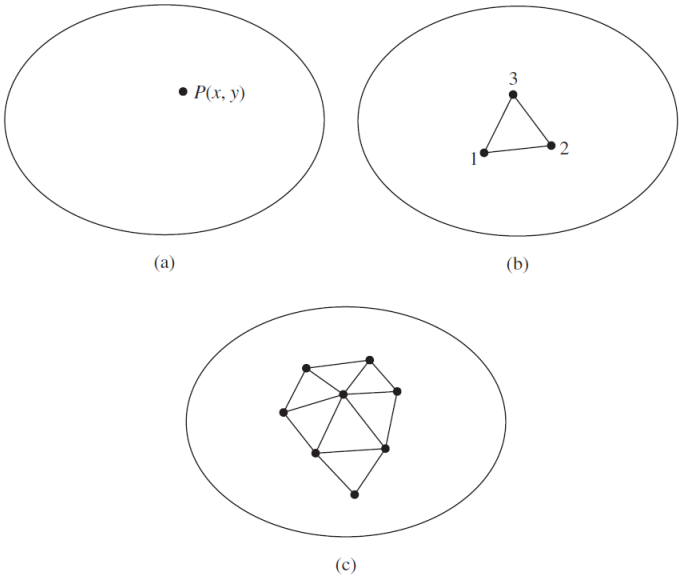

Figure 5.1: Illustration of the basic discretisation of the FEM for 2D geometry; (a) defined 2D domain of field variable $\Phi(x, y)$, (b) 3-node elements defined within the domain and (c) several elements defined within the domain forming the "mesh". Adapted from (Hutton, 2004).

The elements can differ in shapes and sizes and also depend on the working space, i.e. whether the domain is in 1D, 2D or 3D. Figure 5.2 shows the various ways in which a domain can be meshed and the number of external nodes that can be associated with each element.

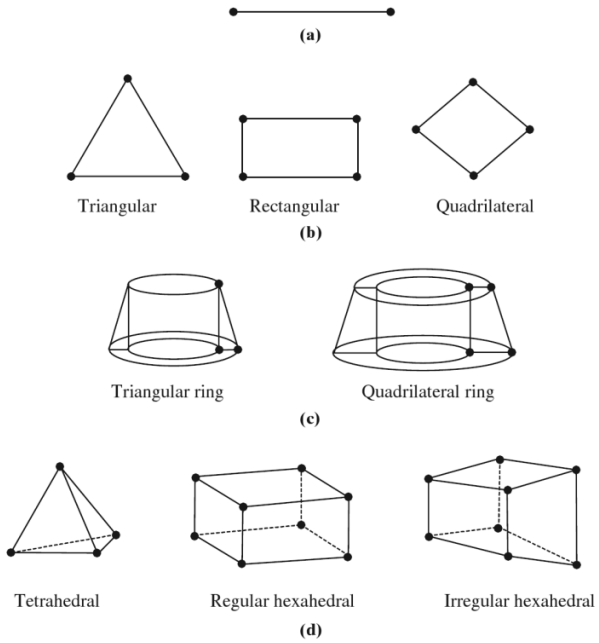

Figure 5.2: Several types of elements that can be defined within a domain; (a) one-dimensional element, (b) two-dimensional elements (c) two-dimensional elements generated into three- dimensional ring elements for axisymmetric geometry and (d) three-dimensional elements. Adapted from (Chung, 2010).

If the field variable to be solved for each element is a scalar quantity, the number of external nodal points in the element will be equivalent to the number of degrees of freedom (DOFs), however, if the the field variable is a vector quantity, the number of DOFs for that particular element will be given by the product of the number of nodes and the number of field variables to be solved (Hutton, 2004). Errors in the FEM computations are inherent, especially when the shape of the domain is irregular. The choice of element type and size is important as it may affect the area that is covered for the computations, e.g. in Figure 5.3.

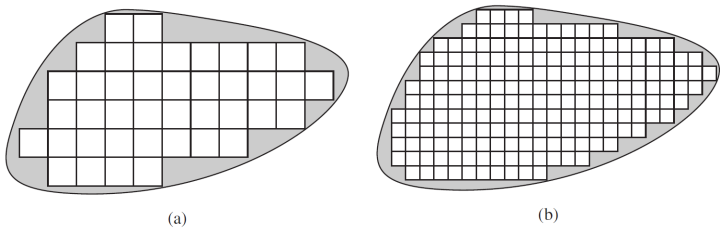

Figure 5.3: Illustration of how the element type and size may affect the magnitude of the errors in FEM, (a) fewer and bigger elements leave a larger uncovered area and (b) smaller elements cover a wide area of the defined domain. Adapted from (Chung, 2010).

3. *Interpolation function selection*

   The best interpolation function for the element must be selected. Evaluating the solution of a defined finite element is achieved through an interpolation function that is dependent

on the number of DOFs of the particular element. The interpolation function is often a predetermined polynomial that satisfies nodal conditions. These interpolation functions will therefore define the behaviour of the field variables within the domain. Simple elements, e.g. 1D elements, may require the use of linear functions, while complex elements may require the use of quadratic or cubic functions to cater for the higher number of nodal points (Hutton, 2004; Sayas, 2008).

4. *Element equation specification*
   The equation matrices for each element are formulated and they describe the properties of each element. Methods such as the direct method, variational method or weighted residual method are used to formulate these matrices. A suitable method must be chosen as it has a significant impact on the quality of results. For an element with n exterior nodes, the element solution is given as:

$$\Phi(x,y) = N_1(x,y)\phi_1 + N_2(x,y)\phi_2 + N_3(x,y)\phi_3 .....N_n(x,y)\phi_n \tag{5.1}$$

   where; $\phi_{1,2,3,....n}$ are field variables at nodal points $1, 2, 3, ...n$ and $N_{1,2,3,.....n}$ are the interpolation functions.

5. *Boundary condition definition*
   The necessary boundary conditions are specified before the system equation is solved. These boundary conditions are either essential or natural boundary conditions. The essential boundary conditions have a direct effect on the degrees of freedom (DOFs) while natural boundary conditions do not (Dixit, n.d.). It is therefore a recommendation in FEM that these boundary conditions are well understood before being imposed on a problem domain to avoid fatal errors.

6. *System equation solution*
   The governing PDE is solved for each element and the set of solutions of each element is then integrated to give the overall solution of the whole system (Sayas, 2008). For a simple system, an exact solution can be obtained, while complex elements will require numerical integration. For example, if the element matrix is denoted as $\mathbf{A^e}$ and the system matrix as $\mathbf{A^s}$ and both the matrices have the same matrix routines, then Figure 5.4 illustrates how the elements can be assembled.

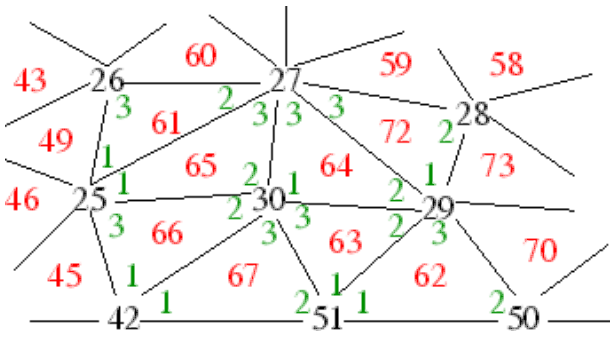

Figure 5.4: A section of a system assembled by adjacent elements. Adapted from (Hollauer, 2007).

From Figure 5.4 it is generally implied that the element matrix 61 is transformed to the system matrix in the following manner (Hollauer, 2007),

$A^{61}_{1,1} \rightarrow A^{s}_{25,25}$, $A^{61}_{1,2} \rightarrow A^{s}_{25,27}$, $A^{61}_{1,3} \rightarrow A^{s}_{25,26}$, ...

hence, for all N elements with a transformation $T(\mathbf{A^e})$, the system matrix can be written as

$$\mathbf{A^s} = \sum\nolimits_{e=1}^{N} T(\mathbf{A^e}). \tag{5.2}$$

This representation illustrates that computations handled for complex systems with different materials can be very extensive.

7. *Presentation of results*
   The desired variables are computed and the results are displayed either in numerical or graphical form.

Figure 5.5 summarises the procedures described, showing the link between the FEM procedure and the necessary actions that complete the model, rendering it ready for analysis.

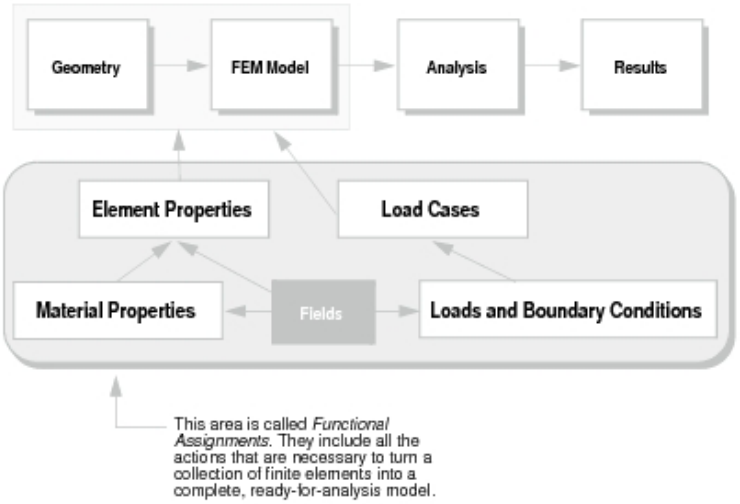

Figure 5.5: The link between the FEM procedure and the necessary steps for making a model ready for analysis. Adapted from (www.mscsoftware.com).

5.2.2 Advantages and disadvantages

Advantages

1. The use of FEM has enabled computations associated with the following scenarios:
    - Irregular geometry
    - Load conditions
    - Non-homogeneous material
    - Higher order elements
2. There is no restriction on the number of elements that can be used for a defined problem domain; hence, such flexibility allows for model expansion and refinement.

Disadvantages

FEM requires digital computers and the computations may be very extensive and take very long, depending on the complexity of the problem (equations and geometry). Since most of the simulations are part of the design process of a real system, human error during the simulation may be fatal. The inherent errors also limit the accuracy of the solutions obtained through this method.

5.3 Modelling in COMSOL Multiphysics

COMSOL Multiphysics is a simulation platform designed to solve a variety of engineering and mathematical problems that include one or more physics concept. Figure 5.6 shows the wide range of packages that are used in a variety of engineering and physics problems.

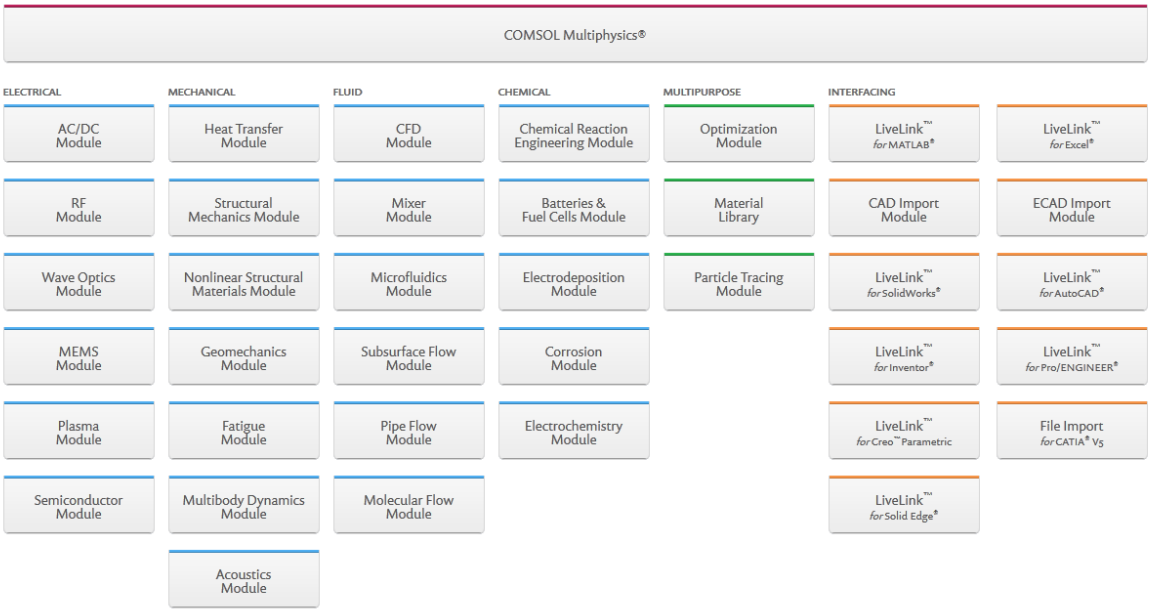

Figure 5.6: Several COMSOL products. Adapted from (www.comsol.com).

The nature of computations discussed in this work falls in the electromagnetics category. The aim is to compute the induced electric field at the Earth consisting of layers having different conductivities, and within the Earth. The induced geoelectric field is then used to compute GIC in a power line. For these computations, the AC/DC module is applicable.

5.3.1 The AC/DC module

The AC/DC module is suitable for low frequency or direct current related electric or magnetic field computations. Problems associated with either dynamic or stationary electric/magnetic fields can be handled. The computations in the module concentrate on solving the differential form of Maxwell's equations with their initial and boundary conditions (COMSOL, 2012). The AC/DC module covers the following interfaces:

- *Electrostatics*
  Applicable to dielectric problems where the charge conservation equation is solved for the electric potential if the distribution of the electric charge within a space is known.

- *Electric currents*
  Applicable to capacitive and conductive mediums where the flow of the AC, DC or transient currents can be studied by solving the current conservation equation for the electric potential.

- *Electric currents, shell*
  The interface is applied to capacitive and conducting thin shells. The flow of the AC, DC or transient currents can be modelled by solving the boundary current conservation equation for an electric potential in 2D, 2D-axisymmetric or in 3D.

- *Magnetic fields*
  This interface solves Ampère's law for the magnetic vector potential and is applicable to magnetostatics, ac and transient magnetodynamics.

- *Magnetic and Electric fields*
  A combination of Ampère's law and the current conservation equation is solved. It addresses problems dealing with magnetostatics and ac magnetodynamics.

- *Magnetic fields, no currents*
  The magnetic flux conservation equation for the magnetic scalar potential is solved for zero current scenarios.

- *Electric circuits*
  The interface allows electrical circuits to be modelled with or without connection and the behaviour associated with circuits to be studied. The behaviour of attributes, such as voltage, capacitance and current flow can be simulated.

5.3.2 Modelling inputs and outputs

The set of equations presented in Chapter 2, section 2.5.1, are solved with the AC/DC module using the *Magnetic field* interface. The model inputs are the measured magnetic field and the conductivity profile necessary for the electric field computations. The desired outputs are the domain induced electric field and current density. Figure 5.7 shows the summarised version of the modelling ,requirements. The *time dependent study* is selected, since the outcome of the computations ought to display the change in the induced electric field with time.

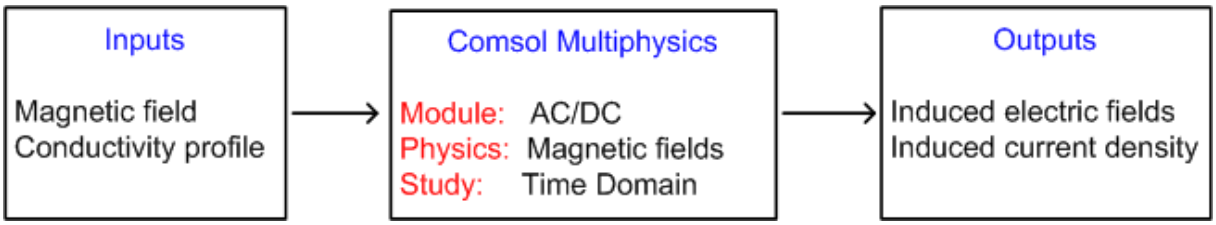

Figure 5.7: The modelling requirements for the computation of geoelectric field using COMSOl Multiphysics.

5.3.3 Data interpolation and extrapolation

The COMSOL platform offers data interpolation methods that can be used when a data set is used as model input. During the interpolation process, a new data set is constructed from the existing discrete data points. These are very important when dealing with big data sets and an appropriate interpolation method has a significant bearing on the outcome.

- *Linear*
  Linear interpolation is generally fast and estimates the new data point by constructing a line between two neighboring data points. The outcome of this method may not be a true representation of the missing value.

- *Piecewise cubic*
  For a given data set, a piecewise cubic interpolation polynomial is composed of a different cubic polynomial in each sub-interval. The piecewise cubic spline function and its first derivative are continuous at the interior nodes.

- *Cubic spline*
  For a given data set, a spline is a polynomial between consecutive data points. The coefficients of these data points are determined such that global smoothness is achieved up to some order of derivative. The cubic piecewise interpolated function is continuous throughout the first and the second derivative within intervals and nodes of interpolation. Splines are preferred over fitting a polynomial for their stability, i.e. they offer less chance of "off" oscillations within the data points.

5.4 Model definition

The derived Grassridge conductivity profile (Ngwira *et al.*, 2008), consists of 9 layers with properties outlined in table 5.1. Three cases are considered when modelling the Earth's layers. The purpose of considering the three cases is to investigate the effects of varying the Earth's structure on the characteristics of the modelled GIC.

Table 5.1: Resistivity vs. depth for the 9 layered planar Earth model.

Layer number	Thickness [km]	Resistivity [Ω]
1	1.1	440
2	3.9	420
3	7	400
4	14	380
5	24	330
6	50	300
7	100	260
8	190	10
9	∞	16

Case 1-Only the conductivities of the first seven layers are considered.
Case 2-The conductivities of the first seven layers are averaged and treated as one layer and the 8^{th} layer conductivity is added.
Case 3-The infinity layer conductivity is considered.

These cases are depicted in Figure 5.8.

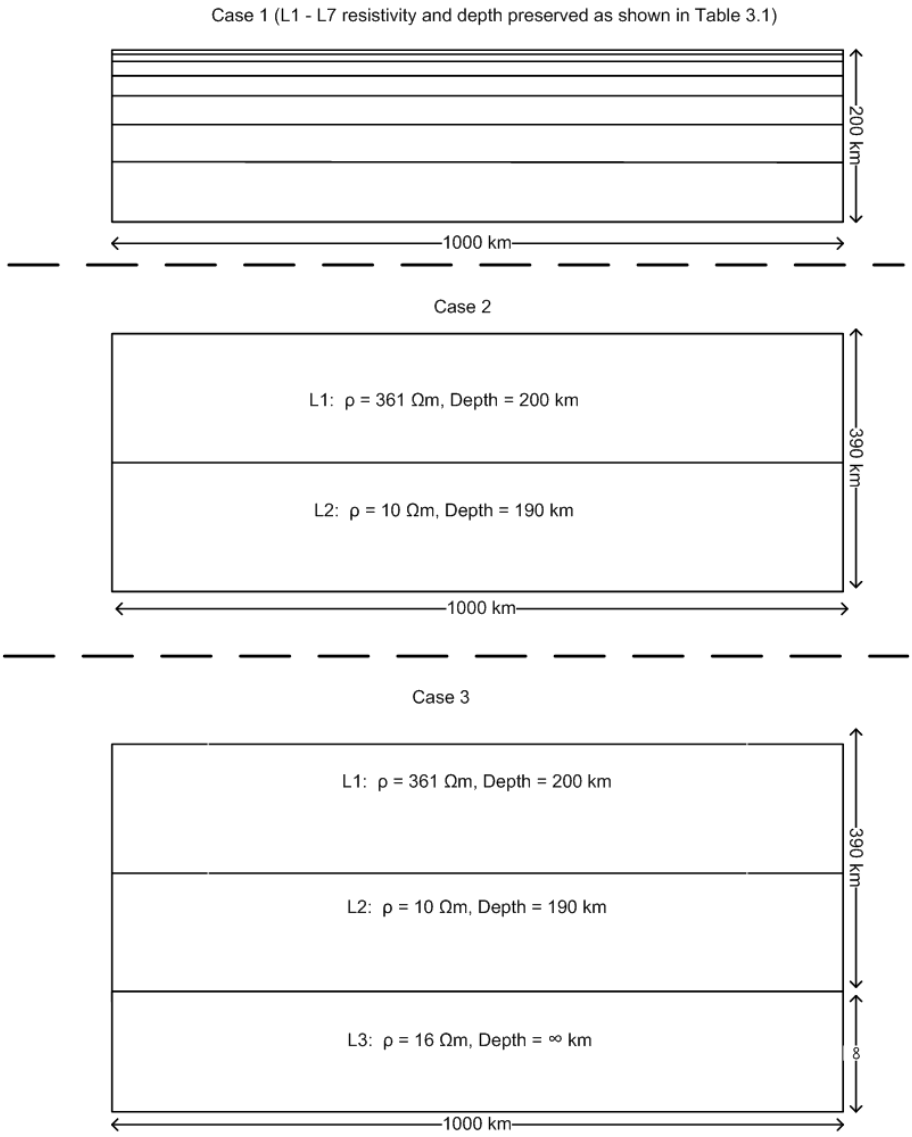

Figure 5.8: Representation of the three modelled ground conductivity structures.

5.4.1 Assumptions

To reduce the complexity of the computations the following assumptions are adopted:

1. The conductivity profile of the areas influenced by the local geological structure . This assumption allows the Earth's surface to be modelled by 2D planar blocks, each with a uniform conductivity.

2. The magnetic field propagates as a plane wave vertically downwards and, hence, only horizontal components of the electric field will be considered in the computation.

3. The computations are localised; i.e. *leq* 1000 km dimensions are considered, thus the Earth's curvature is ignored in the model.

5.5 Detailed modelling

The steps involved in building up the model in COMSOL Multiphysics are presented. The graphics shown are for the Case 1 Earth structure. The procedure was repeated for Case 2 and Case 3. This is not a step by step instruction of building the model but an overview of the whole modelling process.

- *Earth domain*

  The construction of the layered Earth model in the simulation platform is done in the $x-z$ plane. The surface of the Earth is in the x-axis. The interest is therefore in the variation of the induced geoelectric field ($E_{x,y}$) in the z-axis. It is important at this stage to make sure that all layers are properly joined to each other for continuity of the Earth's structure. This is achieved through the built-in "Union"' function. Figure 5.9 shows the 7 adjacent layers as constructed in the simulation platform. A discontinuous domain will present errors during the evaluation of the solution.

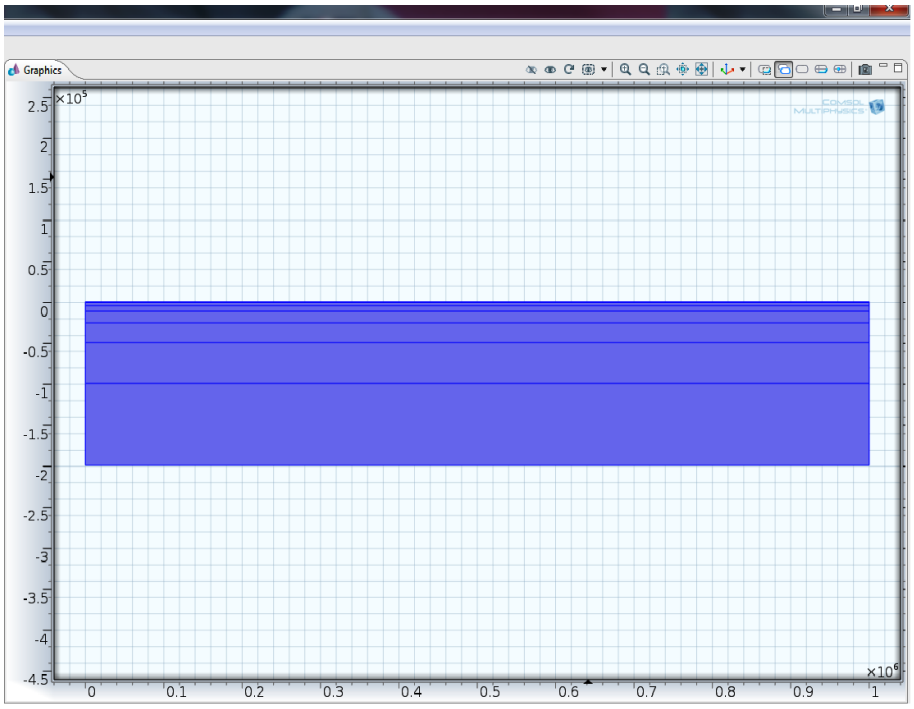

Figure 5.9: COMSOL Multiphysics model representing a 7 layered flat Earth.

- *Magnetic field data*

  The magnetic field is introduced in the model on the surface as a *piecewise cubic* interpolated function. One magnetic field component is loaded at a time, that is either the B_x or B_y component. In the current case, magnetic field data measured at one-minute intervals are used.

- *Boundary conditions*

  To keep the magnetic field uniform within the model, a "perfect magnetic conductor" boundary condition was set on the left and right edges of the model as shown by the blue

lines in Figure 5.10. This boundary condition, implying $\mathbf{n} \times \mathbf{H} = 0$, prevents tangential components of the magnetic field at the edges of the model and ensures continuity of the perpendicular components.

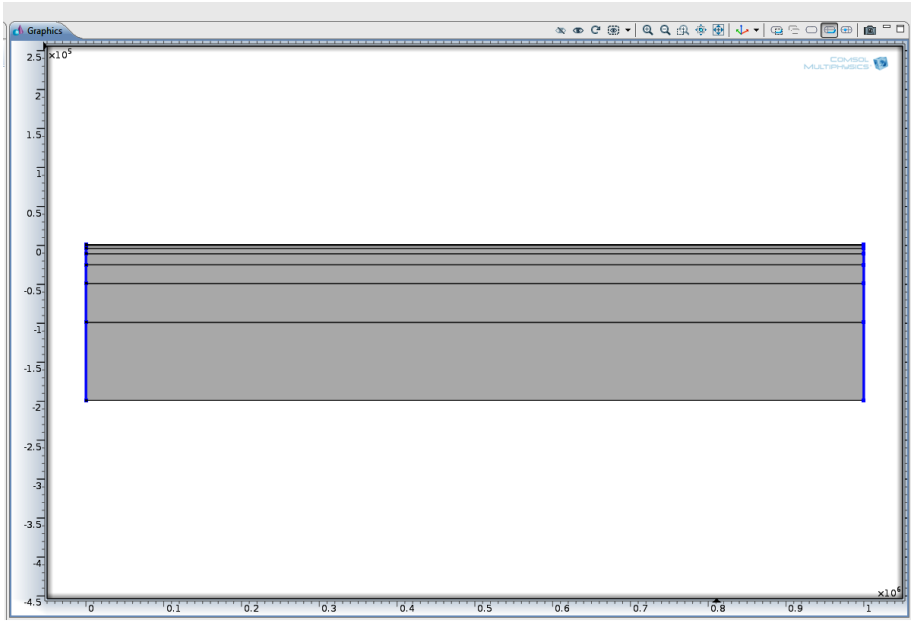

Figure 5.10: Assignment of the boundary conditions. Magnetic insulation boundaries shown in blue.

The "magnetic insulation" boundary condition was set at the bottom of the model to ensure that the induced currents can only flow in the normal direction. Figure 5.11 shows how these boundary conditions can be interpreted in a model.

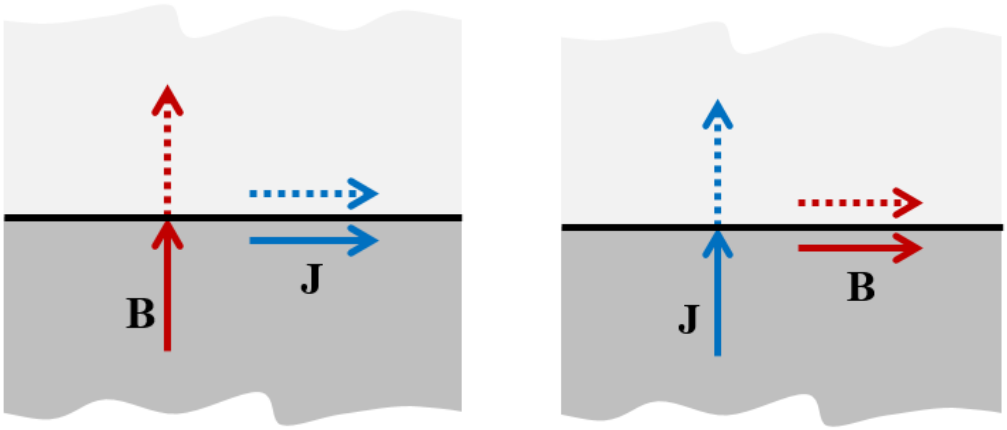

(a) Perfect magnetic conductor boundary condition

(b) Magnetic insulation boundary condition

Figure 5.11: A demonstration of the interpretation of the (a) Perfect magnetic conductor (b) Magnetic insulation boundary conditions when modelling magnetic field. Adopted from (Frei, 2014).

- *The system equations*

  The layers of the Earth are considered to be sub-domains. For each sub-domain, Ampère's law, given by equation 5.3, is solved.

$$\sigma \frac{\partial \mathbf{A}}{\partial t} + \nabla \times (\mu_0^{-1} \mu_r^{-1} \mathbf{B}) \times \mathbf{B} = \mathbf{J} \tag{5.3}$$

$$\mathbf{B} = \nabla \times \mathbf{A} \tag{5.4}$$

  and

$$\mathbf{E} = \frac{\mathbf{J}}{\sigma} \tag{5.5}$$

  where $\mathbf{A}$ is the magnetic vector potential, $\mathbf{B}$ is the magnetic flux density, σ is the conductivity, $\mathbf{v}$ is the velocity of the conductor ((which is zero in the current case as there is no moving media in the model), μ_r is the relative permeability and $\mathbf{J}$ is the current density.

- *The mesh*

  An *extremely fine* mesh size of triangular elements was used on the current model. This yielded a total number of 11137 elements that are shown in Figure 5.12. The size of the mesh has a significant bearing on the computation time. While few elements may take a short while to converge to the estimated solution, the accuracy of the solution may be compromised.

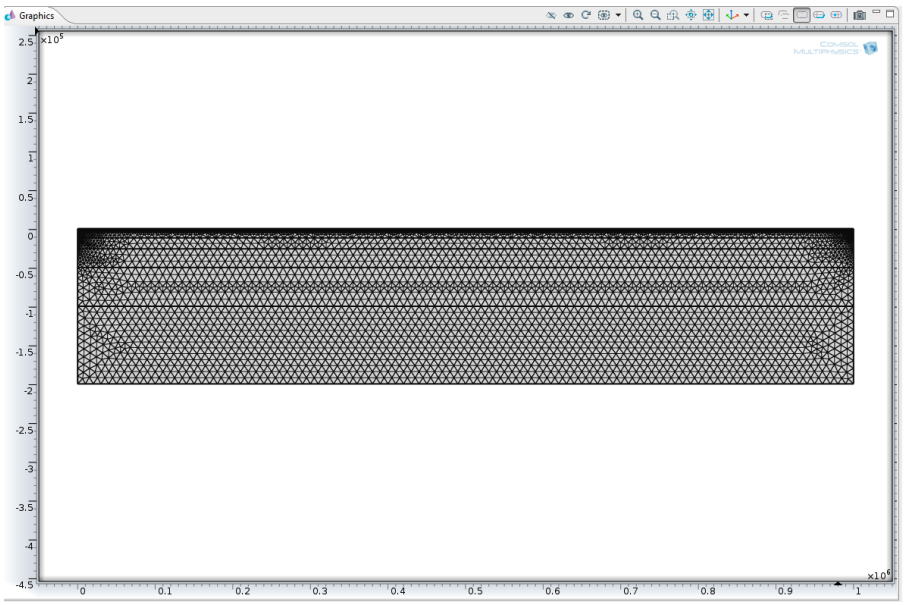

Figure 5.12: Model of the layered Earth divided into triangular elements

- *Computation*

  The final step of the process is to allow the computation of the desired variables. A *time dependent* study is used for the computation of the induced current density and the electric field within the several layers of the domain. The electric field is then used to compute the GIC that are likely to be driven into any grounded technological system in the vicinity.

5.6 Conclusion

The basic concepts applied in FEM and the significant steps followed in defining the 2D model in COMSOL have been presented. The results obtained from the constructed models and the computational procedure followed, are presented in the next chapter.

CHAPTER 6: RESULTS OF MODELLING GIC USING THE FINITE ELEMENT METHOD

6.1 Introduction

COMSOL Multiphysics, is used to compute the electric field induced in a layered Earth model using the magnetic field measured at Hermanus Magnetic Observatory (HER) and the magnetic field interpolated from the HER and the Hartebeesthoek Magnetic Observatory (HBK).

This chapter presents a comparison of GIC modelled using FEM with GIC measured at the Grassridge substation for the Halloween 2003 geomagnetic storm. Typical current density distributions and electric field variations are discussed for two selected instances. It is worth noting that Grassridge is not the only power station at which GIC measurements have been done in South Africa. The site is chosen as a case study because it is currently the only station in South Africa for which a 1D layered conductivity profile has been derived. Thus, the Grassridge conductivity profile is used to test the applicability of FEM in modelling GIC, using measured geomagnetic field as model input. The Halloween storm makes a significant case study as there are good quality GIC data from the Grassridge substation for the corresponding stormy days.

According to the NOAA space weather scale for geomagnetic storm intensity, the Halloween storm has periods of G4 (Severe) and G5 (Extreme) intensity. At this magnetic storm intensity, the anticipated effects on the power systems include widespread voltage control problems, protective relay tripping, transformer damage, as well as blackouts.

6.2 Input data

The geomagnetic field measured at HER, and the magnetic field interpolated to the Grassridge substation using the Spherical Elementary Current System (SECS) method, based on the geomagnetic field measured at HER and HBK from 29 to 31 October 2003, are used as inputs for the FEM model. For the GIC calculation, either the rate of change of the horizontal components of the magnetic field or the horizontal components of the magnetic field itself may be used, depending on the mathematical formulation of the model (Marti *et al.*, 2014; Pirjola, 2010). For the formulation used in the COMSOL Multiphysiscs model, the horizontal magnetic field components are used as input. Only the B_x and B_y components at the location of interest are used for computation of the corresponding E_y and E_x, respectively.

The horizontal magnetic field components, B_x and B_y, and the rate of change, $\partial B_x/\partial t$ and $\partial B_y/\partial t$, of the magnetic field measured at HER for the selected period are illustrated in Figure 6.1. The interpolated magnetic field data set based on the HBK and HER data sets and the corresponding rate of change are shown in Figure 6.2. The interpolated data set is designated as INT.

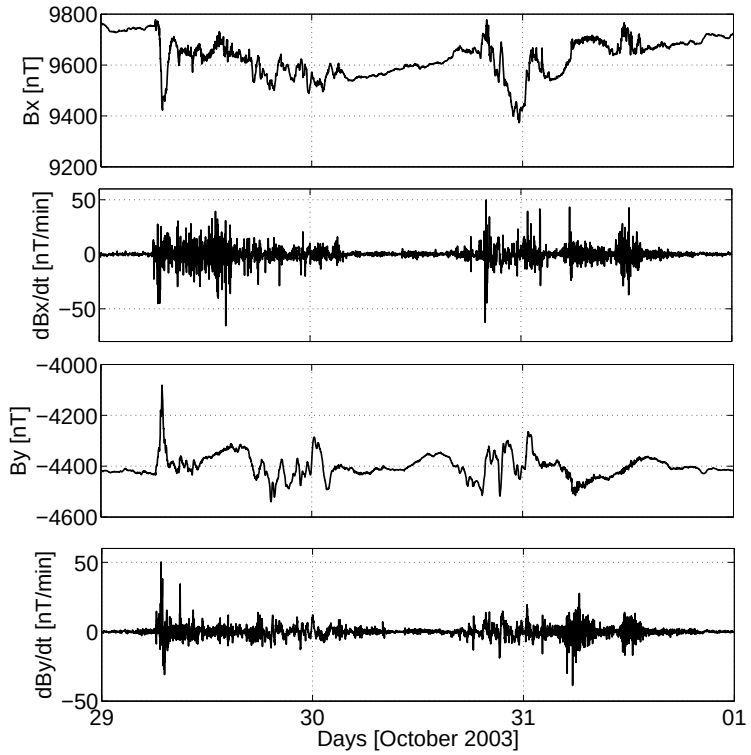

Figure 6.1: B_x, $\partial B_x/\partial t$, B_y **and** $\partial B_y/\partial t$ **for 29 to 31 October 2003 as measured at HER observatory.**

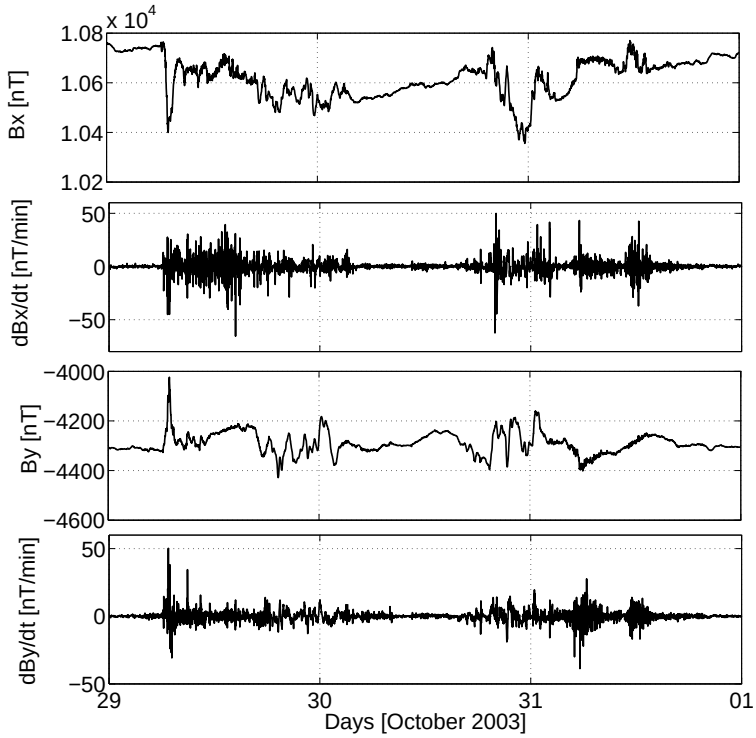

Figure 6.2: B_x, $\partial B_x/\partial t$, B_y **and** $\partial B_y/\partial t$ **for 29 to 31 October 2003 interpolated to the Grassridge substation based on the measurements at HBK and HER observatories.**

6.3 Conductivity structure variation analysis

The computation of the horizontal electric field is referred to as the geophysical step in GIC modelling. In the current study, the electric field is computed from measured magnetic field data. Equations described in section 2.4.3 are the basis of the electric field computations. The horizontal electric field components, E_x and E_y, are computed using the default equations of the AC/DC module of COMSOL Multiphysics.

The 1D layered Earth conductivity profile for Grassridge was derived by Ngwira *et al.* (2008). The chapter presents three conductivity structures (Case 1, Case 2 and Case 3), which were derived from Ngwira's profile. The three structures are shown in Figure 5.8. The purpose of this investigation is to determine the best way to represent the Grassridge conductivity structure in a finite element model for optimised results. The modelled GIC are compared to the measured GIC for the three consecutive storm days.

6.3.1 Presentation of method and results

For the Grassridge substation, there are two sets of network coefficients that have been derived independently in previous studies. The two sets of network coefficients are $a = -80Akm/V, b = 15Akm/V$ as derived by Koen (2002) and $a = -80Akm/V, b = 1Akm/V$ as derived by Ngwira *et al.* (2008). Koen (2002) used the Lehtinen-Pirjola (LP) method described (Lehtinen and Pirjola, 1985) to derive the network coefficients as in equations 2.47 and 2.48. Ngwira *et al.* (2008) used the method described by Pulkkinen *et al.* (2007) where measured GIC and and the estimated electric field are used.

For the modelling of GIC using FEM calculated electric field, both sets of network coefficients are considered in this study. For each conductivity profile investigated, the maximum electric field for each layer is computed. The modelled GIC is computed using the electric field at the Earth's surface for that particular configuration. In all GIC comparison figures, the top panel presents a comparison of measured GIC and GIC computed using the coefficients, $a = -80Akm/V, b = 15Akm/V$ and the bottom panel presents a comparison of measured GIC and GIC computed using the coefficients $a = -80Akm/V, b = 1Akm/V$. The maximum measured GIC during the period of interest was 13.2 A recorded on 29 October 2003. Peak GIC for 30 and 31 October were 9.94 A and 8.44 A, respectively.

The three parameters used for comparing the output of the GIC modelled with the measured GIC for the three conductivity profiles are, the difference between the peak GIC (—measured GIC - modelled GIC—), ΔI, the root-mean-square error (RMSE) and the correlation coefficient (R).
For each case presented, the electric field displayed in the figures was extracted from the simulation platform as the average of the domain (i.e. the block representing a certain layer). In figures 6.3 and 6.4 for Case 1, the thickness of the top layer is relatively small and the average electric field of the domain is the same as the electric field extracted from the top layer boundary (L1 = Surface). This however, is not the case with Cases 2 and 3. For these particular scenarios, the top boundary

of the first layer is regarded as the surface and L1, L2 and L3 are modeled domains representing the conductivity layers as described for each case. The electric field considered for GIC computation is extracted from the top layer boundary referred to as the surface.

6.3.2 Case 1

The first configuration of the Earth's profile consists of the first 7 layers of the Ngwira 1D profile. The resistivity of these layers decreases with depth; the respective resistivity values at corresponding thicknesses are [440, 420, 400, 380, 330, 300, 260] Ωm at [1.1, 3.9, 7, 14, 24, 50, 100] km. This case was considered to evaluate if the poorly conducting layers of this profile are adequate for calculating the electric field associated with the GIC.

Figure 6.3 shows the FEM computed electric field for the three consecutive storm days for each layer using Hermanus (HER) data. Figure 6.4 shows the maximum FEM computed electric field computed using the interpolated (INT) data. In Figures 6.3 and 6.4 the electric field for L2-L7 are offset to enhance readability. The measured and modelled GIC are compared in Figures 6.5 and 6.6. The GIC are calculated with the electric field estimated at the surface of the Earth (L1). L1 is the top layer. Table 6.1 shows model performance analysis based on the Δ I, RMSE and R for the three consecutive days as well as for each storm day.

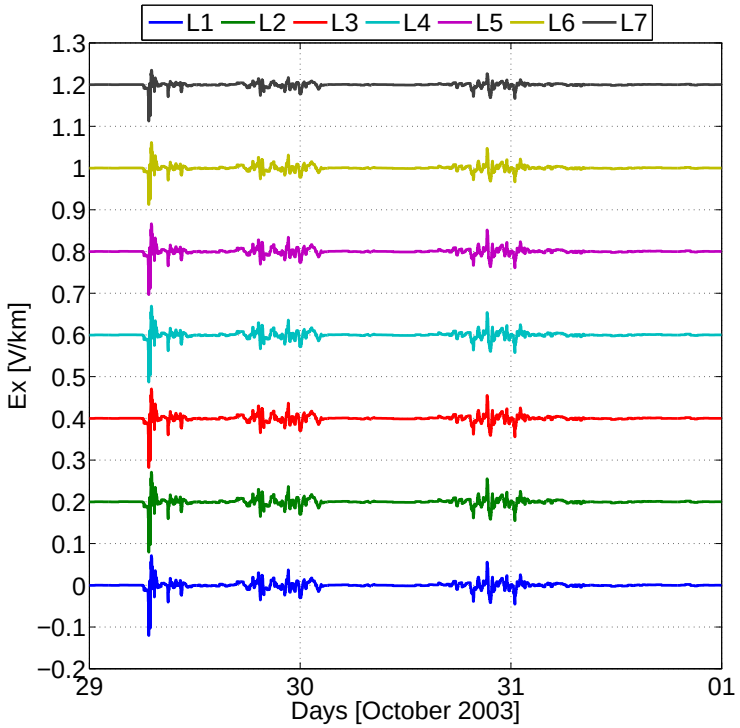

(a) E_x

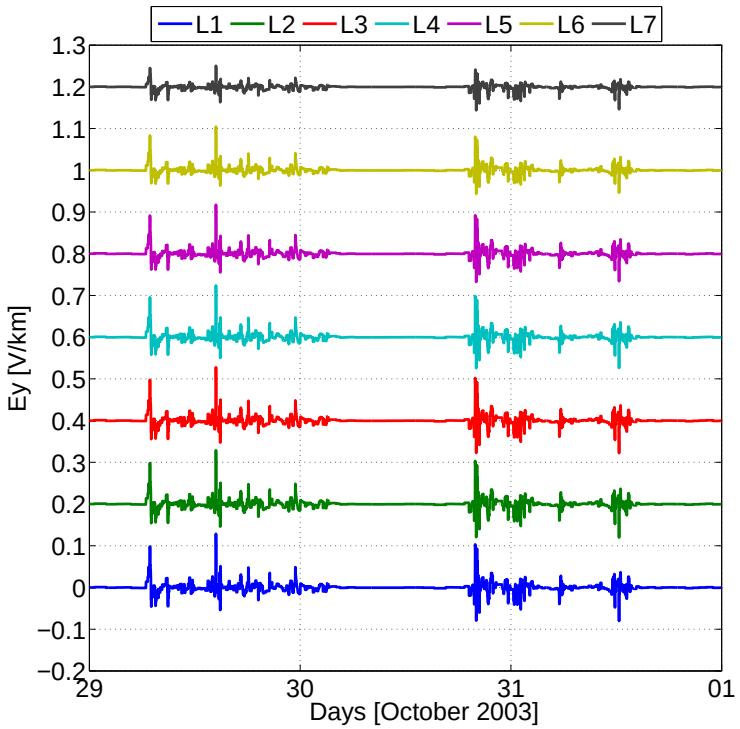

(b) E_y

Figure 6.3: The horizontal electric field components, E_x and E_y for the 7 layers calculated using HER data. L2's electric field is centered at 0.2 V/km, L3 at 0.4 V/km, L4 at 0.6 V/km, L5 at 0.8 V/km, L6 at 1.0 V/ km and L7 at 1.2 V/km.

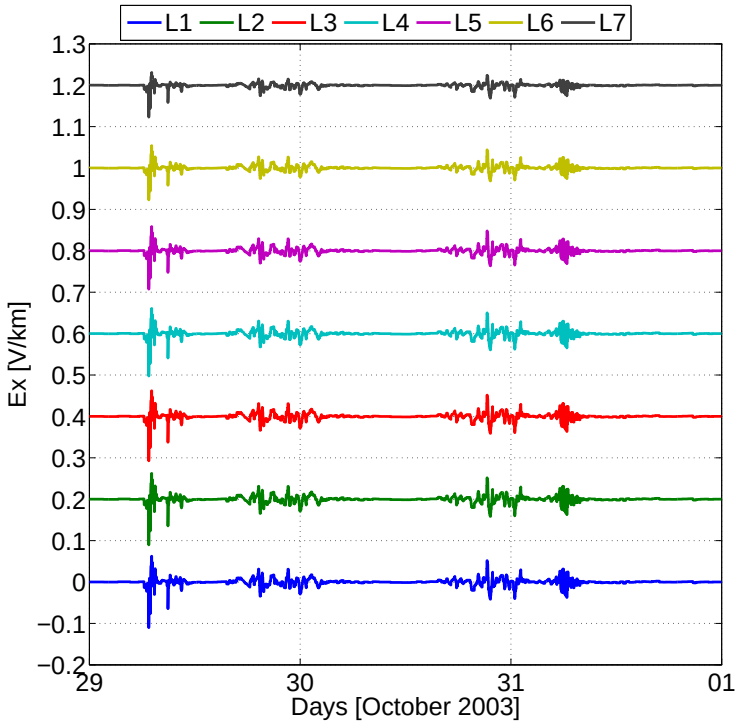

(a) E_x

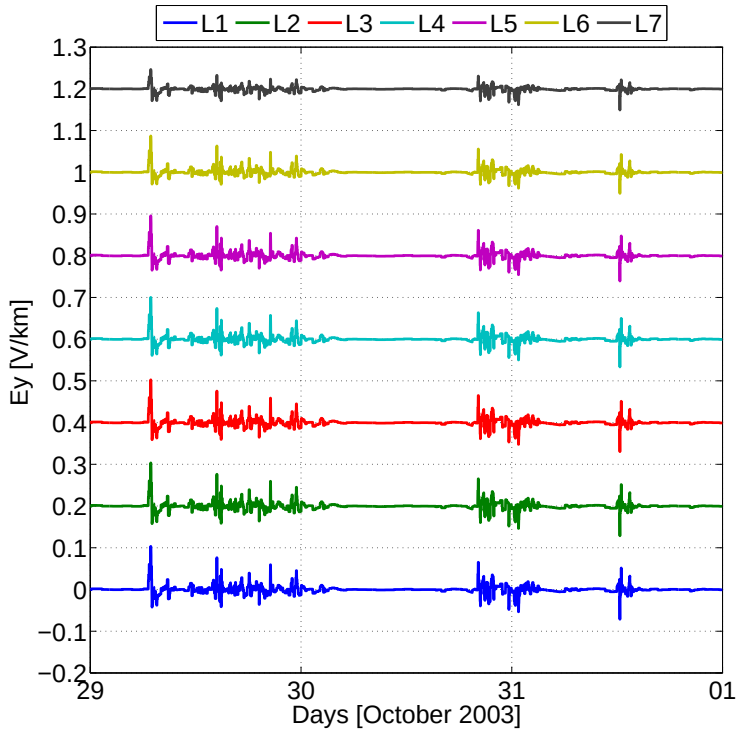

(b) E_y

Figure 6.4: The horizontal electric field components, E_x and E_y, for the 7 layers calculated using INT data. L2's electric field is centered at 0.2 V/km, L3 at 0.4 V/km, L4 at 0.6 V/km, L5 at 0.8 V/km, L6 at 1.0 V/ km and L7 at 1.2 V/km.

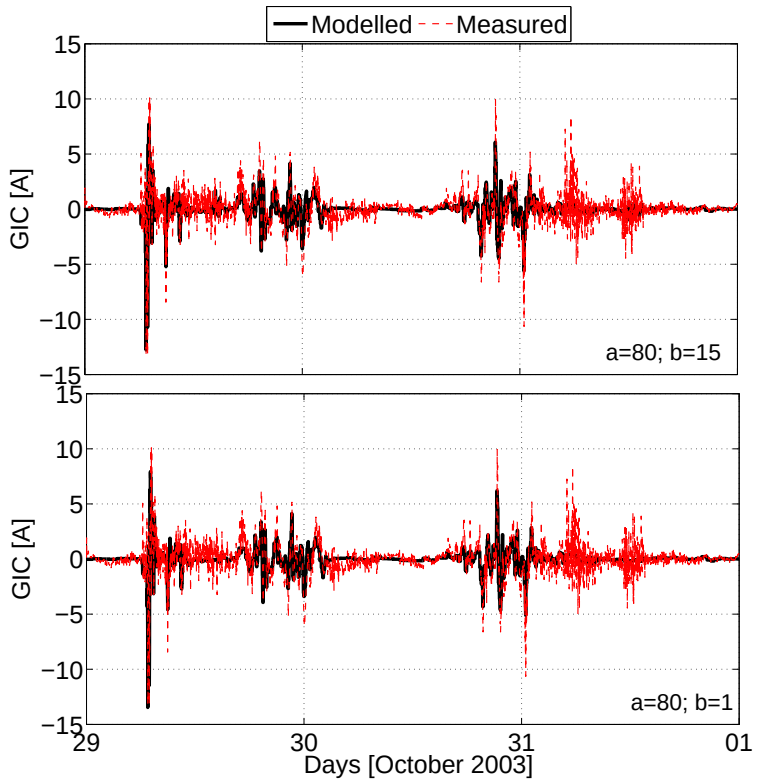

Figure 6.5: Measured and modelled GIC using HER data for Case 1 conductivity profile.

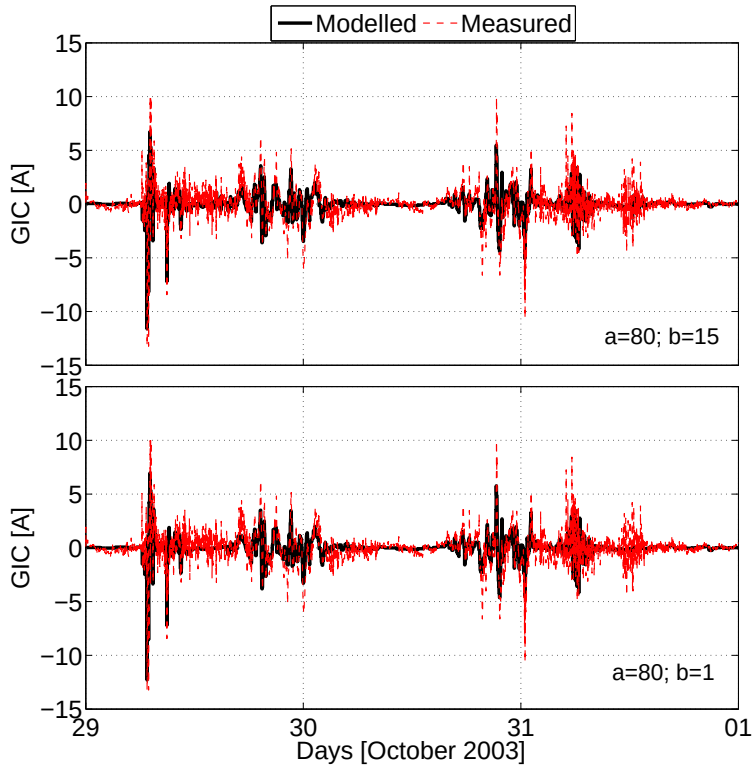

Figure 6.6: Measured and modelled GIC using INT data for Case 1 conductivity profile.

Table 6.1: Performance analysis for the FEM model using HER and INT geomagnetic data sets: Case 1.

	ΔI [A]	RMSE [A]	R [%]	ΔI [A]	RMSE [A]	R [%]
	$a = 80, b = 1$			$a = 80, b = 15$		
	29-31 October 2003					
HER	0.26	1.03	71	0.40	1.03	70
INT	0.91	1.04	70	2.00	1.06	69
	29 October 2003					
HER	0.26	1.11	77	0.40	1.11	77
INT	0.91	1.11	77	2.00	1.13	77
	30 October 2003					
HER	3.75	0.81	84	3.87	0.85	81
INT	4.17	0.84	83	4.88	0.89	80
	31 October 2003					
HER	8.04	1.01	58	8.04	1.02	56
INT	5.00	0.95	62	4.11	0.94	63

For the three consecutive days, an average of 70 % correlation coefficient between the measured and modelled results is obtained when either HER and INT data are used. The difference in the calculated RMSE between using the a and b coefficients of Koen (2002) or Ngwira (2008) is less

than 0.06 A. When considering individual days, the electric field derived from the FEM model estimates the peak GIC of the 29^{th} to be 0.26 A below the measured value when HER data is used with the Koen coefficients but in the case when INT data is used with the Ngwira network coefficients the modelled value is above the measured value. For the 30^{th}, peak GIC is underestimated by 3.75 A to 3.87 A for the HER data and 4.17 A to 4.88 A for INT data. However, higher values of correlation coefficient and lower RMSE values are obtained for this particular day compared to the other two days. Peak values of the modelled GIC for the 31^{st} of October are very low despite the low RMSE values obtained. When HER data for 31 October is used, the peak value of the modelled GIC is only 5 % of the measured GIC while INT data estimates ≈50 % of the peak GIC. The 31^{st} is also the day with the lowest calculated correlation coefficient values.

6.3.3 Case 2

For the second conductivity profile configuration (Case 2), 2 layers are considered. The first layer (L1) has a resistivity which is the average of the top 7 layers of the Ngwira model and the second layer (L2) has the resistivity of the 8th layer of the Ngwira model; resistivity = [361, 10] Ωm at depth [200, 190]. The purpose of considering this layer is to evaluate the effect of a less resistive layer underlying a high resistivity layer on the calculated electric field.

Figure 6.7 shows the maximum FEM computed electric field for the three consecutive storm days for each layer using HER data for Case 2. Figure 6.8 shows the maximum FEM computed electric field for the three consecutive storm days for each layer using the interpolated data. The measured and modelled GIC for Case 2 are shown in Figures 6.9 and 6.10. Table 6.2 shows differences in the peak currents, the RMSE and the correlation coefficient for the storm period.

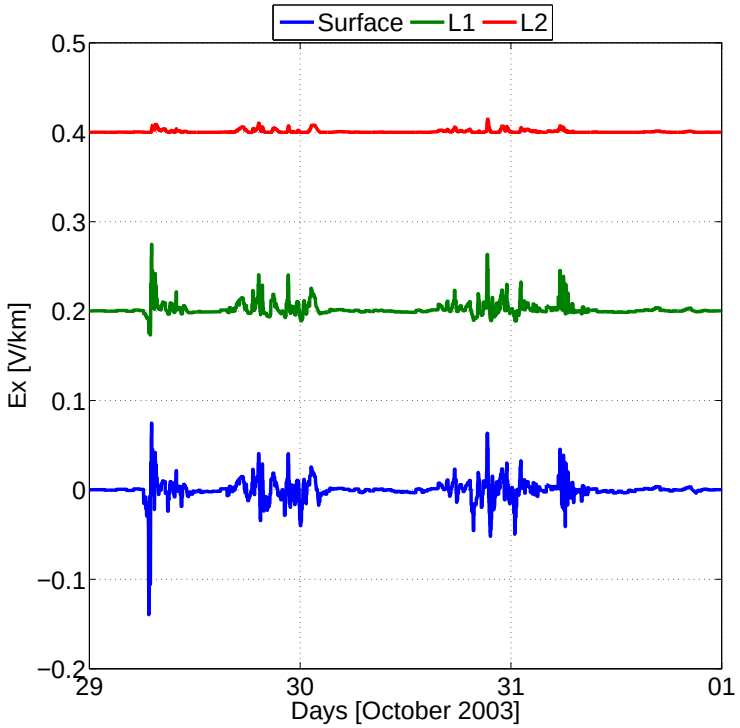

(a) E_x

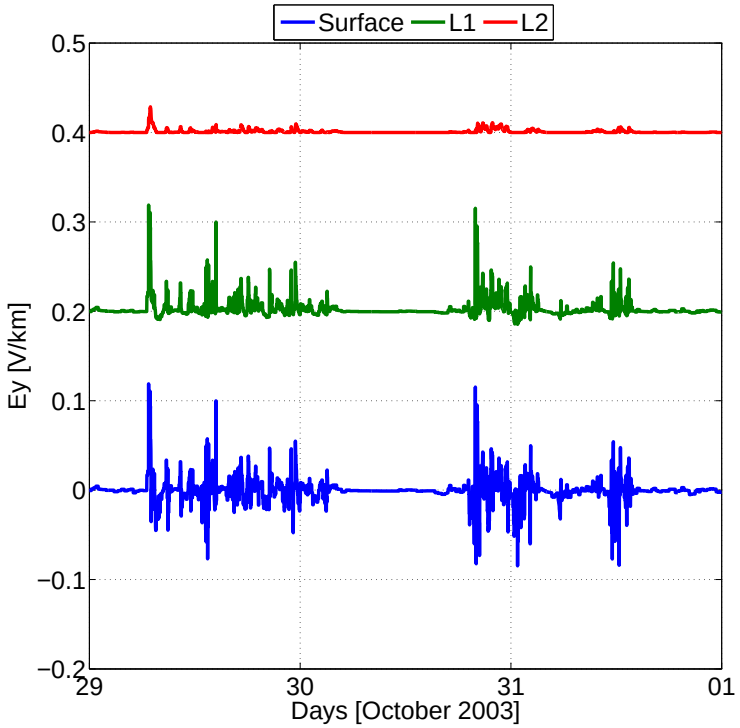

(b) E_y

Figure 6.7: The horizontal electric field component, E_x and E_y, computed for the surface and the 2 layers calculated using HER data. L1's electric field is centered at 0.2 V/ km, L2 at 0.4 V/km.

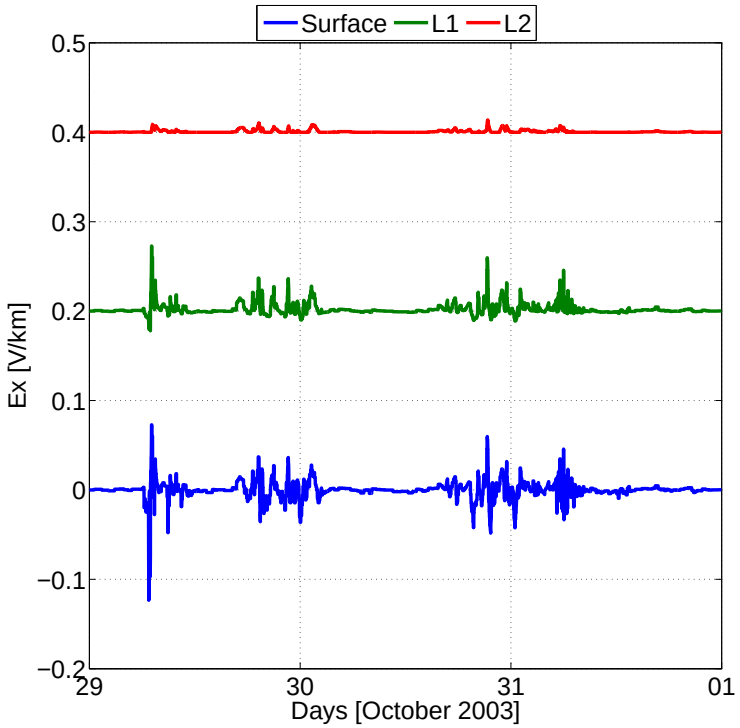

(a) E_x

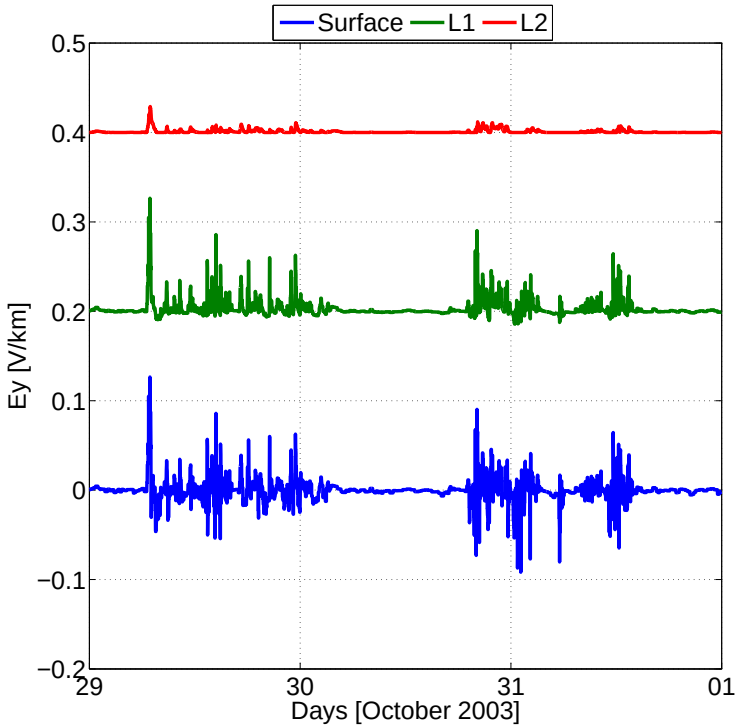

(b) E_y

Figure 6.8: The horizontal electric field component, E_x and E_y, computed for the surface and the 2 layers calculated using INT data. L1's electric field is centered at 0.2 V/ km, L2 at 0.4 V/km.

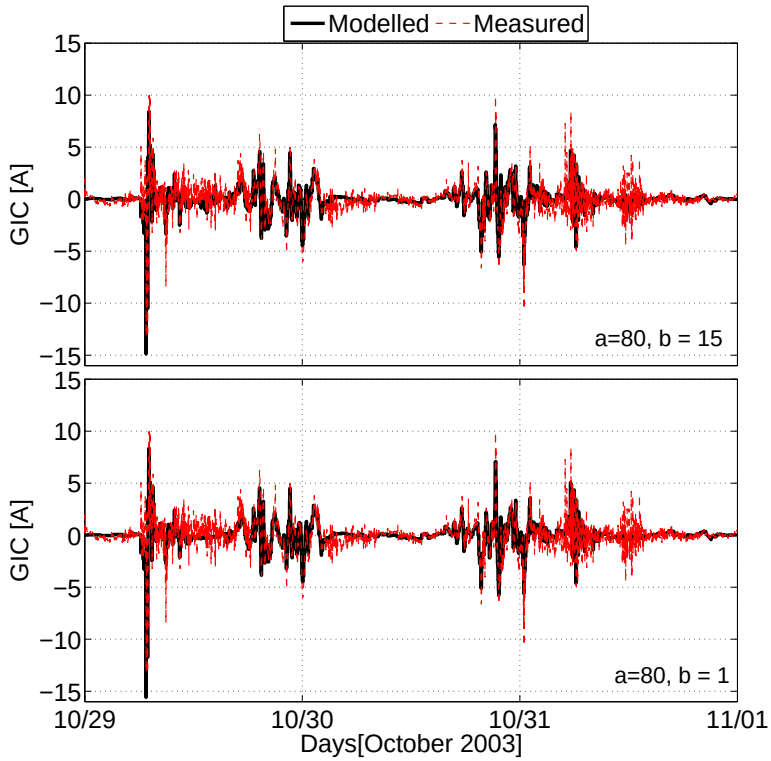

Figure 6.9: Measured and modelled GIC using HER data for Case 2 conductivity profile.

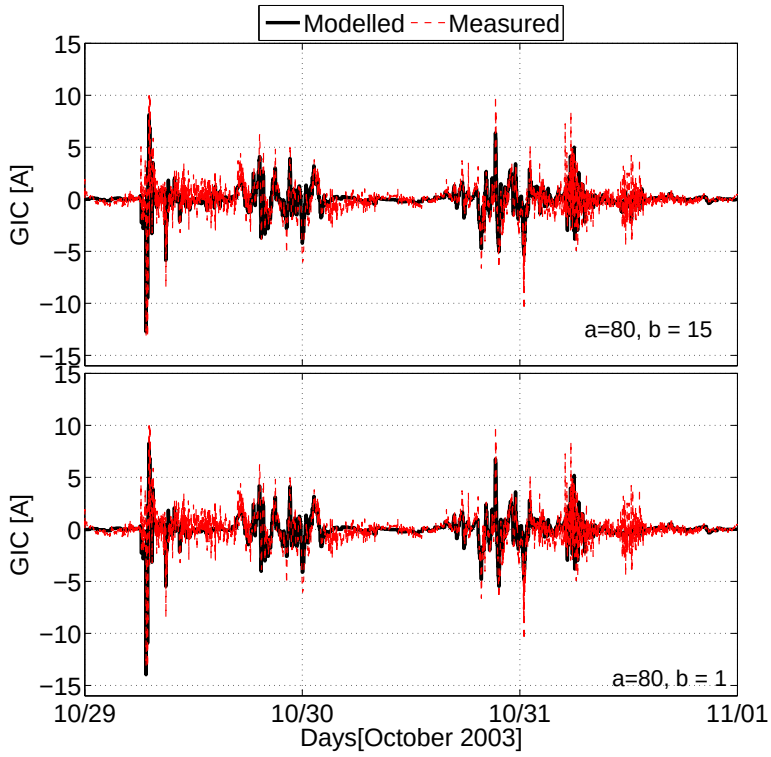

Figure 6.10: Measured and modelled GIC using INT data for Case 2 conductivity profile.

Table 6.2: Performance analysis for the FEM model using HER and INT data sets: Case 2

	ΔI [A]	RMSE	R [%]	Δ I [A]	RMSE	R[%]
	$a = 80, b = 1$			$a = 80, b = 15$		
	29-31 October 2003					
HER	2.4	0.97	75	1.7	0.98	74
INT	0.80	0.97	74	0.46	1.0	72
	29 October 2003					
HER	2.4	1.09	78	1.7	1.08	78
INT	0.80	1.04	80	0.46	1.05	80
	30 October 2003					
HER	2.87	0.65	89	2.76	0.69	87
INT	3.56	0.67	88	3.18	0.72	86
	31 October 2003					
HER	3.76	0.93	64	3.38	0.92	63
INT	3.37	0.94	64	3.25	0.92	61

An average of 75 % correlation coefficient is obtained over the storm period for both HER and INT data sets. The RMSE values averaged over the period 29-31 October are slightly lower than those obtained for Case 1, by an average of 0.05 A. The HER data underestimates the measured GIC by 2.4 A and 1.7 A while the INT data underestimates the measured GIC by 0.8 A if the Ngwira coefficients are used and by 0.46 A if the Koen coefficients are used. As in Case 1, the RMSE errors computed for the 30^{th} are low (an average of 0.68 A) and higher correlation coefficient values (¿ 85 %) are obtained than on the other days. For the 30^{th}, peak GIC is underestimated by between 2.76 A and 2.87 A for the HER data and between 3.18 A and 3.56 A for the INT data. The correlation coefficients for the 31 October are relatively low when compared to the other two days (an average of 63 %), and the peak GIC estimated are between 55 % and 61 % of the peak measured GIC.

The representation in Case 2 is similar to the case of a poorly conducting surface layer above a highly conducting bottom discussed by Pirjola (2010). In such a profile it has been concluded that the electric field is proportional to the rate of change of the horizontal magnetic field measured at the Earth's surface and can be approximated as;

$$E_y(t) = -dg(t) \tag{6.1}$$

where d is the thickness of the top layer and $g(t)$ is the rate of change of the measured magnetic field.

Figure 6.11 shows a comparison of the electric field calculated using equation 6.1 and the FEM calculated E_y. For electric field calculation the rate of change of the B_x component of the INT data

were used and is compared with E_y calculated using B_x of the INT data in FEM. It is observed that there is good correlation between the calculated electric field for these two approaches. This result shows that the FEM calculated electric field calculations compares well with the method derived by Pirjola (2010).

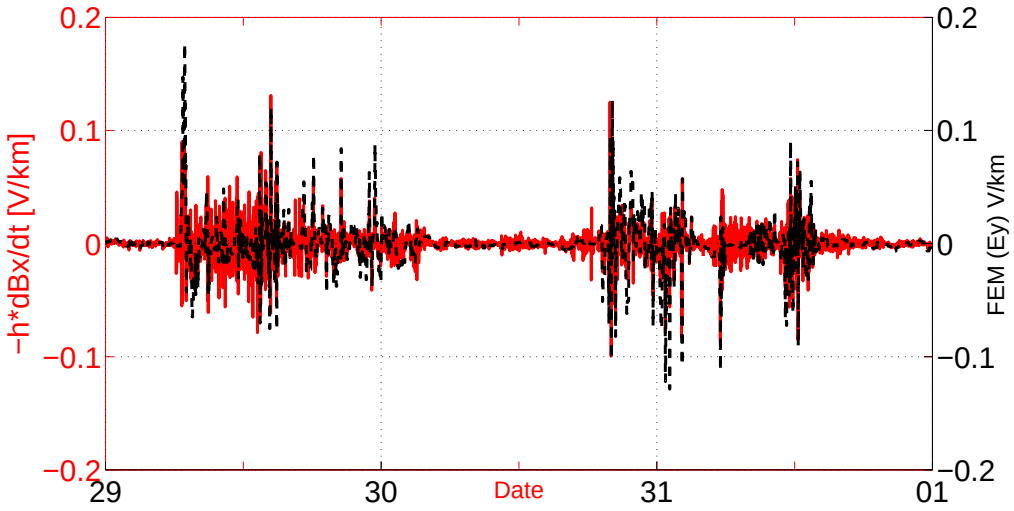

Figure 6.11: Electric field calculated with FEM compared with the electric field calculated using equation 6.1.

6.3.4 Case 3

For the third conductivity profile configuration (Case 3), 3 layers are considered. The first layer (L1) has a resistivity, which is the average of the top 7 layers of the Ngwira model. The second layer (L2) has the resistivity of the 8th layer of the Ngwira model and the third resistivity is that of the terminating half-space (L3); resistivity = [361, 10, 16] Ωm at depth = [200, 190, ∞] km.

Figure 6.12 shows the maximum FEM computed electric field for each layer using HER data for the three consecutive storm days. Figure 6.13 shows the maximum FEM computed electric field for the three consecutive storm days for each layer using the INT data. The measured and modelled GIC are compared in Figures 6.14 and 6.15. Table 6.3 shows the model performance analysis.

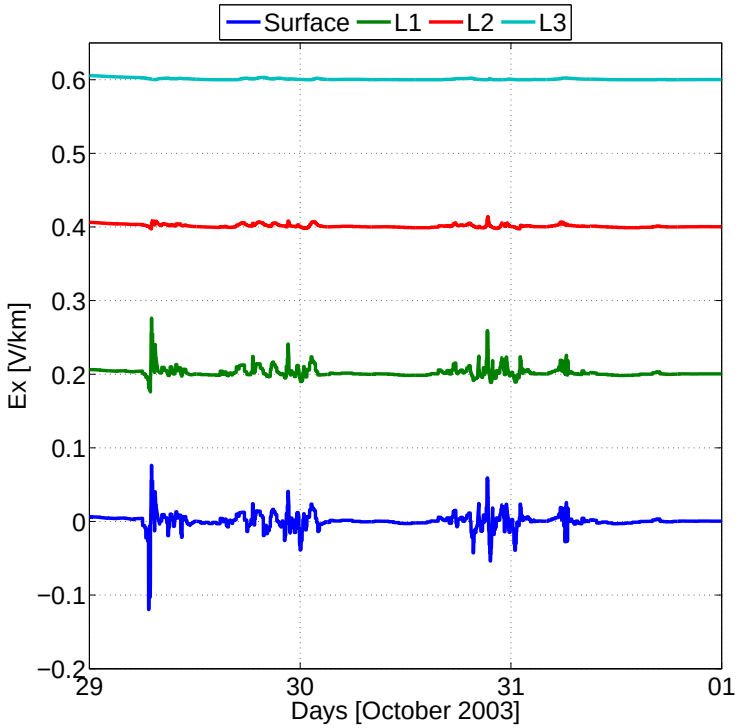

(a) E_x

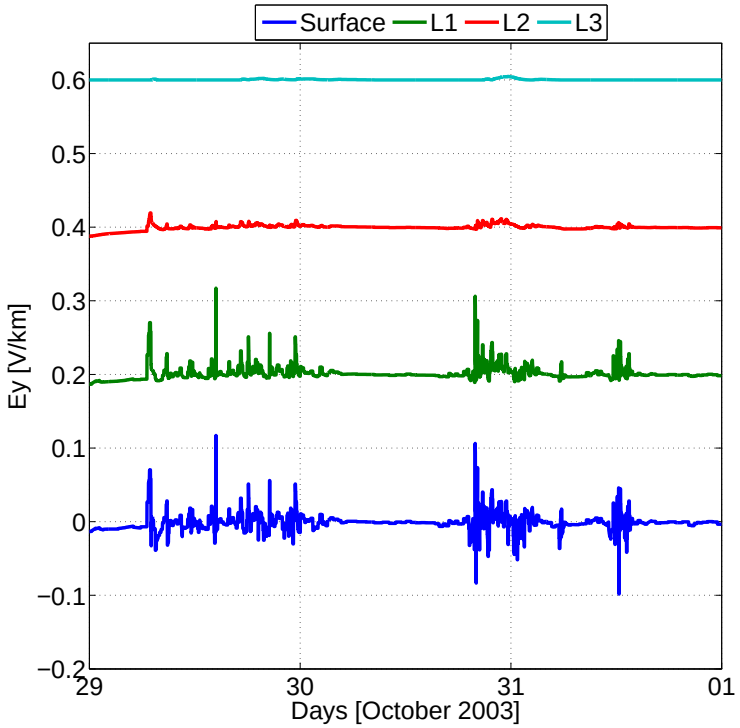

(b) E_y

Figure 6.12: The horizontal electric field components, E_x and E_y, computed for the surface and the 3 layers calculated using HER data. L1's electric field is centered at 0.2 V/km, L2 at 0.4 V/km and L3 at 0.6 V/km.

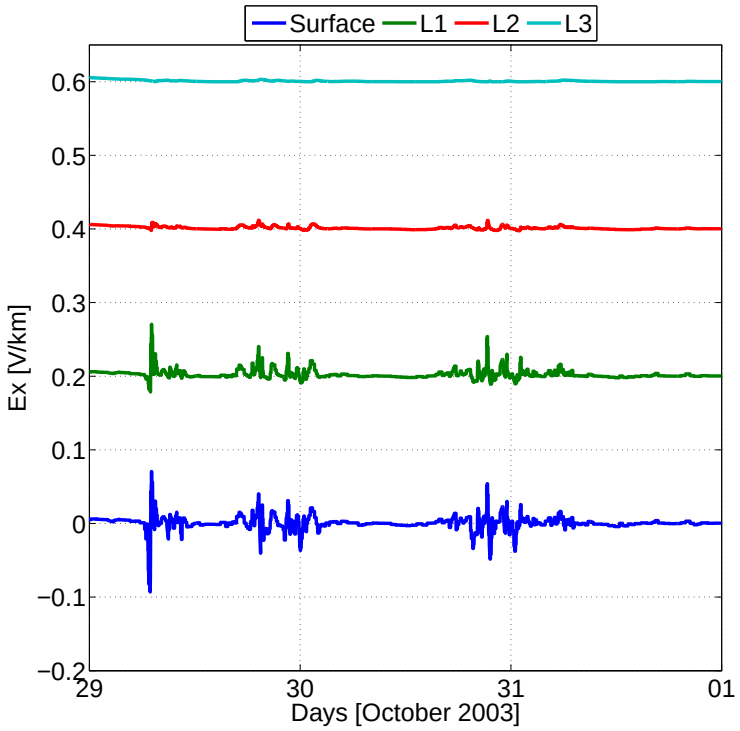

(a) E_x

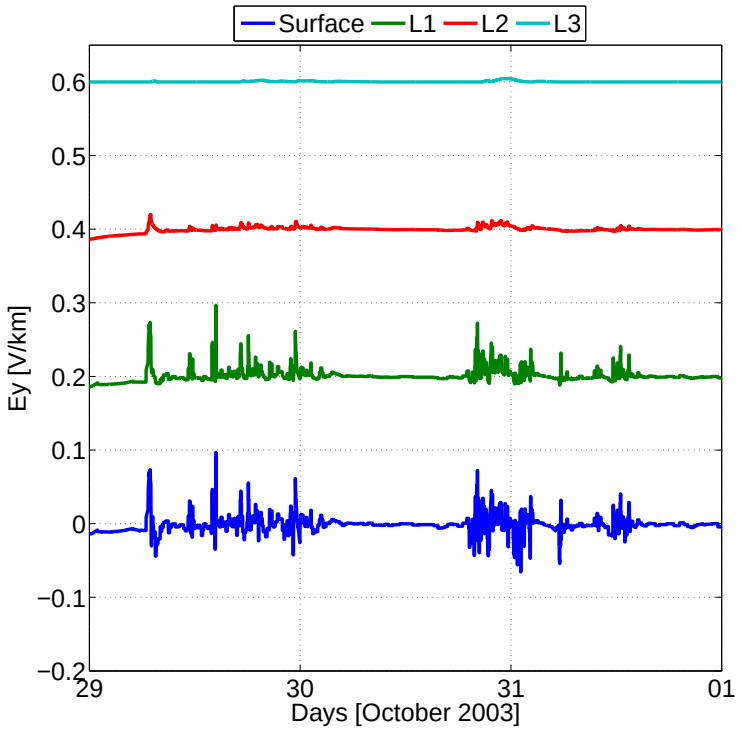

(b) E_y

Figure 6.13: The horizontal electric field components, E_x and E_y, computed for the surface and the 3 layers calculated using INT data. L1's electric field is centered at 0.2 V/km, L2 at 0.4 V/km and L3 at 0.6 V/km.

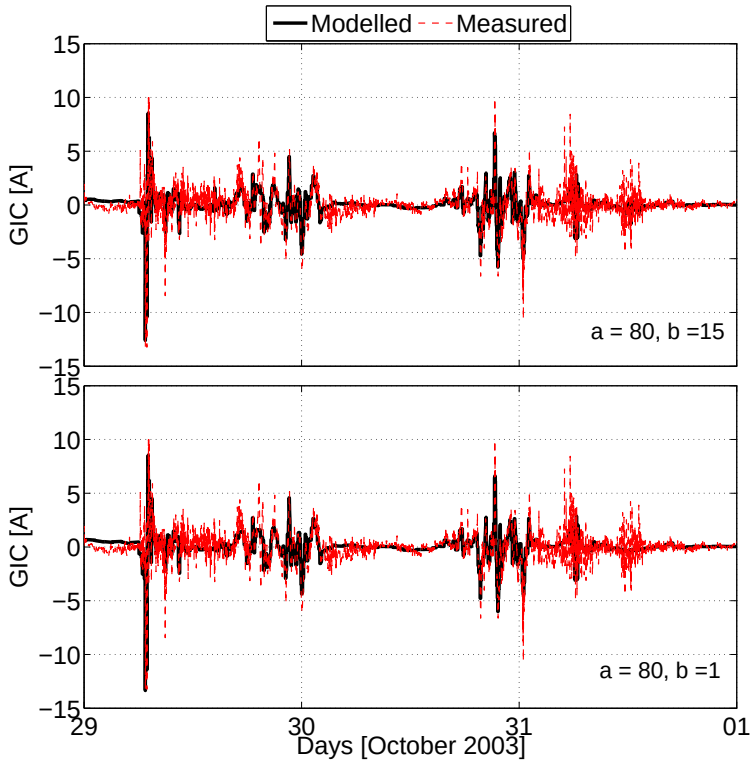

Figure 6.14: Measured and modelled GIC using HER data for Case 3 conductivity profile.

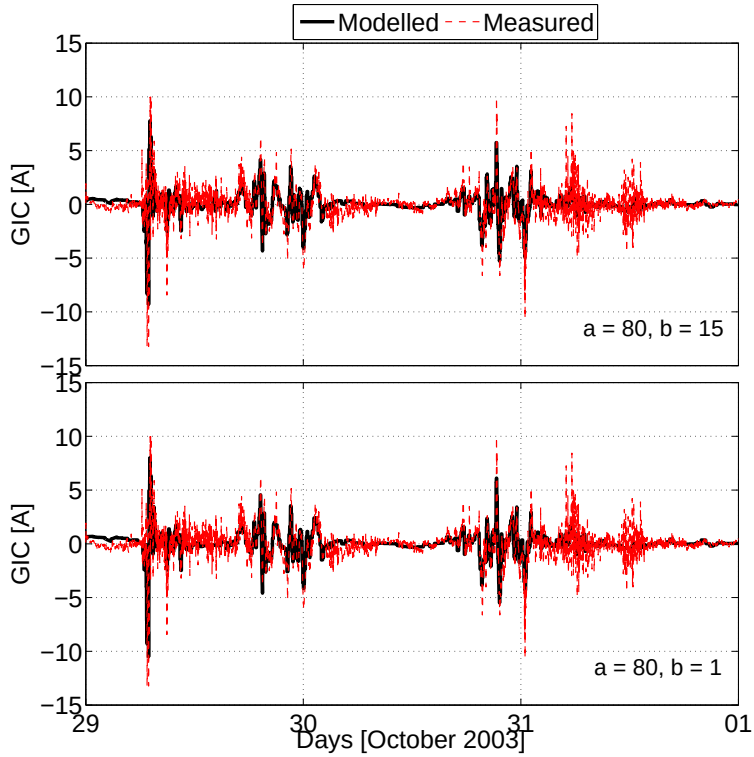

Figure 6.15: Measured and modelled GIC using INT data for Case 3 conductivity profile.

Table 6.3: Performance analysis for the FEM model using HER and Interpolated data sets: Case 3.

	ΔI [A]	RMSE	R [%]	Max I [A]	RMSE	R[%]
	$a = 80, b = 1$			$a = 80, b = 15$		
	29-31 October 2003					
HER	0.02	1.04	70	0.60	1.05	69
INT	2.69	1.0	73	3.88	1.02	72
	29 October 2003					
HER	0.02	1.20	72	0.60	1.18	73
INT	2.69	1.14	75	3.88	1.15	74
	30 October 2003					
HER	3.49	0.69	87	3.23	0.73	86
INT	3.83	0.72	87	4.15	0.77	84
	31 October 2003					
HER	5.62	0.97	60	6.68	0.97	59
INT	6.63	1.00	58	6.15	0.99	56

The average of the correlation coefficient for the three consecutive days is 72 %, where the average is determined over the two sets of a and b coefficients and two sets of data, i.e. HER and INT. For 29 October, HER data underestimates the peak GIC by between 0.02 A and 0.6 A while INT data underestimates the peak GIC by between 2.69 A and 3.88 A, with an average correlation coefficient of 73 %. This average is determined over the two sets of a and b coefficients and two sets of data, i.e. HER and INT. Like in Cases 1 and 2, lower RMSE values and higher coefficient correlation values are obtained for 30 October. For 31 October the peak GIC are poorly estimated (<34 % of the measured GIC) for both HER and INT data.

The infinite layer is relatively highly conducting, compared to the top layer in this configuration. The difference between Cases 2 and 3 can be described in terms of the depth of the highly conducting layer underlying a poorly conducting layer. The introduction of the infinite layer did not have a significant bearing on the modelled GIC; it can be concluded that the top poorly conducting layer is preferred by the GIC driving electric field. The depth of the underlying conducting layer will not influence the electric field, but the magnitude of the electric field will be enhanced if the depth of the poorly conducting layer increases.

6.4 Current density and Electric field variation

Understanding the current density distribution and the electric field variation within the different layers of the Earth can contribute to the understanding of the layers that should be considered for adequate GIC modelling. Furthermore, this will give a view of the distribution of currents during different storm conditions. In this study the use of FEM provides the advantage of being able to display the depth distribution of the current density during different storm conditions.

From the model performance analysis, the results obtained for 29 October are very similar when either HER or INT data sets are used. For this reason, it is assumed that either of the data sets will give a similar current density distribution for a selected time period. For the three cases considered in the study, current density distributions are shown for a period of low geomagnetic activity (at 02:30 UT) and high geomagnetic activity (at 06:45 UT) on 29 October 2003. These times were selected based on the rate of change of the magnetic field; 02:30 UT falls within periods of the lowest rate of change of the magnetic field, while 06:45 UT falls within periods of higher rate of change of the magnetic field. For the results shown, INT data were used.

Figure 6.16 and Figure 6.17 illustrate the current density distribution at 02:30 UT for Cases 1, 2 and 3 due to the B_y and B_x components of the INT data, respectively. Figure 6.18 and Figure 6.19 illustrate the distribution of the current density at 06:45 UT for Cases 1, 2 and 3 due to the B_y and B_x components of the INT data, respectively. The variations of the electric field with depth for each conductivity profile configuration at the selected times are shown in Figure 6.20.

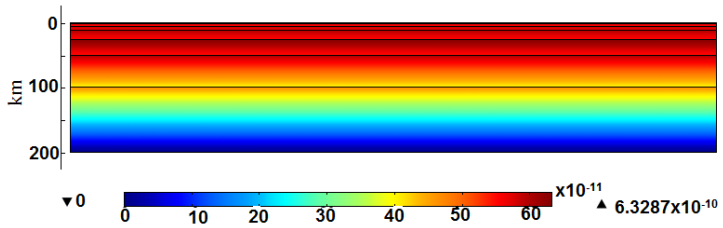

(a) Case 1

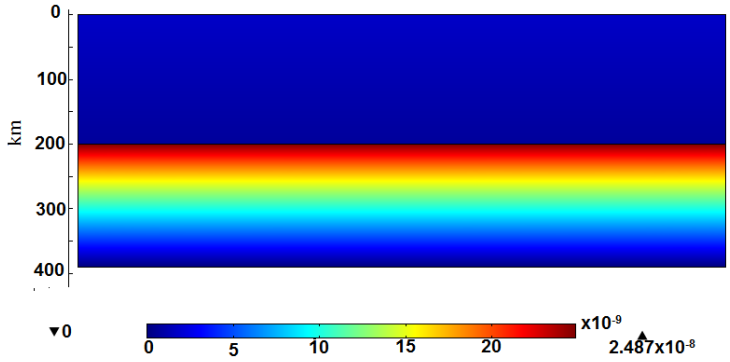

(b) Case 2

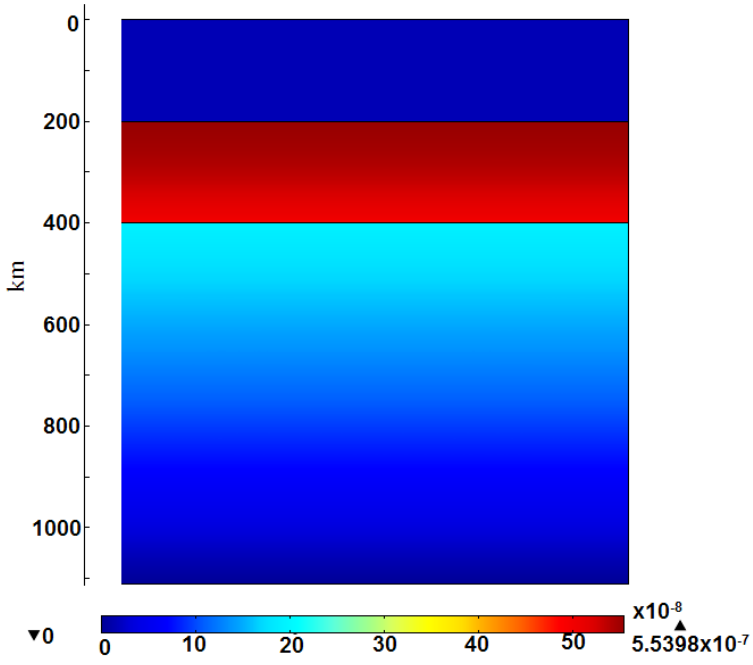

(c) Case 3

Figure 6.16: Current density in A/m^2 for the 3 cases during a typical low geomagnetic activity period due to the B_x component.

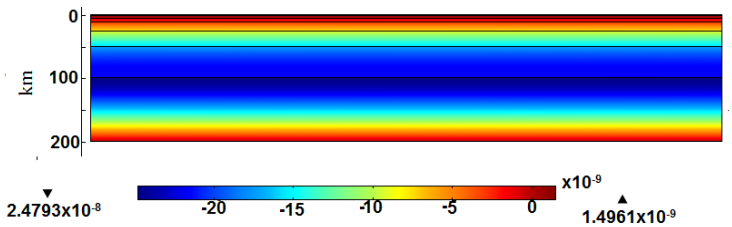

(a) Case 1

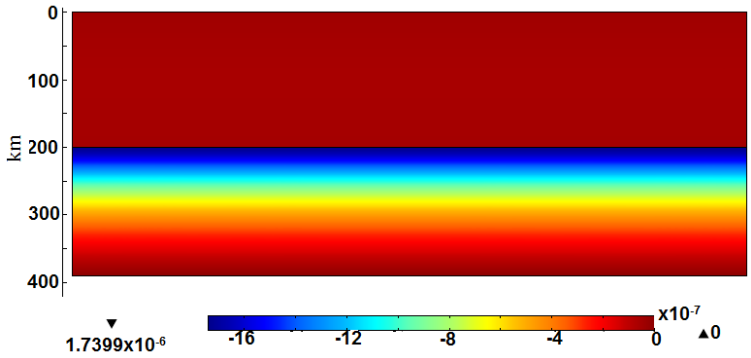

(b) Case 2

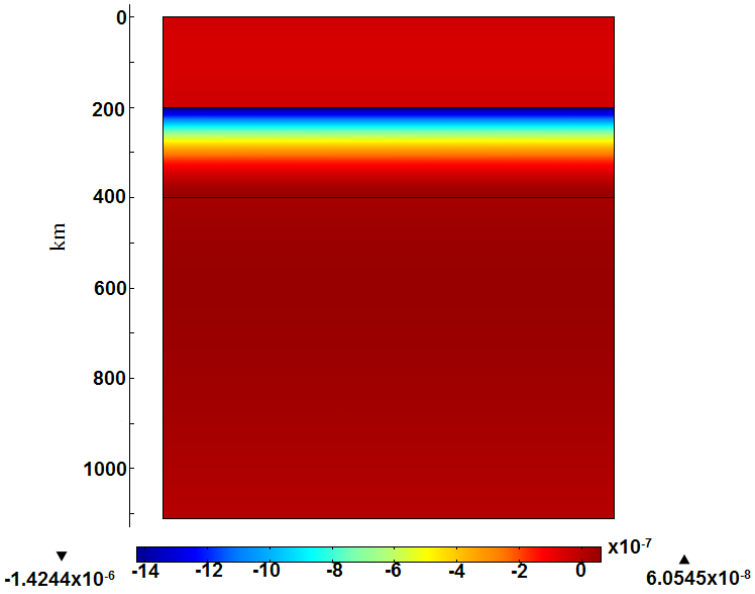

(c) Case 3

Figure 6.17: Current density in A/m^2 for the 3 cases during a typical high geomagnetic activity period due to the B_x component.

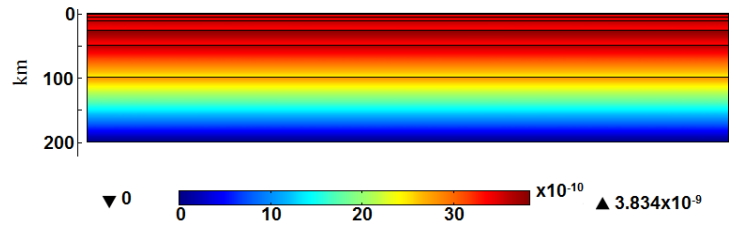

(a) Case 1

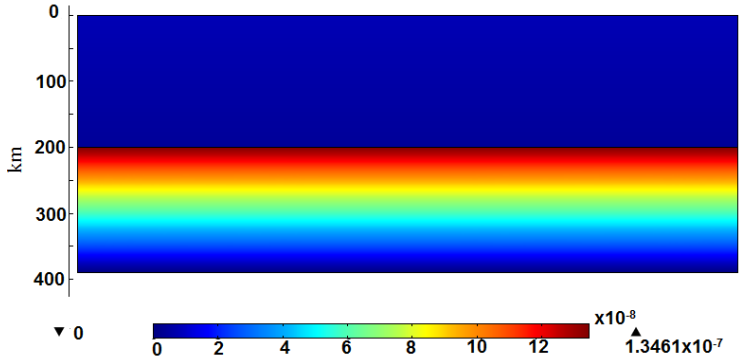

(b) Case 2

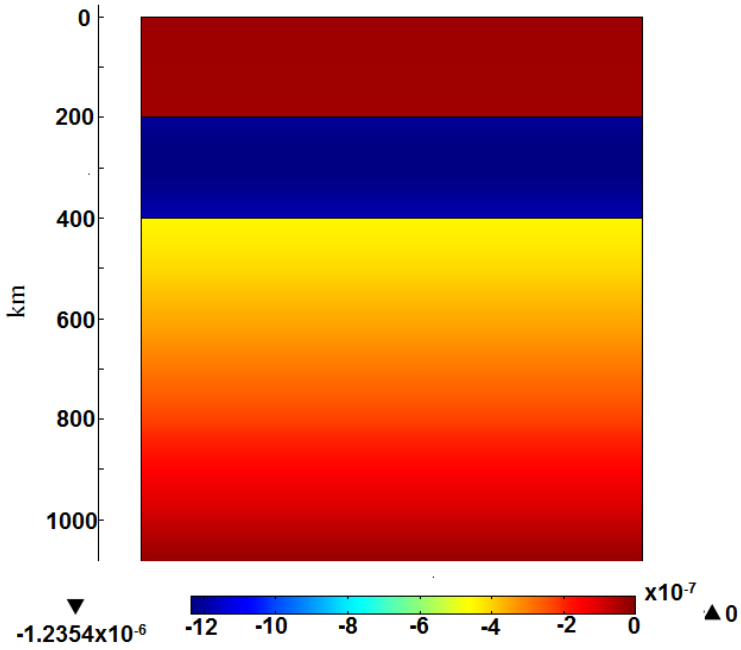

(c) Case 3

Figure 6.18: Current density in A/m^2 for the 3 cases during a typical low geomagnetic activity period due to the B_x component.

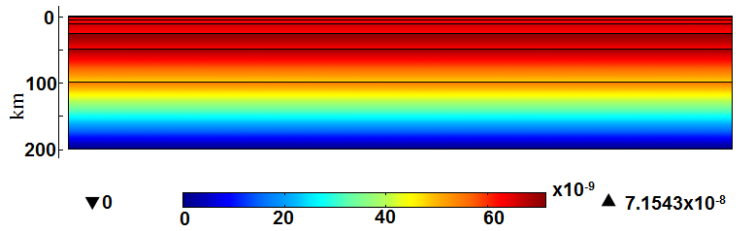

(a) Case 1

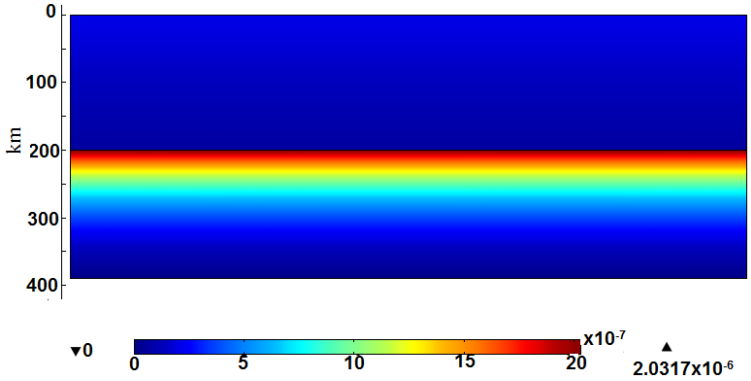

(b) Case 2

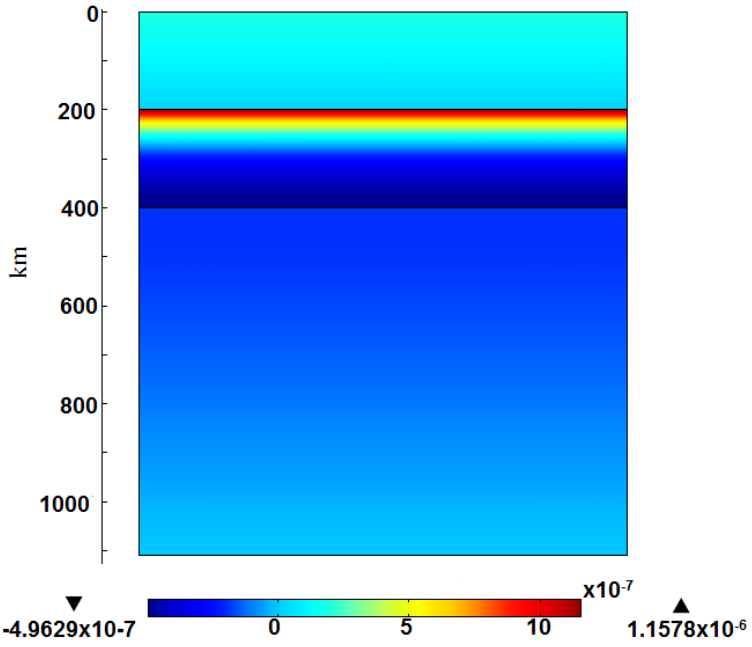

(c) Case 3

Figure 6.19: Current density in A/m^2 for the 3 cases during a typical high geomagnetic activity period due to the B_x component.

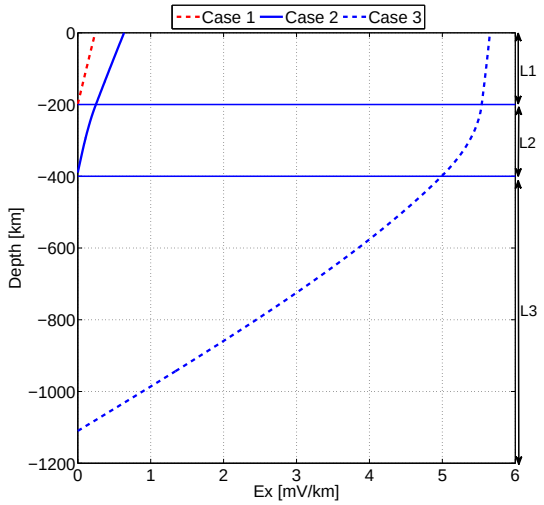

(a) E_x during low geomagnetic activity

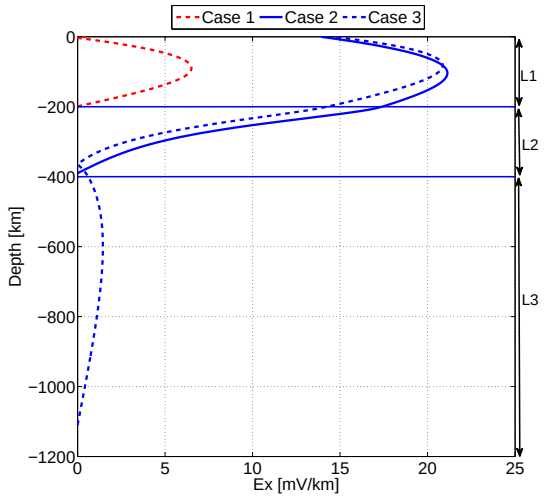

(b) E_x during high geomagnetic activity

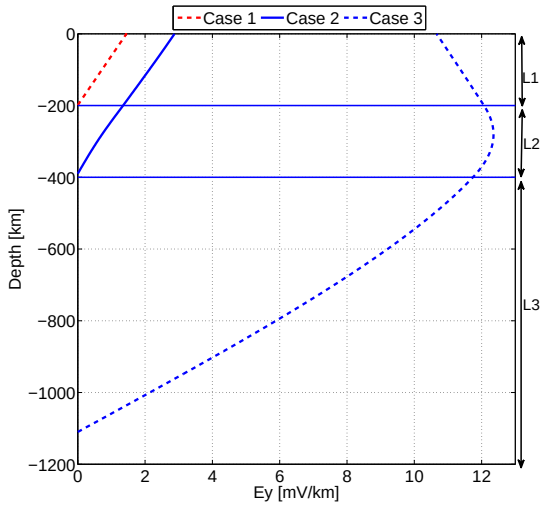

(c) E_y during low geomagnetic activity

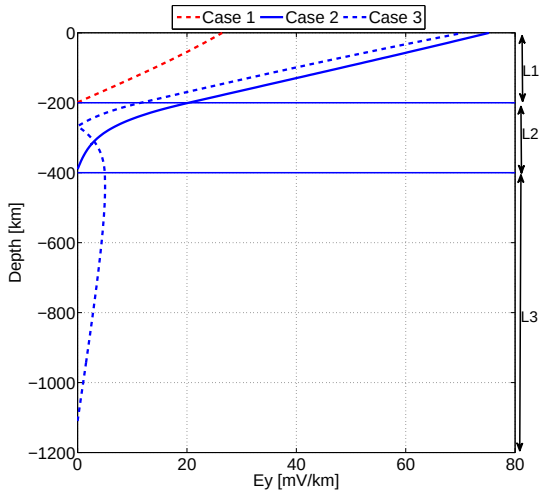

(d) E_y during high geomagnetic activity

Figure 6.20: Electric field variation with depth for the Case 1, 2 and 3 conductivity profile configurations during low and high geomagnetic activity.

From the current density it is shown that the currents have high densities in the conductive regions. This is because the currents will prefer a less resistive medium.

During low geomagnetic activity the magnitude of the electric field in the three conductivity profiles tend to increase with the height of the model. Higher magnitudes of electric fields are observed for Case 3 than for Case 2 and Case 1. However, the magnitude distinction is not the same during a high geomagnetic activity. Comparatively low electric field magnitudes are observed for Case 1. Cases 2 and 3 show the same pattern of electric field variation with depth in the two common layers with a difference of 2 mV/km for E_y and 5 mV/km for E_x. The observed results may be due to the fact that the dominant frequencies in the magnetic field during low geomagnetic activity are lower than during a high geomagnetic activity. Low frequencies imply a

small angular frequency and, thus, a large skin depth. If the bottom layers are highly conductive compared to the top layer, the top layer will not have much influence on the electric field on the surface (Pirjola, 2010). The resemblance in the electric field pattern for Cases 2 and 3 is due to the fact that the high frequencies of the magnetic field during high geomagnetic activity result in a lower skin depth. Thus, the incident wave will be more attenuated closer to the surface, compared to when the frequencies are lower.

In Appendix A, a frequency spectrogram of the magnetic field measured at HER during the Halloween storm is shown. Typical skin depth values are calculated to illustrate the concepts discussed in this section. Appendix B shows the current and current density distributions with depth for the three cases considered at the selected times. It is observed that 95 % of the total current flows above the 200 km depth.

6.5 Discussion of results

The relative errors obtained in the modelled GIC using both INT and HER data sets with either the Ngwira or Koen network coefficients differ by a maximum of 0.06 A. This can be regarded as a small difference. The same pattern is observed in the correlation coefficient where the differences are less than 5 %. There are two factors that can be pointed out from this observation. GIC are related to the rate of change of the magnetic field, and although the magnitude of the INT data is larger than the HER data, the rates of change have magnitudes that are close together as illustrated in Figure 6.21. The other explanation for this result is the fact that the direction of the power lines terminating at Grassridge is predominantly North-South so that the contribution of the E_y to the GIC was low, hence, varying the b parameter would not make a significant difference in the modelled GIC.

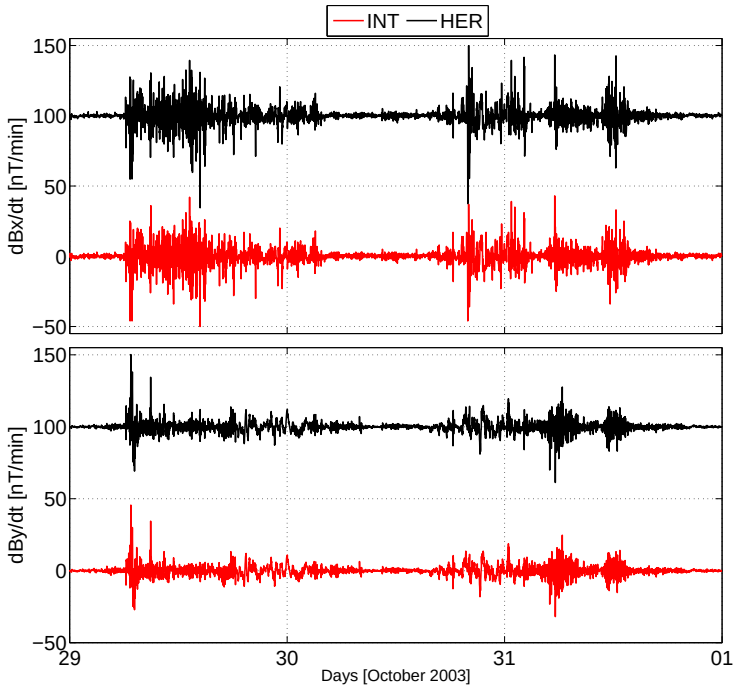

Figure 6.21: The rate of change of the horizontal components of both HER and INT data.

From the conductivity structure variation investigation, the Case 2 configuration has modelled results better than the other cases considered. This conclusion is based on its ability to model the GIC throughout the storm period with less RMSE and higher correlation coefficients. Furthermore, this is the configuration which best estimated the peak GIC for 31 October. The results from Case 3 are close to those of Case 2 for 29 and 30 October. The inclusion of the infinite layer makes the FEM model larger, i.e. more memory and more time are required for the computation. Since the addition of the infinite layer does not improve the Case 2 results, it could be excluded from the FEM modelling of the GIC for the particular storm considered.

6.6 Conclusion

This chapter presented a statistical analysis of the relationship between modelled and measured GIC. The electric field was calculated by means of FEM. The comparison is made in terms of the difference between the peak modelled and peak measured GIC, the root-mean-square error and the correlation coefficient between the modelled and measured GIC. The current density distribution and electric field variation for typically low and high geomagnetic activity conditions were also presented. Possible explanations for the observed results were discussed.

CHAPTER 7: CONCLUSION AND RECOMMENDATIONS

The current study focuses on the Southern African region where transformer damage due to GIC has been identified. The monitoring and modelling of GIC are ongoing processes in order to understand and assess the risk of the power grid being affected by GIC during adverse space weather events. There are only a few locations where GIC are measured in Southern Africa. This has led to the dependence on observatory data to model GIC for some substations. There are only four magnetic observatories in the Southern African region. The dependence on observatory data has been identified as a limitation in GIC modelling for the whole region. The accuracy of GIC models reduce as the distance between the observatory and substation increases. A GIC measurement technique and GIC modelling technique that could be adopted in Southern Africa to increase the number of GIC measurements, as well as improve GIC modelling, were presented. These two techniques can improve the assessment of the vulnerability of the Southern African power grid to GIC during adverse space weather events.

The two objectives of the study were (a) to estimate the geomagnetically induced currents flowing in a power line using magnetic field measurements in the vicinity of the power line and (b) to use the finite element method to compute the electric field associated with GIC modelling. This chapter summarises the findings of the current study and highlights possible areas that can be improved to enhance understanding of the characteristics of GIC in the mid-latitude region. The overall conclusion reached, based on the findings of this study, is that the measurement of GIC using the differential magnetometer method and modelling GIC using the FEM method are useful tools in understanding the characteristics of GIC and both can be used to complement the GIC measurement done at the neutral-ground-connection of the transformer neutrals. Both methods can provide necessary information to the power utilities so that the impact of GIC on the Southern African power grid can be better assessed and managed.

7.1 Summary

7.1.1 GIC measurement with the differential magnetometer method

The first differential magnetometer method (DMM) measurements of GIC in Southern Africa were carried out in Namibia near the Obib substation. Data for only 6 days data were available for analysis from this measurement opportunity. A temporary magneto-telluric setup was used to perform the DMM observation and the period of measurement had low geomagnetic activity. The magnetic sensor axes were aligned such that the y-axis of the magnetometer would measure the magnetic field perpendicular to the power line. The GIC estimated using the DMM observations were compared with GIC modelled with the Nodal Admittance Matrix Method and the GIC calculated by using the network parameters and the electric field measured 200 m away from the power line. The magnetic field measured 200 m away and at the Tsumeb (TSU) Magnetic Observatory were used as references in DMM. Correlation coefficients $> 60\%$ between the GIC calculated using three different methods were achieved. This is taken as evidence of common

features of the GIC characteristics shown by the different methods.

The second identified DMM site was near Botriver in South Africa. Measurements done from 17 to 21 March 2015 during an active geomagnetic storm period were discussed. The LEMI-011 magnetometer was used for these measurements. The magnetic field measured 70 m away from and directly under the power line were measured with the x-axis of the magnetometer aligned to Magnetic North. The horizontal components of the measured magnetic field were transformed to the power line coordinate system to allow the subtraction of the horizontal magnetic field (under the power line and the reference) components in the same coordinate system. This was achieved by rotating the coordinate system of the measured field through the declination angle as well as the power line bearing. The magnetic field measured 70 m away from the power line and at Hermanus (HER) Magnetic Observatory were both used to provide the background field. After scaling down the 10-second sampled magnetic field measurements to 5-minute averages, the DMM calculated GIC and the GIC measured at the neutral to ground connection of the transformer at the Bacchus station were compared. A 52 % correlation coefficient was obtained.

The DMM observation from both the Obib and Botriver sites indicated that the magnetic field perpendicular to the power line would be characterised by a noisy signal. The selected LEMI-011 magnetometers are suitable for the DMM observation as they have demonstrated the ability to detect the slight fluctuations in the magnetic field due to GIC and also the ability to suppress the magnetic field of the 50 Hz current flowing in the power line. The DMM observations can be a useful tool in the measurement of GIC, which can complement the GIC measurements done at the neutral to ground connection of the transformers.

The GIC values calculated for both sites identified are not indicative of the extremes of GIC that can occur in the Southern African power network. In both incidences, the calculated GIC and the measured GIC are less than 3 A. These values may be considered as of no immediate threat to the transformers, but continuous exposure to these GIC levels may contribute to cumulative effects.

7.1.2 Modelling GIC with Finite Element Method

The AC/DC module of the COMSOL Multiphysics finite element simulation software was used to calculate the electric field associated with geomagnetically induced currents. Measured magnetic field data and a 1D conductivity profile were used as model input. The Grassridge substation was used for the case study. Two magnetic field data sets were used: Magnetic field measured at HER and the magnetic field interpolated to the location of the Grassridge substation based on the magnetic field measured at HBK and HER. To evaluate the FEM model, the electric field calculated with FEM was used to calculate GIC, which were then compared to the GIC measured at the Grassridge substation during the October 2003 storm. Two sets of network parameters, derived by Koen (2002) (a = -80 Akm/V; b = 15 Akm/V) and Ngwira *et al.* (2008) (a = - 80 Akm/V; b=1 Akm/V) for the substation were used to calculate the GIC.

The electric field was calculated for three different conductivity profile configurations. These configurations were based on the original conductivity profile derived by Ngwira *et al.* (2008). The first configuration (Case 1) consists of 7 layers of the 9-layer Ngwira model. The second profile configuration (Case 2) consists of an average of Case 1 as the first layer and the second layer is the 8th layer of the Ngwira model. The third profile (Case 3) adds an infinite half- space below the two layers of Case 2. Information, such as the current density distribution with depth, as well as the variation of the electric field with depth could be extracted. The FEM model gives insight into three aspects of the GIC modelling, with focus on the Grassridge case:

- Which of the two sets of the network coefficients best models the Grassridge GIC.
- Which magnetic field data is best for modelling GIC for the Grassridge substation.
- Which of the three conductivity profile configurations gives the best match to the GIC derived from the electric field calculated using the FEM model.
- In which layers does most of the Earth's current flow.

The use of measured magnetic field as input for FEM modelling was different from the study presented by Dong *et al.* (2013) , where both magnetic field and electric field were calculated from an infinite line source using FEM. The measured input data used, allows the FEM model performance to be compared with results obtained from previous models, such as reported by Koen (2002), Bernhardi *et al.* (2008) and Ngwira *et al.* (2008) for the same and for the same period discussed.

Of the three conductivity profile configurations, the input magnetic field data and the network coefficients, Case 2 and HER data modelled the GIC better than the other combinations, however, the results for 29 October were an exception. On that particular day INT data best modelled the GIC with Δ I values of less than 1 A (0.5 A when using the Koen coefficients and 0.8 A when using the Ngwira coefficients). If focus is put on the GIC results of the 29^{th} of October as per the study by Ngwira *et al.* (2008), it can be observed that the FEM model is an improvement of the Ngwira model. RMSE values obtained from the FEM model using both network coefficients were about 1A. This is less than the 3.49 A obtained by Koen and the 1.56 A obtained by Ngwira.

The current density as obtained using the 1D earth conductivity model used in FEM is not continous at the adjacent conductivity interfaces while the electric field is. The current density distribution and the electric field variation with depth show that more than 95 % of the total current will flow above the 200 km depth. A conclusion that the FEM models the GIC better if the earth is considered to be one with a top poorly conducting layer resting on a highly conducting layer. The GIC driving electric field is therefore, not influenced by the depth of the conducting layer but as the depth of the conducting layer increases, so does the enhancement of the electric field. To save memory and computation time, the GIC could thus be simulated adequately in FEM without the infinite layer.

The correlation between the GIC values obtained using direct measurements , DMM and FEM agree upto 70 % on the average. This confirms that the DMM and FEM are complementary. Thus FEM is a promising tool for modelling and may be suited for now casting of GIC in power networks.

7.2 Recommendations

Two tools that could enhance the assessment of GIC through measurement and modelling in the Southern African region are discussed. By implementing these tools the data coverage may be increased. Where GIC cannot be measured, the FEM models can be implemented. The measurement of GIC by DMM will increase the number of GIC measurement points; thus, assisting in the assessment of the vulnerability of the Southern African network to GIC. The system designed in the study is portable and affordable. However, some technical aspects can be implemented to improve the system. The recommendations listed below are related to the DMM measurement technique:

- The wooden boxes used as enclosure for the DMM measurement system can be affected by moisture, especially in the rainy season. It is therefore recommended that wooden boxes are replaced with larger plastic or non-magnetic containers.
- The 8 Ah battery must be recharged every 2 months. During replacement of the batteries the orientation of the magnetometers may be disturbed. A longer lasting battery should be used. For sites that are endorsed to be permanent, solar panels can be used to charge the batteries if the sites are secure enough to avoid theft of the solar panels.
- The current measurement system requires data to be downloaded manually after a certain period of time. A more flexible data acquisition system, such as wireless transfer, would be useful. This would help to detect problems at the site, such as low battery power and could be rectified with minimal data loss.

With regards to FEM modelling, it has been demonstrated that the measured magnetic field and a layered Earth model can be used to model the GIC for a selected substation. The derivation of conductivity profiles for other locations in Southern Africa will allow extension of this work to other substations. Although only the 1D profile was tested, with adequate computational power complex conductivity profiles in 2D and 3D can be used as model inputs. Expansion to a 3D model will allow the determination of the variation of the direction of the currents within the Earth layers.

7.3 Future work

The modelling of GIC in the Southern African power grid has been limited by the availability of quality GIC data model validation (Ngwira *et al.*, 2009). The DMM observation presented in the current study has proved to be an affordable and reliable method of inferring the characteristics of GIC in the power lines. The system used for the South African measurement is easy to duplicate and maintain but requires some improvements in power supply. In future, more secure and suitable sites could be identified for DMM observations, so that more GIC data of acceptable

integrity can be acquired for analysis.

The FEM has the advantage of solving problems with a complex geometry. Some substations are located in areas that may be affected by the interface of the coastal geological structure (highly conductive) and inland geological structure (highly resistive). Realistic conductivity profiles for different coastal and inland regions need to be derived so that the FEM can be used to model GIC for the substations situated along those regions. For this to be achieved, long term magnetic field measurement data available in the region can be identified and used for the derivation of conductivity maps.

References

Albertson, V., Kappenman, J., Mohan, N. and Skarbakka, G. 1981. Load-flow studies in the presence of geomagnetically induced currents. *Power Apparatus and Systems, IEEE Transactions on*, (2): 594–607.

Bathe, K. J. 1982. *Finite element procedures in engineering analysis.* Prentice Hall, Inc.

Beamish, D., Clark, T. D. G., Clarke, E. and Thomson, A. W. P. 2002. Geomagnetically induced currents in the UK: geomagnetic variations and surface electric fields. *Journal of Atmospheric and Solar-Terrestrial Physics*, 64(16): 1779–1792.

Béland, J. and Small, K. 2005. *Space weather effects on power transmission systems: the cases of Hydro-Québec and Transpower New Zealand*, Dordrecht, Springer Netherlands, pp. 287–299.

Bernhardi, E. H. 2006. Modelling geomagnetically induced currents (GIC) in Southern Africa. Honours Thesis, University of Cape Town, Cape Town.

Bernhardi, E. H., Tjimbandi, T. A., Cilliers, P. J. and Gaunt, C. T. 2008. Improved calculation of geomagnetically induced currents in power networks in low-latitude regions., *in* 'Power System Computation Conference, Scotland.'.

Bolduc, L. 2002. GIC observation and studies in the Hydro-Quebec power system. *Journal of Atmospheric and Solar-Terrestrial Physics*, 64(16): 1793–1802.

Boteler, D. 2014. Methodology for simulation of geomagnetically induced currents in power systems. *Journal of Space Weather and Space Climate*, 4: A21.

Boteler, D. H. and Pirjola, R. 1998*a*. Modelling geomagnetically induced currents produced by realistic and uniform electric fields. *IEEE, Transactions on Power Delivery*, 13(4): 1303–1308.

Boteler, D. H., Pirjola, R. and Nevanlinna, H. 1998. The effects of Geomagnetic disturbances on electrical systems at the Earth's surface. *Advances in Space Research*, 22(1): 17–27.

Boteler, D. and Pirjola, R. 1998*b*. The complex-image method for calculating the magnetic and electric fields produced at the surface of the Earth by the auroral electrojet. *Geophysical Journal International*, 132(1): 31–40.

Boteler, D. and Pirjola, R. 2014. Comparison of methods for modelling geomagnetically induced currents., *in* 'Annales Geophysicae', Vol. 32, Copernicus GmbH, pp. 1177–1187.

Campbell, W. H. 1978. Induction of auroral zone electric currents within the Alaska pipeline. *Pure and Applied Geophysics*, 116(6): 1143–1173.
URL: *http://dx.doi.org/10.1007/BF00874677*

Campbell, W. H. 1980. Observation of electric currents in the Alaska oil pipeline resulting from auroral electrojet current sources. *Geophysical Journal of the Royal Astronomical Society*, 61(2): 437–449.

Campbell, W. H. 2001. *Earth Magnetism.* Harcourt Academic Press.

Campbell, W. H. and Zimmerman, J. E. 1980. Induced electric currents in the Alaska Oil Pipeline measured by gradient fluxgate and squid magnetometers. *IEEE, Transactions on Geoscience and Remote Sensing*, 18(3): 244–250.

Cargniard, L. 1953. Basic theory of the magneto-telluric method of geophysical prospecting. *Geophysics*, 18(3): 605–635.

Chave, A. D. and Jones, A. G. 2012. *The magnetotelluric method: Theory and Practice.* Cambridge University Press.

Chung, T. J. 2010. *Computational Fluid dynamics.* 2nd edn, Cambridge University Press.

COMSOL 2012. 'Introduction to AC/DC Module.', [Online], www.comsol.com, U. S. [Accessed: 27 August 2014].

Dixit, U. S. n.d. Finite element method:An introduction. [Online], http://www.iitg.ernet.in/scifac/qip/public_html/cd_cell/cdc_06_07.htm. [Accessed: 04 August 2015].

Dommel, H. W. 1986. *Electromagnetic transients program (EMTP) theory book.* Bonneville Power Administration.

Dong, B., Danskin, D. W., Pirjola, R. J., Boteler, D. H. and Wang, Z. Z. 2013. Evaluating the applicability of the finite element method for modelling of geoelectric fields. *Annales Geophysicae*, 31(10): 1689–1698.

Forslund, Å., Belyayev, S., Ivchenko, N., Olsson, G., Edberg, T. and Marusenkov, A. 2008. Miniaturized digital fluxgate magnetometer for small spacecraft applications. *Measurement Science and Technology*, 19(1): 015202.

Frei, W. 2014. Exploiting symmetry to simplify magnetic field modeling. [Online], http://www.comsol.com. [Accessed: 26 November 2014].

Gaunt, C. T. and Coetzee, G. 2007. Transformer failures in regions incorrectly considered to have low GIC risk., *in* '2007 IEEE Power Tech , Lausanne, Switzerland'.

Girgis, R., Vedante, K. and Gramm, K. 2012. Effects of geomagnetically induced currents on power transformers and power systems., Cigre 2012, Paris.

Gummow, R. A. and Eng, P. 2002. GIC effects on pipeline corrosion and corrosion control system. *Journal of Atmospheric and Solar-Terrestrial Physics*, 64(16): 1755–1764.

Hapgood, M. and Rees, J. 2014. UK space weather strategy-linking research to operations (Draft 10).

Hermance, J. and Peltier, W. R. 1970. Magnetotelluric fields of a line current. *Journal of Geophysical Research*, 75(17): 3351–3356.

Hollauer, C. 2007. Modeling of thermal oxidation and stress effects. PhD thesis, Technischen Universität Wien (Vienna University of Technology), Vienna, Austria.

Humphries, S. J. 2010. *Finite element methods for electromagnetics.* U.S.A, Albuquerque.

Hutton, D. V. 2004. *Fundamentals of Finite element analysis.* USA, Mc Graw-Hill.

Kamide, Y. 2001. Geomagnetic storms as a dominant component of space weather: Classic picture and recent issues., *in* 'Space storms and space weather hazards', Springer, pp. 43–77.

Koen, J. 2000. Geomagnetically Induced Currents and its Presence in the Eskom Transmission Network. Master's thesis, University of Cape Town, Cape Town, South Africa.

Koen, J. 2002. Geomagnetically Induced Currents in the Southern African Transmission Network. PhD thesis, University of Cape Town, Cape Town, South Africa.

Koskinen, H., Transknen, E., Pirjola, R., Pulkkinen, A., Dyer, C., Rodgers, D., Cannon, P., Mandeville, J., Boscher, D. and Hilgers, A. 2001. *Space weather effects catalogue.* Vol. 2, Finnish Meterological Institute.

Lang, K. R. 2009. *The Sun from Space.* 2nd edn, U.S.A, Spinger.

Lehtinen, M. and Pirjola, R. 1985. Currents produced in the earthed conductor by geomagnetically induced electric fields. *Annales Geophysicae*, 31(4): 479–484.

LEMI 2011. LEMI-417M Long-period magnetotelluric station., Technical report. [Accessed: 21 August 2014].

Liu, C. M., Liu, L. G., Pirjola, R. J. and Wang, Z. Z. 2009. Calculation of geomagnetically induced currents in mid- to low-latitude power grids based on the plane wave method: A preliminary case study. *Space Weather*, 7(4). doi:10.1029/2008SW000439.

Mäkinen, T. 1993. *Geomagnetically induced currents in the Finnish power transmission system.* Number 32, Helniski, Finland, Finnish Meteorological Institute, Geophysical Publications.

Marshall, R. A., Smith, E. A., Francis, M. J., Waters, C. L. and Sciffer, M. D. 2011. A preliminary risk assessment of the Australian region power network to space weather. *Space Weather*, 9(10).

Marti, L., Yiu, C., Rezaei-Zare, A. and Boteler, D. 2014. Simulation of geomagnetically induced currents with piecewise layered-earth models. *Power Delivery, IEEE Transactions on*, 29(4): 1886–1893.

Matandirotya, E., Van-Zyl, R. R., Gouws, D. J. and Saunderson, E. F. 2013. Evaluation of a Commercial-Off-the-Shelf Fluxgate magnetometer for Cube Sat space magnetometry. *Journal of Small Satellites*, 2(1): 133–146.

Moldwin, M. 2008. *An Introduction to Space Weather.* USA, Cambridge University Press.

Molinski, T. S. 2002. Why utilities respect geomagnetically induced currents. *Astrophysics and Solar Terrestial Physics*, 64(16): 1765–1778.

MrReid.Org. 2011. Solar wind and real wind. [Online], http://wordpress.mrreid.org. [Accessed: 1 September 2014].

NASA/MSFC 2010. The birth of a Coronal mass ejection. [Online], http://www.nasa.gov/mission_pages/hinode/solar_005.html. [Accessed: 1 September 2014].

Ngwira, C. M., McKinnell, L. A., Cilliers, P. J., Viljanen, A. and Pirjola, R. 2009. Limitations of the modeling of the geomagnetically induced currents in the South African power network. *Space Weather*, 7(10). DOI: 10.1029/2009SW000478.

Ngwira, C. M., Pulkkinen, A., McKinnell, L. A. and Cilliers, P. J. 2008. Improved modelling of geomagnetically induced currents in the South African power networks. *Space Weather*, 6(11). DOI: 10.1029/2008SW000408.

NRF/HMO 2009. Magnetic Results 2009:Hermanus, Hartebeesthoek and Keetmanshoop observatories., Technical report. [Online], http://www.intermagnet.org/yearbooks/SouthAfrica_2009.pdf [Accessed: 16 September 2015].

Pirjola, R. 2000. Geomagnetically induced currents during magnetic storms. *IEEE, Transactions on Plasma Science.*, 28(6): 1867–1873.

Pirjola, R. 2007. Calculation of geomagnetically induced currents (GIC) in a high-voltage electric power transmission system and estimation of effects of overhead shield wires on GIC modelling. *Journal of Atmospheric and Solar-Terrestrial Physics*, 69(12): 1305–1311.

Pirjola, R. and Boteler, D. 2002. Calculation methods of the electric and magnetic fields at the Earth's surface produced by a line current. *Radio Science*, 37(3): 14.1–14.9.

Pirjola, R. J. 2010. Derivation of characteristics of the relation between geomagnetic and geoelectric variation fields from the surface impedance for a two-layer earth. *Earth, planets and space*, 62(3): 287–295.

Pirjola, R. and Viljanen, A. 1998. Complex image method for calculating electric and magnetic fields produced by an auroral electrojet of finite length. *Annales Geophysicae*, 16(11): 1434–1444.

Price, P. R. 2002. Geomagnetically Induced current effects on transformers. *Power Delivery, IEEE Transactions*, 17(4): 1002–1008.

Priest, E. R. 1995. *The Sun and its magnetohydrodynamics.* USA, Cambridge University Press.

Pulkkinen, A. 2003. Geomagnetic induction during highly disturbed space weather conditions: studies of ground effects. PhD thesis, Finish Metrological Institute, Helsinki, Finland.

Pulkkinen, A., Pirjola, R. and Viljanen, A. 2007. Determination of the ground conductivity and system parameters for optimal modeling of geomagnetically induced current flow in technological systems. *Earth Planets Space*, 59: 999–1006.

Ratcliffe, J. A. 1972. *An Introduction to the ionosphere.* Cambridge University Press.

Ripka, P. and Ripka, S. 2007. *Magnetic Sensors.*, London:ISTE, pp. 433–475.

Russell, M. J. 2000. The impact of mains impedance on power quality., *in* 'Power Quality'.

Sayas, F.-J. 2008. A gentle introduction to the Finite Element Method. [Online], artuno.imati.cnr.it/~marini/didattica/Metodi-engl/Intro2FEM.pdf [Accessed: 22 January 2017].

Shepherd, G. S. and Shubitidze, F. 2003. Method of auxiliary sources for calculating the magnetic and electric fields induced in a layered Earth. *Journal of Atmospheric and Solar-Terrestrial Physics*, 65(10): 1151–1160.

Thomson, A. W. P., McKay, A. J. and Viljanen, A. 2009. A Review of Progress in Modelling Induced Geoelectric and Geomagnetic Fields with special regard to Geomagnetically Induced Currents. *Acta Geophysica*, 57(1): 209–219.

Torta, J. M., Serrano, L., Regué, R. J., Sánchez, A. M. and Roldán, E. 2012. Geomagnetically induced currents in a power grid of northeastern Spain. *Space Weather*, 10(6). DOI: 10.1029/2012SW000793.

Trichtchenko, A., Boteler, D. and Foss, A. 2007. Gic modelling for an overdetermined system., *in* 'Electromagnetic Compatibility and Electromagnetic Ecology, 2007 7th International Symposium on', pp. 254–256.

Trivedi, N. B., Vitorello, I., W. Kabata, Padilha, A., Bologna, M. S., de Padua, M. B., A. P. Soares, G. S. Luz, de A. Pinto, F., Pirjola, R. and Viljanen, A. 2007. Geomagnetically induced currents in an electric power transmission system at low latitudes in Brazil: A case study. *Space Weather*, 5(4). DOI: 10.1029/2006SW000282.

Tsurutani, B. 2001. The interplanetary causes of magnetic storms, substorms and geomagnetic quiet., *in* I. A. Daglis, ed., 'Space Storms and Space Weather Hazards', Vol. 38 of *NATO Science Series*, Springer Netherlands, pp. 103–130.

Uchida, T., Song, Y., Lee, T. J., Mitsuhata, Y., Lim, S. and Lee, S. K. 2005. Magnetotelluric survey in an extremely noisy environment at the pohang low-enthalpy geothermal area, Korea., Proceedings World Geothermal Congress, Antlya, Turkey.

Viljanen, A. and Pirjola, R. 1989. Statistics on Geomagnetically -Induced Currents in the Finish 400kV Power System Based on recordings of geomagnetic variations. *Journal of geomagnetism and geoelectricity*, 41(4): 411–420.

Viljanen, A. and Pirjola, R. 1994. Geomagnetically induced currents in the Finnish high-voltage power system. *Surveys in Geophysics*, 15(4): 383–408.
URL: *http://dx.doi.org/10.1007/BF00665999*

Viljanen, A., Pirjola, R., Wik, M., Ádám, A., Prácser, E., Sakharov, Y. and Katkalov, J. 2012. Continental scale modelling of geomagnetically induced currents. *Journal of Space Weather and Space Climate*, 2: A17.

Viljanen, A., Pulkkinen, A., Amm, O., Pirjola, R. J., Korja, T. and BEAR Working group 2004. Fast computation of the geoelectric field using the method of elementary current systems and planar Earth models. *Annales Geophysicae*, 22(1): 101–113.

Viljanen, A. T., Pirjola, R. J., Pajunpaa, R. and Pulkkinen, A. A. 2009. Measurements of geomagnetically induced currents by using two magnetometers., *in* '8-th International Symposium on the Electromagnetic Compatibility and Electromagnetic Ecology, Saint-Petersburg,Russia', pp. 227–230. June 16-19, 2009.

Zatjirua, T. 2005. Investigation of geomagnetically induced currents in the transmission network of Namibia. Honours Thesis, University of Cape Town, Cape Town.

Zhang, J. J., Wang, C. and Tang, B. B. 2012. Modeling geomagnetically induced electric field and currents by combining a global MHD model with a local one-dimensional method. *Space Weather*, 10(5): n/a–n/a. S05005.

Zheng, K., Pirjola, R. J., Boteler, D. H. and Liu, L. 2013. Geoelectric fields due to small-scale and large-scale sources current. *Power Delivery, IEEE Transactions on*, 28(1): 442–449.

Appendices

Appendix A: FREQUENCY SPECTRUM ANALYSIS OF THE HALLOWEEN STORM MAGNETIC FIELD

A spectrogram represents the frequency spectrum of a signal. In this section, the frequency spectrum of the magnetic field measured at Hermanus on 29-31 October 2013 is presented. The aim is to display the typical frequencies that are representative of low and high geomagnetic activity. With the selected frequencies, the classical skin depth for the top layer of Cases 2 and 3 are calculated. Figures A.1 and A.2 show the rate of change of the horizontal components of the magnetic field, the maximum frequencies per time bin and spectral density distribution during the October 2003 storm period.

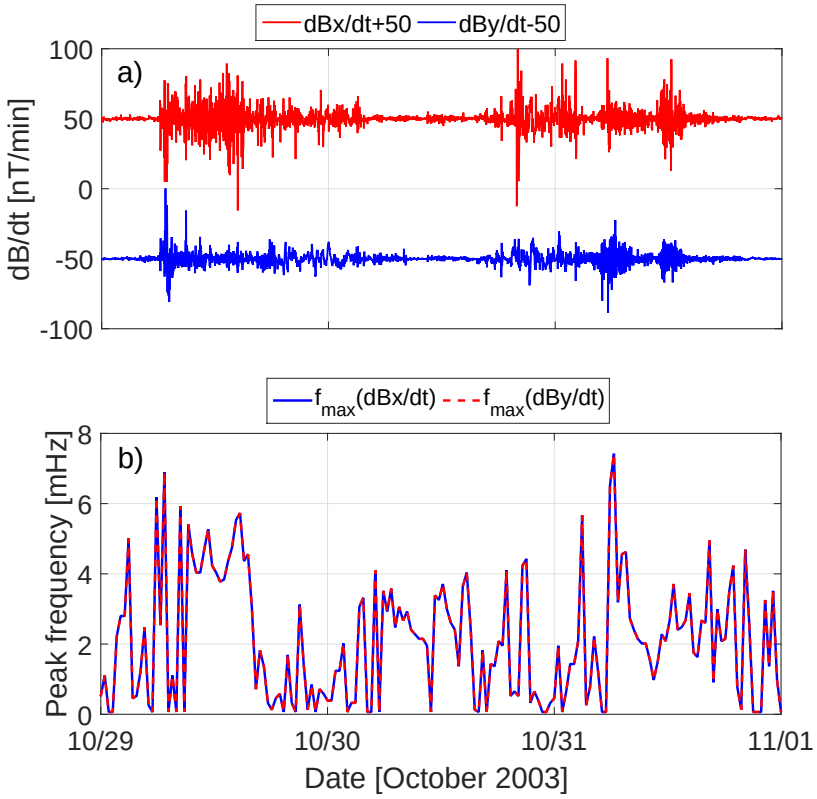

Figure A.1: The rate of change of the horizontal components of the magnetic field measured at Hermanus and the peak frequencies per time bin.

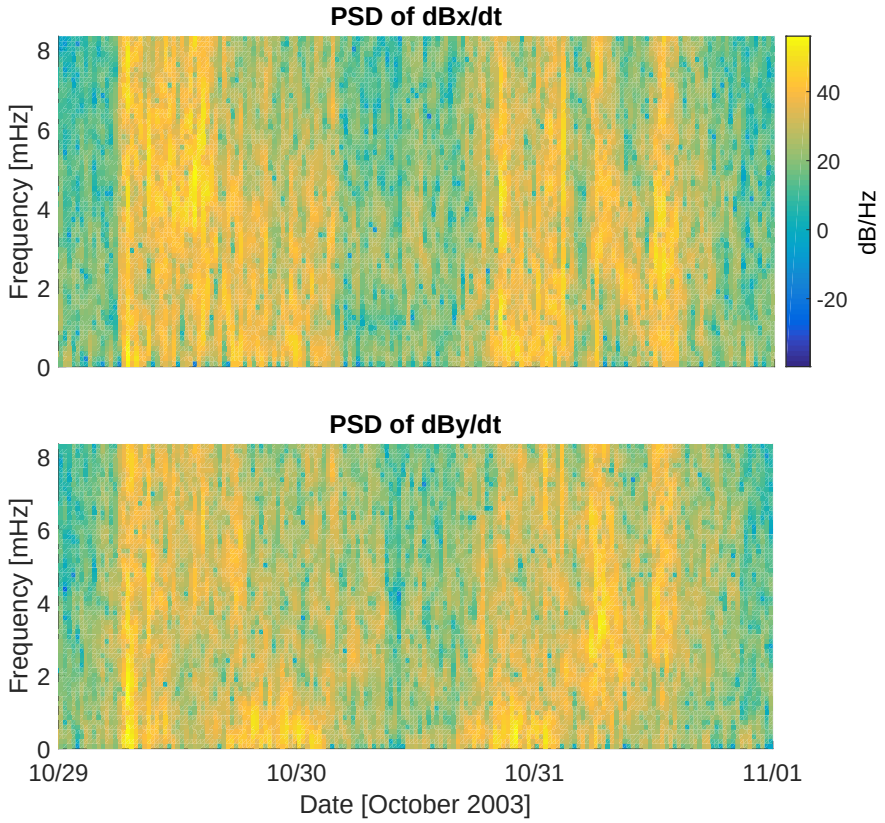

Figure A.2: Power spectral density (PSD) for the rate of change of the horizontal components of the magnetic field measured at Hermanus.

A.1 Calculating the classical skin depth

The skin depth is defined as the depth at which the amplitude of the plane-wave electric or magnetic field has decayed by a magnitude of e^{-1} from its magnitude at the surface. The skin depth for the layer $\delta_n (n = 1, 2, ..)$ is given as:

$$\delta_n = \sqrt{\frac{2}{\omega \mu_n \sigma_n}} \tag{A.1}$$

where μ_n is the permeability of the layer, ω is the angular frequency considered and σ_n is the conductivity of the layer.

If we consider the first layer in Cases 2 and 3, the resistivity of the layer is 361 Ωm. During the selected times of low geomagnetic activity (02:30 UT on the 29^{th} of October 2003) the frequency is ≈ 0.8 mHz and at high geomagnetic activity (06:45 UT 02:30 UT on the 29^{th} of October 2003) the peak frequency is ≈ 6.90 mHz. If we assume that $\mu_n = \mu_0$, the permeability of free space, the skin depth at these frequencies are:

at $f = 0.8$ mHz

$\delta_1 = \sqrt{\frac{2}{(1/361)\times(4\times\pi\times10^{7})\times(2\times\pi\times0.8\times10^{-3})}}$

$\delta_1 =$338.56 km

at $f = 6.9$ mHz

$\delta_1 = \sqrt{\frac{2}{(1/361)\times(4\times\pi\times10^{7})\times(2\pi\times6.9\times10^{-3})}}$

$\delta_1 = 115.27$ km

It can be seen that during the low geomagnetic activity the classical skin depth is larger than the depth of the first layer. Thus, the skin effect is different during different storm conditions. During low geomagnetic conditions, the bottom layers will have more influence on the characteristics of the electric field.

Appendix B: CURRENT DENSITY AND CURRENT GRAPHS FOR THE SELECTED PERIOD

The current density (**J**) is the current per unit area. The total current [I] in the medium is obtained by integrating the current density over the area where the current is flowing, thus

$$I = \int \mathbf{Jds} \tag{B.1}$$

In the context of the study to determine the current distribution as a function of depth of the Earth model, the current density is integrated along the depth of the Earth model. The total current $I(z)$ in is given by:

$$I(z) = \int_0^z \mathbf{Jdz} \tag{B.2}$$

The resultant is the line current in A/m along the depth. For the selected low and high geomagnetic activity times, (02:30 UT for low and 06:45 UT for high on the 29^{th} of October 2003), the current density and the current distribution are shown in Figures B.1 to B.4. The current density distribution figures illustrate the discontinuity of the current density with depth. The depth where the current is 95 % of the total current for each configuration during a typical low and high geomagnetic period are indicated.

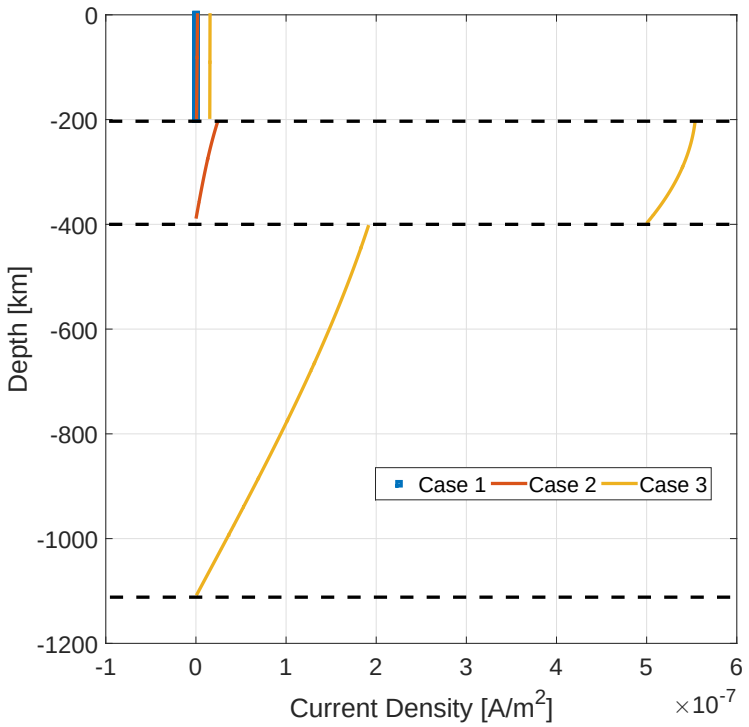

(a) Current density distribution due to By at low geomagnetic activity

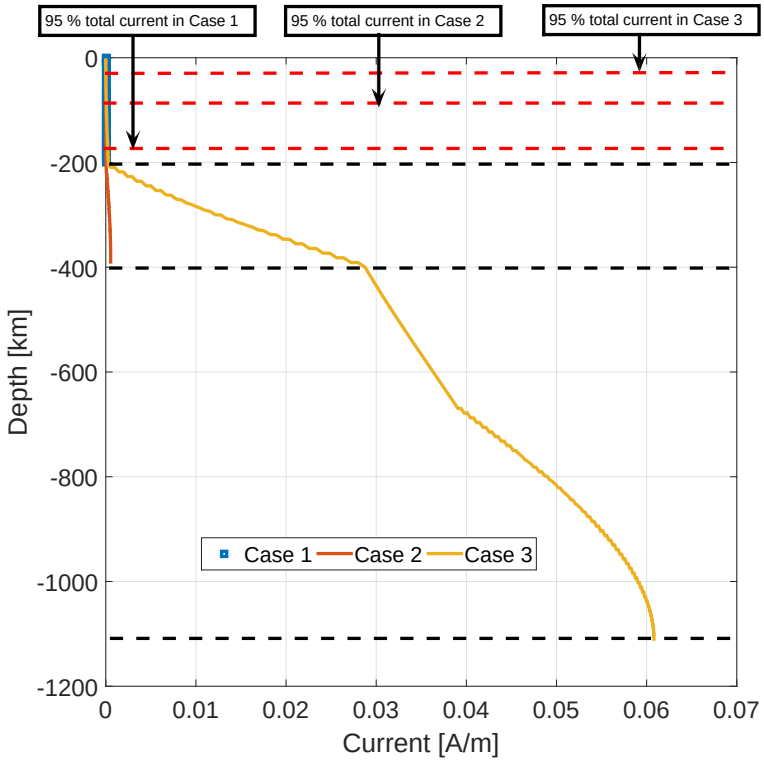

(b) Current distribution due to By at low geomagnetic activity

Figure B.1: Current density and current during the low geomagnetic activity for the By magnetic field component.

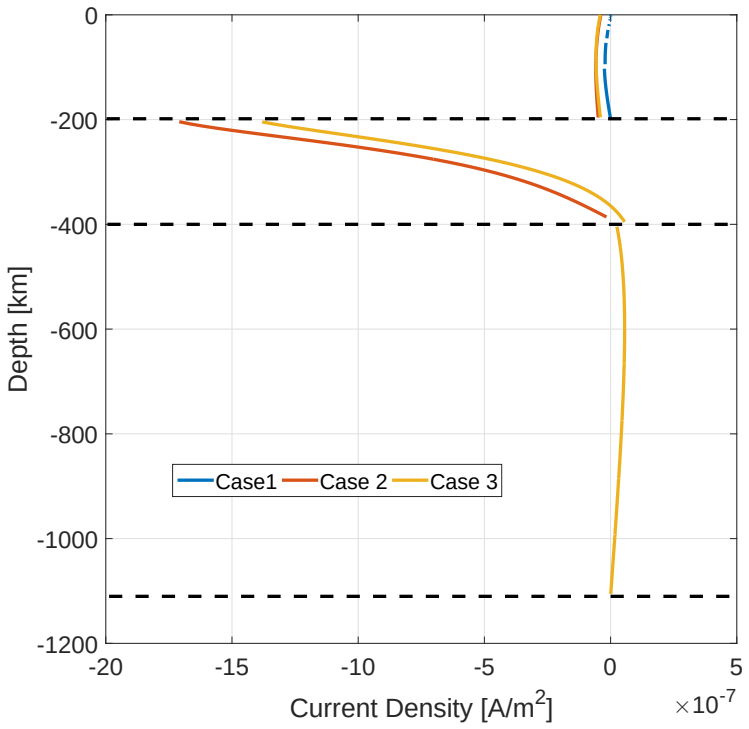

(a) Current density distribution due to By at high geomagnetic activity

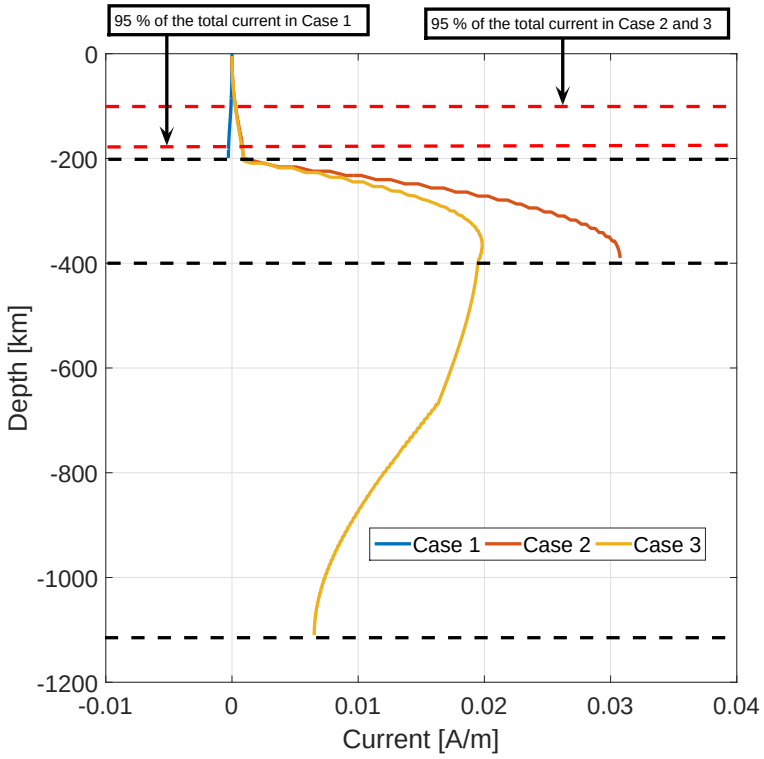

(b) Current distribution due to By at high geomagnetic activity

Figure B.2: Current density and current during the high geomagnetic for the By magnetic field component.

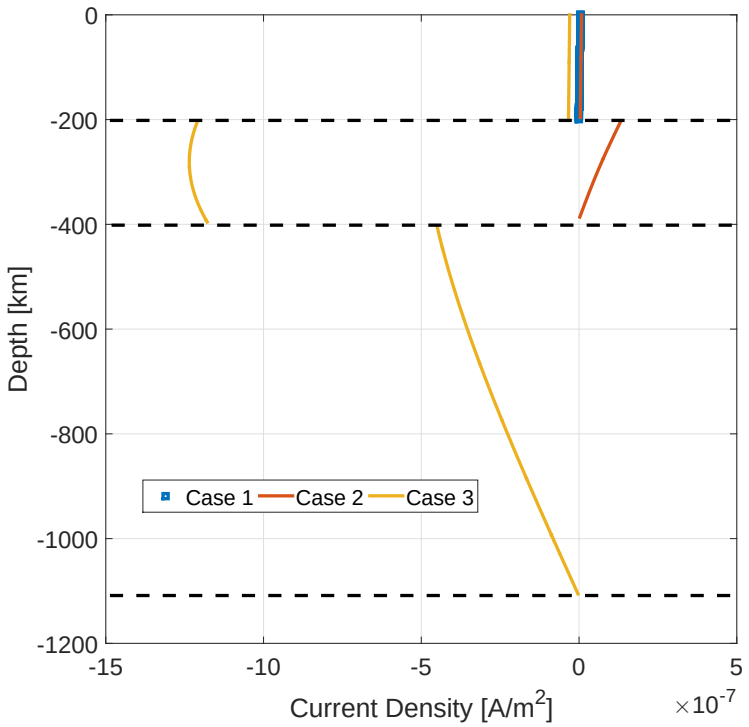

(a) Current density distribution due to Bx at low geomagnetic activity

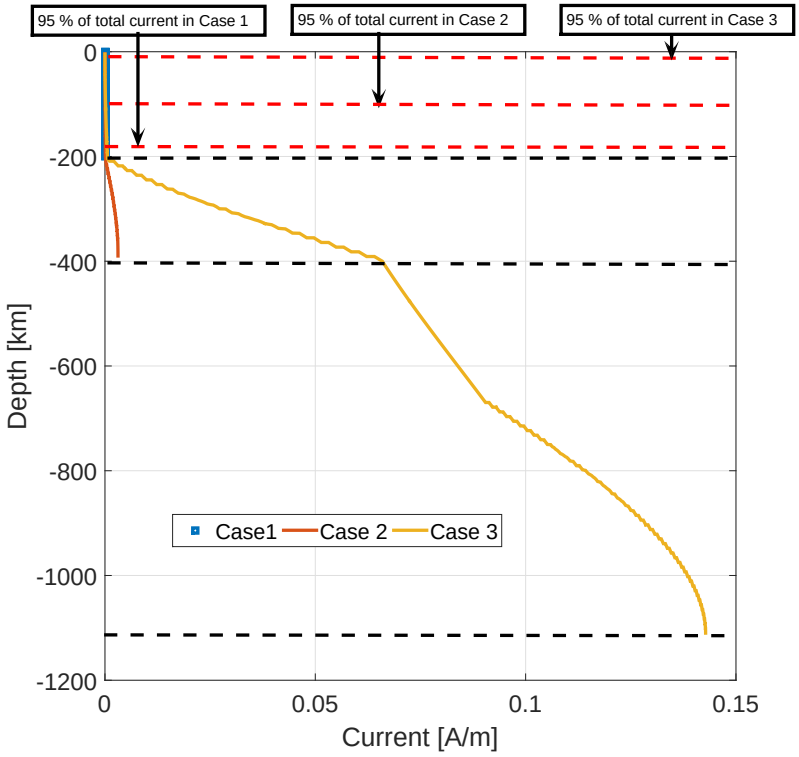

(b) Current distribution due to Bx at low geomagnetic activity

Figure B.3: Current density and current during the low geomagnetic activity for the Bx magnetic field component.

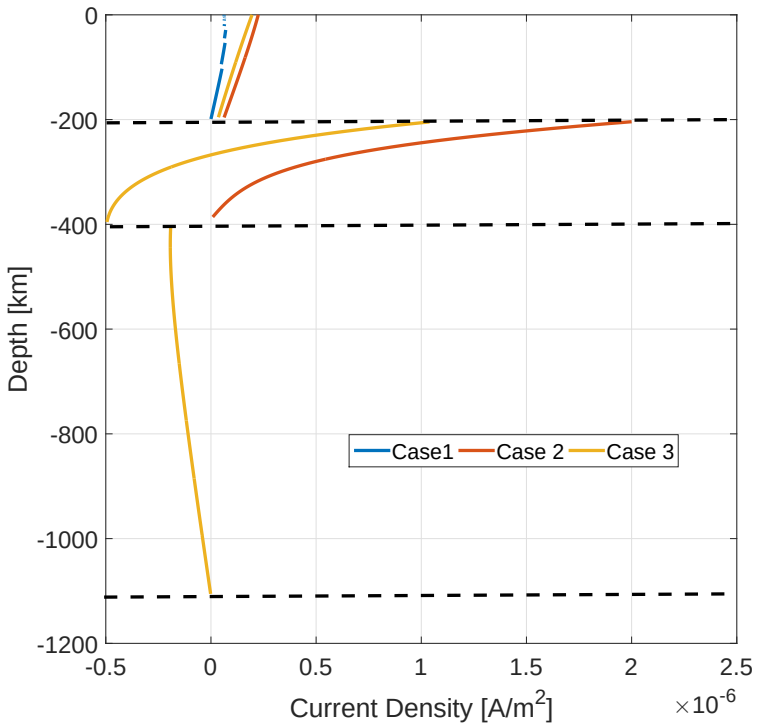

(a) Current density distribution due to Bx at high geomagnetic activity

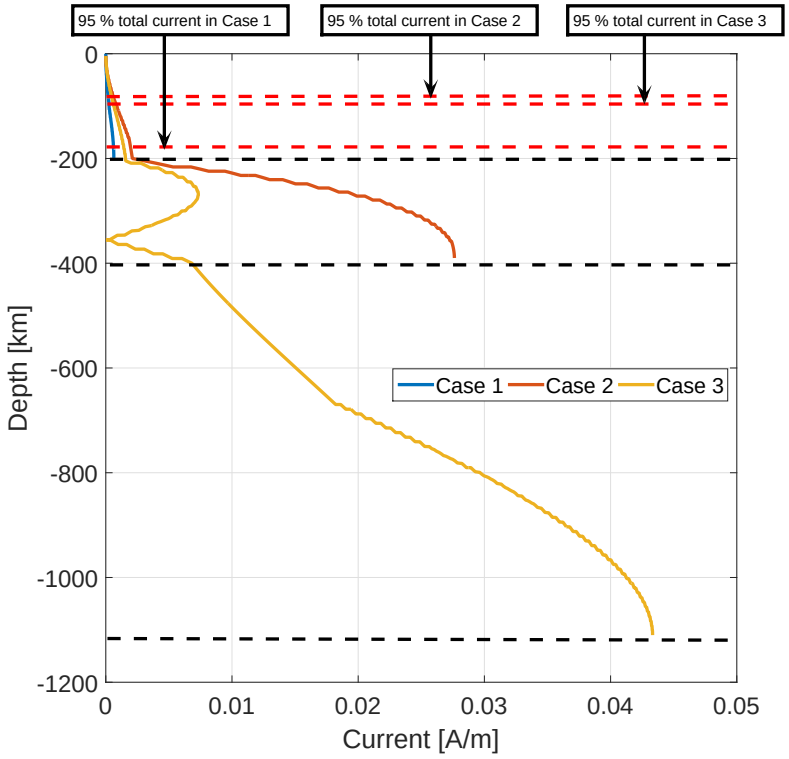

(b) Current distribution due to Bx at high geomagnetic activity

Figure B.4: Current density and current during the high geomagnetic activity for the Bx magnetic field component.